Characterization of molecular systems by scanning probe microscopy for nanoelectronics applications : from single molecules to molecular crystals

Hugo Therssen

Université de Lille

ED ENGSYS Ecole doctoral Sciences de l'Ingénierie et des Systèmes

IEMN Institut d'électronique de microélectronique et de nanotechnologie

Thèse soutenue par Hugo THERSSEN

Le 14 décembre 2022

Pour obtenir le grade de Docteur de l'université de Lille

Spécialité Électronique, microélectronique, nanoélectronique et micro-ondes

Caractérisation de systèmes moléculaires par microscopie à sonde locale pour des applications en nanoélectronique : des molécules uniques aux cristaux moléculaires

Characterization of molecular systems by scanning probe microscopy for nanoelectronics applications: from single molecules to molecular crystals

Devant un jury composé de :

Rapporteur	Lionel PATRONE	Université Aix Marseille Chargé de recherche CNRS
Rapporteur	Philippe LECLERE	Université de Mons Professeur
Président du jury	Frank PALMINO	Université Franche-Comté Professeur
Examinatrice	Sylvie GODEY	IEMN Ingénieure de recherche CNRS
Invité	Dominique VUILLAUME	IEMN Directeur de recherche CNRS
Co-directeur de thèse	Thierry MELIN	IEMN Directeur de recherche CNRS
Directeur de thèse	Stéphane LENFANT	IEMN Directeur de recherche CNRS

À ma Maman qui m'a énormément donné. Tu resteras pour toujours mon modèle de courage.

Acknowledgement

First of all, I would like to express my gratitude to all the members of the NCM group at IEMN. My supervisor Stéphane Lenfant and my co-supervisor Thierry Melin chose me 3 years ago for this thesis subject. They have supported me all along the way in a very professional way. Their scientific discussions and group work have enriched my knowledge and skills to complete this thesis. I would like to thank Sylvie Godey for her help in the technical part of the work, her availability, her support and all the time spent together on the near field platform to make it work the JT.

I would like to thank Dominique Vuillaume for his help in finding a charge transport model for my subject. Special thanks to Dominique Deresmes who answered my many questions about AFM and electronics.

I must also thank all the administrative assistants, Emmanuelle Gillman, Nora Benbahlouli and Andy Ledent.

During the three years I spent at the IEMN, I met many wonderful people. First of all, my PHD companions: Kamila, Cécile and Corentin. Time has passed quickly and the good times spent with you have been numerous. There are other PhD students and post-docs to thank, I will mention some of them: Michel, Kiril, Vincent and Davide. I wish you good luck for your future projects.

I would like to thank Lionel Patrone, Philippe Leclere for accepting to report on my thesis and Frank Palmino and Sylvie Godey for joining the jury of my thesis defense.

I thank all my friends, for all the good times spent together and the listening you had during my PhD

A big thank you to my family who always supported me in my choices, who always let me choose the path I wanted to take, their encouragement and their unconditional love.

Finally, I must thank my girlfriend, Louise. It has been six years since we started this adventure together, we have grown together along the way, not without friction but she has always been by my side.

Abstract

This manuscript reports on scanning probe microscopy study of α, γ-bisdiphenylene-β-phenylallyl (BDPA), *3,3',5,5'-tetra-tert-butylazobenzene* (TBA) and Prussian blue analogue (PBA) $Co^{III}[Fe^{II}(CN)_6]$ (noted CsCoFe) molecules for applications in nanotechnology and molecular electronics.

We observed thanks to Scanning Tunneling Microscopy (STM) in ultra-high vacuum (UHV) at low temperature (4K), BDPA self-assemblies on Au(111) organized in chains. These chains behave like a one-dimensional harmonic oscillator at a temperature ≈ 15 K due to the phonon-molecule coupling. We observed that the vibrations of the chain were attenuated or stopped depending on the polarization applied during STM imaging. The charge states of the molecules on the substrate were studied by Kelvin Probe Force Microscopy in UHV.

The TBA molecule is a derivative of azobenzene molecule with four spacer groups for the decoupling of the molecule from the gold substrate. This molecule switches between two isomeric stable states (*trans*-TBA and *cis*-TBA). We study by STM and non-contact Atomic Force Microscopy in UHV with sub-molecular resolution the effect of the electric field and UV irradiation on TBA monolayers deposited on Au(111) substrate on the switching of the TBA molecule between these two isomeric states. We demonstrate that the electric field induces bright spots with a height of 0.25 ± 0.02 nm, these spots are associated to the *cis*-TBA isomer. The effect of UV irradiation induces another effect, that we suppose associated with a deterioration of the TBA molecule.

PBA molecules constitute a large family of materials with an open framework structure. PBA molecules form a nanocrystal whose size can be controlled according to the chemical process applied. We have electrically characterized by Conducting-AFM in air, single PBA CsCoFe nanocrystals with typical size of 15, 30 and 50 nm. We observe that when the size of the nanocrystal increases, the recorded current measured by Conducting-AFM also increases. To explain this effect, we consider the tip-molecule contact as a metal-"semi-conductor" metal and use the Double Schottky barrier model. This model shows that the height of one of the contact barrier decreases from 0.34 eV to 0.23 eV when the height of the nanocrystal increases.

This work illustrates the effects of coupling a molecule to a substrate, and opens the way to molecular devices.

Contents of the manuscript

General introduction

This research work is rooted in the field of nanotechnology, and more specifically in molecular nanoelectronics. The term nanoelectronics refers to the use of nanotechnology for the design of electronic devices components at the nanoscale. Nanoelectronics covers various types of electronic components and materials, whose common characteristics is that they are so small that physical effects modify the properties of the materials at the nanoscale. Spintronics, optoelectronics, flexible and wearable electronics are some of the applications that are driving active research in the field. Molecular electronics is part of nanoelectronics and deals with electronic processes that occur in molecular structures. Molecular electronics aims at the fundamental understanding of charge transport through molecules and is motivated by the vision of molecular circuits that allow the creation of tiny, low-cost and energy-efficient devices components.

Chapter 1 describes in general the domain and applications of nanotechnology.

In **Chapter 2**, we will discuss the scanning probe microscopy techniques used in this thesis and we will describe the different experimental set-ups used to obtain our results.

Chapter 3 presents a study of the transport properties at the scale of a nanocrystal of Prussian blue analogue. The nanocrystals studied are deposited on a highly oriented pyrolytic graphite and the electrical transport is measured using a conductive tip of an atomic force microscope as the top electrode at ambient air. Results are analyzed in the framework of electronic models for charge transport through molecular junctions.

Chapter 4 presents a low-temperature UHV study of the chain assembly of a stable molecular radical on Au(111), exhibiting nanoscale harmonic oscillator properties. A detailed study of the charge of the molecule is carried out to determine the role of the charge of the molecule in its vibrational characteristics.

Chapter 5 presents a study on electro and photo-switchable molecules on Au(111). The organization of the molecule on the metal substrate is studied first. The different stimuli will then be carried out to observe by STM and non-contact AFM the impact on the configuration of the molecule.

Chapter 1: Introduction to nanotechnology and nanoelectronics

The prefix « nano » for nanotechnology refers to the Greek prefix meaning “dwarf”, or something very small. In science, “nano” designates one thousand millionth of a meter (10^{-9} m). Nanoscience aims to study structures, systems and molecules at the scale of the nanometer. Nanotechnology utilizes all the knowledge of nanoscience and nanoscale properties[1] in practical applications such as innovative materials, electronic devices, anticancer research, drug delivery, etc[2–5]. To realize how much nano is small, a single human hair is 60,000 nm thickness and the DNA double helix has a radius of 1 nm[6]. Nanotechnology is one of the most promising technologies of the 21st century and provides the ability to convert the nanoscience theories to an applicative manner by observing, measuring, manipulating, assembling, controlling the matter at the size of the nanometer scale.

1.1 Genesis of nanotechnology

Richard Feynman introduced the concept of nanotechnology in 1959. During the annual meeting of the American Physical Society, he presented a lecture entitled “There’s plenty of room at the bottom”. R. Feynman described a vision of using machines in order to construct smaller machines down to the nanometer scale[7]. After fifteen years in 1974, a Japanese scientist named Norio Taniguchi was the first to use the term “nanotechnology”. Since R. Feynman, two approaches have been developed to fabricate nanostructures. The first method is called “top-down” and the second “bottom-up”. They differ by their degrees of quality, speed, mass-fabrication and cost.

The top-down approach aims to fabricate nanosized structures starting from bulk materials. Top-down approaches are inherently simpler and depend either on removal or on division of bulk material or on miniaturization of bulk fabrication processes to produce desired structures with appropriate properties. This can be achieved by using advanced techniques such as lithography. One problem with the top-down approach is the imperfection of surface structure. For example, nanowires made by lithography are not smooth and may contain impurities and structural defects[8]. Lithography opened the way to mass production of nanoscale devices and permitted the digital revolution we know nowadays.

The bottom-up approach refers to build-up of nanostructures by physical or chemical methods from the bottom: atom by atom or molecule by molecule. This alternative approach has the potential of creating less waste and hence can be more economical. Self-assembly is a bottom up approach in which atoms or molecules organize themselves into ordered nanostructures.

1.1.1 Nanotechnology in our days

Since the declaration of R. Feynman, a huge advance was made when the physicists Gerd Binnig and Heinrich Rohrer invented a new type of microscope at IBM, the Scanning Tunneling Microscope[9,10], followed by the invention of the atomic force microscopy. Scanning probe microscopes are the instruments of choice for nanoscience and nanotechnology research today[11].

A large number of domains have interest in nanotechnology. In chemistry, the nanometer range is associated to the dimensions of colloids, polymer molecules, very large molecules or aggregates of molecules, but recently also structures such as semiconductor nanorods[12] or particles[13], conductor quantum dots[14,15], molecular switches[16–18], molecular magnets[19–21]. In physics and electrical engineering, nanoscience is associated with quantum behaviors[15,19,22], and particularly behaviors of electrons[23,24] and photons in nanoscale structures[25–27]. Biology and medicine also show a deep interest in nanoscience as for drug delivery or *e.g.* for creating new structures based on DNA[28,29].

One of the most important fabrication technology of our time is microlithography. The technique provides microprocessors and memories, which is the basis for the information technology that has transformed society in the half-century. Microelectronics followed the Moore's law for almost 50 years and provided a popular expression "smaller is cheaper and faster"[30]. The technical evolution in the semiconductor industry has brought the devices components of commercial semiconductor devices to size down to 10 nm or below.

However, the Si-technology miniaturization runs into several physical and technological limitations in the long term. Molecules could offer the ultimate miniaturization of logic circuits by using single molecules, which could act for example as electronic switches[31–33] and storage elements[34,35]. In fact, molecules are the smallest building block providing a large amount of diversity to address various functions by structural design, and are able to organize themselves on surfaces into regular and dense two-dimensional patterns. Recently, molecular systems based on organic compounds with specific dielectric or electronic conduction properties have been enabled to build applicative devices such as liquid display[36], organic transistor[37], organic light-emitting diodes[38,39].

1.1.2 Nanotechnology applications

Nanomaterials

Nanomaterials are already used in numerous products and industrial applications. As example we can quote organic light-emitting diode (OLED) use for flat panel displays and lighting panel or an important use of nanoparticles and nanotubes in composite materials. The enhancement of properties can be focused on the mechanical properties but can be extended to optical, electrical and magnetic properties. As example, we can quote carbon fibers and carbon nanotubes used in polymers in order to control and enhance electrical conductivity[40], or the use of nanoparticles as fillers in a matrix, such as carbon black used to mechanically reinforce car tyres. Nanocoatings and nanostructured surfaces can also be included in the wide family of nanomaterials. Coatings with controlled thickness at the nanoscale have been in routine production for some time. As an example, we can quote molecular beam epitaxy[41] and metal oxide chemical vapor[42].

Nanobiotechnology

Nanobiotechnology is the application of nanotechnology in the biological field. This field is hybrid and regroups chemist, physicist and biologist skills in collaboration. Biotechnology deals with metabolic and other physiological processes of biological subjects. The integration of nanomaterials with biology has led to the development of diagnostic devices[43], contrast agents[44], drug-delivery devices[45]… Nanoelectronics applied to the medical sector also induces deep changes, for instance by exploiting the traditional semiconductor industry, miniaturization and integration for implantation for brain, stimulation, pacemakers and limb stimulation.

Nanosensors

Nanosensensors can be defined as sensing devices smaller than 100 nm, used to collect information at the nanoscale and transfer it into data for analysis. Nanosensors take advantage of physical and chemical properties of matter at the nanoscale. Nanosensors have been developed for the detection of chemical gases and biochemical agents as well as physical variables[46–48].

Nanoelectronics

Nanoelectronics refers to the use of nanotechnology in electronic devices components. Nanoelectronics deals with various types of devices and materials. Quantum mechanical properties play in general a significant role in nanoelectronics. Nanoelectronics notably includes the field of spintronics, which the exploits the electron spin in solid-state electronic devices, and the field of optoelectronics which deals with the sourcing, control, and detection of light. Part from nanoelectronics, molecular electronics designs devices from molecular structures and aims to

understand the fundamental properties of charge transport through molecules. The molecular nanoelectronics is introduced in more details in Section 1.2. It is the main context of this thesis.

1.2 Molecular nanoelectronics and electronic functions

1.2.1 Molecular junctions

The concept of molecular electronics comes from Mann and Kuhn on organic monolayers in 1971[49]. Aviram and Ratner introduce the concept of using organic molecule as molecular diode[50]. More generally, molecular electronics tries to provide answers to miniaturization issues in technological devices, without reducing the efficiency and performance of existing technology. The creation of molecular devices is however a research field in itself, because the fabrication of molecular structures is highly sensitive to defects, hard to control and to replicate in mass production.

To form a molecular junction (MJ), molecules have to be connected between two electrodes. Molecular junctions are the main component in molecular nanoelectronics[51]. A difference needs to be made between MJ formed by one or few molecules (single molecule junctions) or several hundred or more molecules[52]. A junction can be formed or probed by the break-junction method[53],

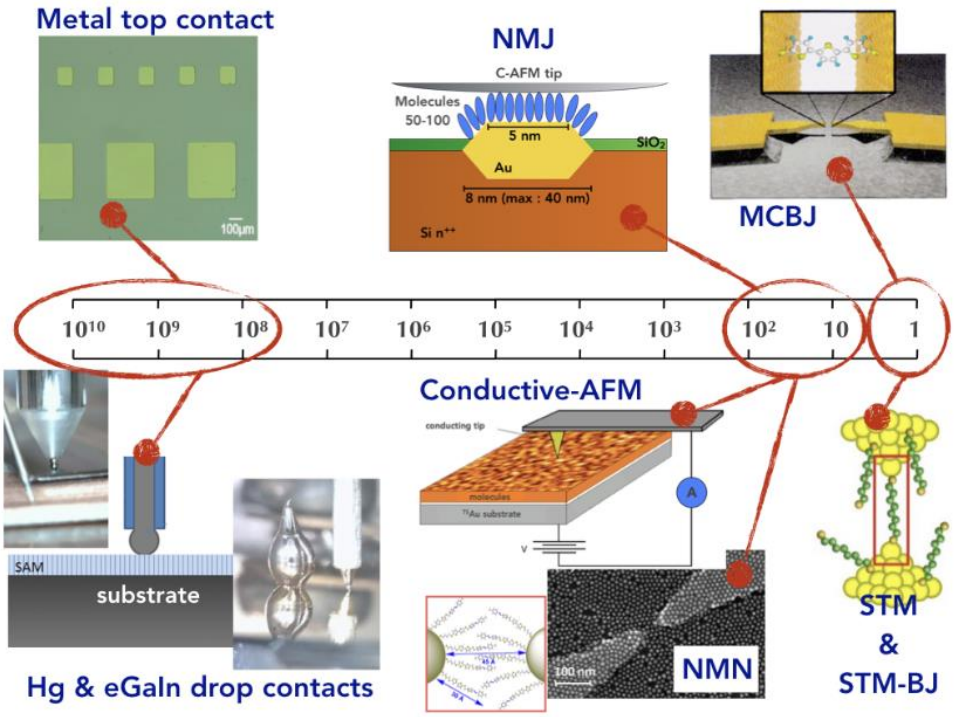

Figure 1. 1 : Overview of several types of molecular junctions (MJs) along a scale of the approximate number of molecules in the MJ: from "large area MJ" on the left of few molecules and single molecule junction on the right[52].

electromigration[54], conductive probe atomic force microscope (C-AFM)[55], scanning tunneling microscopy (STM)[10] etc.

The stability of molecules with time is important in a molecular junction. Molecules need to transport electronic current over high number of cycles without damage. Otherwise, the integration into molecular devices is not possible. Molecules can be grafted to a substrate by a chemical link to form a self-assembled monolayer[56] (SAM) or deposited by electrochemical methods or by evaporation[57,58].

1.2.2 Molecular wires

In electronics, a wire is the most basic object who allows the conduction of electric charges[59]. At the molecular scale, the electronic transport is expected to take part through the frontier orbitals of molecules. In general, when a π-system increases in size, the energy difference between frontier orbitals decreases in energy and the energy difference to the Fermi level of the electrode decreases accordingly. Large delocalized π-systems are thus promising candidates[60] as molecular wires. The simplest example is a chain of polyene, consisting of an alternating sequence of single and double bonds, leading to a π-system delocalized over the whole molecule length[61]. Many other examples consisting of aromatic building blocks like polybenzene, polythiophene etc have been extensively studied[62].

1.2.3 Rectification

A rectifier device allows the current to pass more easily in one direction than in the other. The concept of molecular electronics has already suggested the rectification as an electronic function obtainable from a molecular structure[50]. The first devices displaying rectification based on molecular structures consisted in Langmuir-Blodgett films sandwiched between two electrodes[63]. The coupling of the molecules to the electrodes (e.g. in the case of chemisorbed molecules) may lead to the formation of Schottky barrier at the interface. An asymmetric current-voltage characteristics can be measured in the molecular junctions in the case of (i) different anchor groups; (ii) different electrode materials; or (iii) different dipole moments created at the molecule-electrode interfaces.

1.2.4 Molecular switches

Molecular switches are molecules displaying at least two different conductance states, which can be switched by an external (*e.g.* electrical or optical) stimulus. The two states of the molecules can be associated to ON and OFF states. An important factor for a molecular switch is the conductance ratio(s)

at a given bias between the two or more states. There are classes of molecules which are stable in two different states[31,64–66]. Such bistable switches are characterized by a double potential well[67]. If the potential barrier is sufficiently high, the switching process may exhibit a hysteresis[68]. Molecular switches are in general classified by the nature of the external stimulus required to trigger the switch (azobenzene molecules can be *e.g.* switched optically[33,69]) and/or by the property or function that is switched. Molecular switches offer for example the possibility to transcribe the external stimuli into electrical signals, with switching times of the order of 100 ps[23]. Multiple mechanisms for the change of conductance of a molecular switches exist, such as the modification of the molecule charge state by charge trapping[64] or oxidoreduction[70], or a change of the molecule conformation by isomerization[23], which can drastically change molecular orbitals. The compound which has been the subject of the greatest number of studies remains the diarylethene (DAEs)[71,72] and the azobenzene (AZs)[18,73] derivatives.

1.3 The molecule-metal interface

A wide variety of molecules can be used for the fabrication of molecular electronic devices and for the study of fundamental issues related to *e.g.* growth and/or assemblies, structural and physical properties. The contact of the molecule with respect to electrodes (or the substrate) is of particular importance for electronic properties. Physisorption is characterized by weak van der Waals interactions between molecules and the surface. Chemisorption is defined by the formation of covalent bonds with the substrate[74,75] and/or by the charge transfer between the molecule and the substrate[76].

An important issue in molecular electronics and metal-organic interface is the energetic position of molecular frontier orbitals of the highest occupied molecular orbital (HOMO) and the lowest unoccupied molecular orbital (LUMO) with respect to the metal (electrode or substrate) work function. The metal work function is defined as the energy difference between the metal Fermi level (E_F) and the vacuum level (VL), as presented in Figure 1. 2 a). The interaction between the molecule and metal can induce an interface dipole (see Figure 1. 2)[77], which causes a shift of the vacuum level[78,79] at the molecule-metal interface. When a charge transfer occurs from the molecule to the metal surface, it leads to the formation of a cation or anion (see Figure 1. 2 b)). The direction of the charge transfer depends of the metal-molecule system. The formation of a chemical bond (see Figure 1. 2 c)) leads to a complete change of the metal-molecule electronic structure[80,81]. The pillow effect is due to the compression of the metal wave function at the metal-molecule interface as a consequence of the Pauli repulsion (see Figure 1. 2 d)), leading to a reduction of the local surface potential (or work function).

This effect appears with both physisorbed and also chemisorbed molecules interface[77,79]. Finally, the permanent dipole of a molecule (Figure 1. 2 e)), if any, creates an electrostatic potential which can shift molecular levels[82,83].

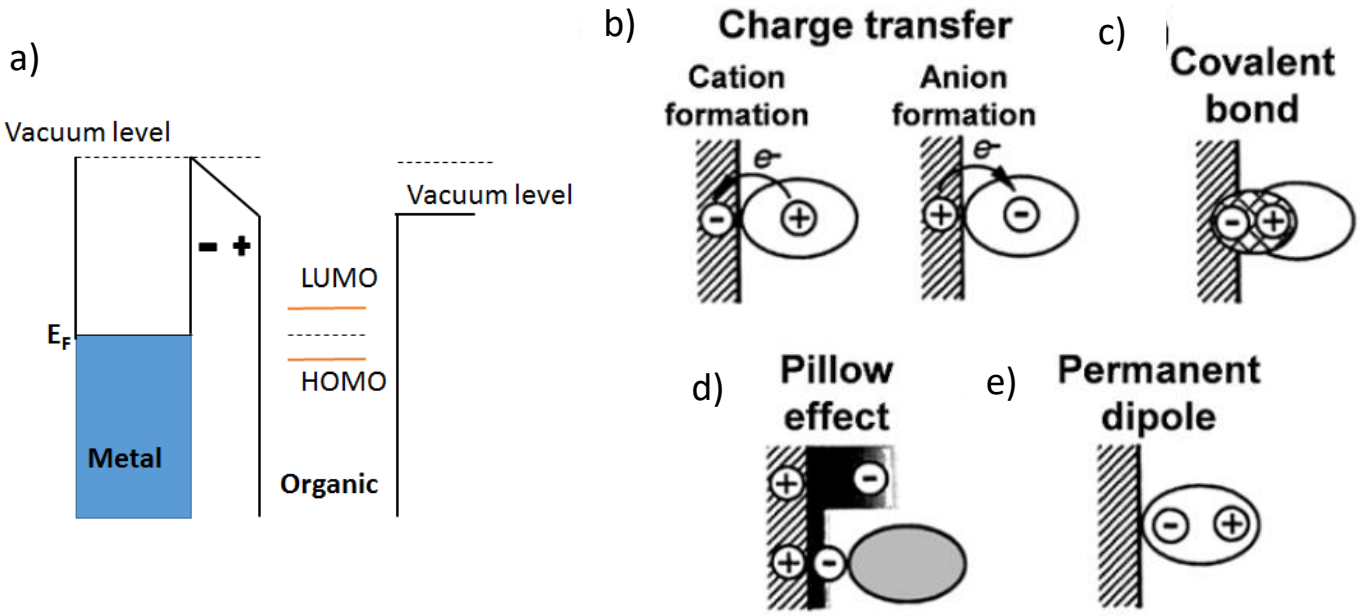

Figure 1. 2 : a) Energy diagram of a metal-molecule interface with a dipole. b)-e) Origins of the interface dipole: charge transfer from molecule (cation formation) or metal (anion formation), covalent bond formation, pillow effect and permanent dipole. Extracted from[77].

1.4 Historical introduction of Scanning Probe Microscopy

The advance in surface science tools is crucial for nanotechnology. Scanning probe microscopes (SPM) consist in a various set of microscopes which provide topographical images of surfaces, but also permit a nanoscale electrical characterization. Multiple variations of SPMs have been developed on the basis of STM and AFM[55,84,85].

The STM was the first instrument that enabled imaging of flat conductive surfaces with atomic resolution in ultra-high vacuum. STM helped to solve the open issue of the structure of the Si(111)-(7x7) surface reconstruction[86], by enabling its real space imaging confirming the dimer-adatom-stacking fault model for 7x7 reconstruction developed by Takayanagi *et al.*[87] on the basis of X-ray and electron scattering experiments. This success has resulted in Gerd Binnig and Heinrich Rohrer Nobel Prize in Physics in 1986.

Since, the STM has been used for a large number of metal and semiconductor analyses. However, the technique has limitations, especially with respect to the analysis of non-conducting materials. To

bypass this problem, AFM was developed. The AFM is based on a tip attached to a flexible cantilever that bends under the influence of the force acting on the tip. The first AFM used an STM tip coupled to the metallic backside of the cantilever to measure its deflection[11]. Since then, other techniques have been used to detect the cantilever deflection like the reflection of a laser on the backside of the cantilever[88]. In 1995, one decade after the AFM invention, the atomic resolution has been obtained using non-contact AFM[89]. In 2009, the operation of an AFM based on stiff quartz probes functionalized with a carbon monoxide molecule has enabled a sub-molecular resolution in molecule imaging, surpassing the resolution obtained by STM[90].

1.5 Conclusion

Molecular nanoelectronics uses the diversity offered by chemistry to exploit molecular properties for application in electronics. The molecular nanoelectronics try to complement semiconductor devices by providing new function or mimic existing function at the simpler process level and with a manufacturing cost lower by the help of self-organization capabilities. However, research for fundamental understanding of the physics at the nanoscale need to be performed to implement electronic device at the molecular-scale. The metal-molecule interface is a critical subject because the properties of a molecule in solution can be totally lost in contact with an electrode because of the physical molecule-electrode interaction. Understanding this interaction therefore becomes an important issue for nanoelectronics and the scanning probe microscopy appear as an indispensable tool. In this thesis the problematics of molecules-metal interaction and electronic properties are investigated through the study of three molecular systems.

Chapter 2 : Experimental section

In this chapter, the scanning probe microscopies used in this thesis are explained. Firstly, all the theoretical concepts of scanning probe microscopy are described. Noise sources are presented. Secondly, the setups used to perform ultra-high vacuum (UHV) and ambient air measurements in the framework of this thesis are presented. The preparation of tips and substrates for the analysis in UHV scanning-probe microscopy are shown. Finally, spectroscopy method is described.

2.1 Scanning Probe Microscopy

In the 1920s, the theory of quantum mechanics appeared, which changed the way we saw physics. It gave birth to concepts such as the wave-particle duality, the quantum superposition and tunnel effect, for example. All these principles are counterintuitive compared to classical physics. Concerning the tunnel effect, this is like saying in classical physics that a stone would be able to cross a concrete wall from one side to the other, while it is supposed to be stopped by it. In quantum mechanics, when a particle meets a wall (a very high-energy barrier), the probability of its presence on the other side of this energy barrier is superior to zero. This probability is exponentially decreasing with the width of the barrier in the direction of propagation of the particle. The first implementations of this phenomenon date back to 1957 with the tunneling diode discovered by Leo Esaki, Nobel Prize in Physics in 1973[91]. In 1981, IBM developed the scanning tunneling microscope with Gerd Binnig and Heinrich Rohrer (Nobel Prize in Physics in 1986), which is one of the keystones of nanoscience today[10,11,92–95].

2.1.1 Scanning tunneling microscopy

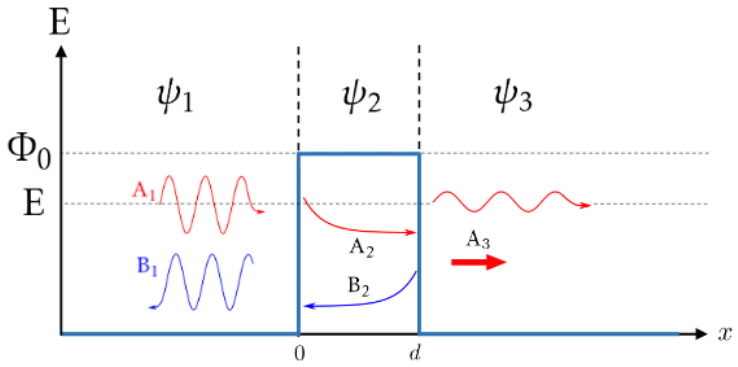

Figure 2. 1 : Schematic view of a 1D tunnel barrier along the propagation axis x. An incident electronic plane wave of amplitude A1 and energy E moves toward the barrier. A part of this initial wave is transmitted at the first interface (A2) while the other part is reflected (B1). This transmitted wave is again partially reflected (B2). The transmitted part of A2 finally reaches the other side of the tunnel barrier (A3). Adapted from[95].

We will see here in more details the tunneling effect. Quantum mechanics predicts an exponential decay solution for the wave function of the electron Ψ across the barrier (Figure 2. 1). Let us now consider the diffusion of an electron coming from the left towards a potential barrier characterized by its width d and its potential value ϕ_0. Consider the time-independent Schrödinger equation in one dimension

$$\left[-\frac{\hbar^2}{2m}\frac{\partial^2}{\partial x^2}+V(x)\right].\Psi(x)=E.\Psi(x) \qquad \textbf{(2. 1)}$$

where ħ is the reduced Planck constant, m is the mass of an electron, V(x) is the potential along the x axis, and E is the energy of the electron. V(x) = 0 for x<0 (region 1) and x>d (region 3), and V(x) = ϕ_0 for 0 < x < d (region 3). Ψ_1, Ψ_2, Ψ_3 verify Schrödinger's equation in their respective region.

X < 0 $$-\frac{\hbar^2}{2m}\frac{\partial^2\Psi_1}{\partial x^2}=E\Psi_1$$

0 < x < d $$-\frac{\hbar^2}{2m}\frac{\partial^2\Psi_2}{\partial x^2}+\Phi_0=E\Psi_2 \qquad \textbf{(2. 2)}$$

X > d $$-\frac{\hbar^2}{2m}\frac{\partial^2\Psi_3}{\partial x^2}=E\Psi_3$$

The general solutions for the different areas are

$$\varphi 1(x) = A_1 e^{ikx} + B_1 e^{-ikx}$$
$$\varphi 2(x) = A_2 e^{\alpha x} + B_2 e^{-\alpha x} \quad \textbf{(2. 1)}$$
$$\varphi 3(x) = A_3 e^{ikx}$$

In this expression $k = \sqrt{\frac{2m}{\hbar^2}E}$ is the incident wave vector, $\alpha = \sqrt{\frac{2m}{\hbar^2}(\Phi_0 - E)}$ is the transmitted wave vector and A_n and B_n are the incident and reflected parts of each wave in region n, i the imaginary unit. The transmission coefficient is

$$T(E) = \left|\frac{A_3}{A_1}\right|^2 \quad \textbf{(2. 2)}$$

All wave functions and their derivatives have to be continuous everywhere and so we are able to calculate A_3 and we have for this system

$$T(E) = \left|\frac{A_3}{A_1}\right|^2 = \frac{1}{1 + \frac{{\Phi_0}^2}{4E(\Phi_0 - E)} sinh^2(\alpha d)} \quad \textbf{(2. 3)}$$

So, the transmission coefficient T(E) is not equal to zero, that means, the electron is able to cross the barrier due to their wave nature. By applying a bias V on the sample or the tip, the situation is reported in Figure 2. 2 where $E_{F,sample}$ and $E_{F,tip}$ are the Fermi level energies of the sample and tip respectively, d is the barrier's thickness.

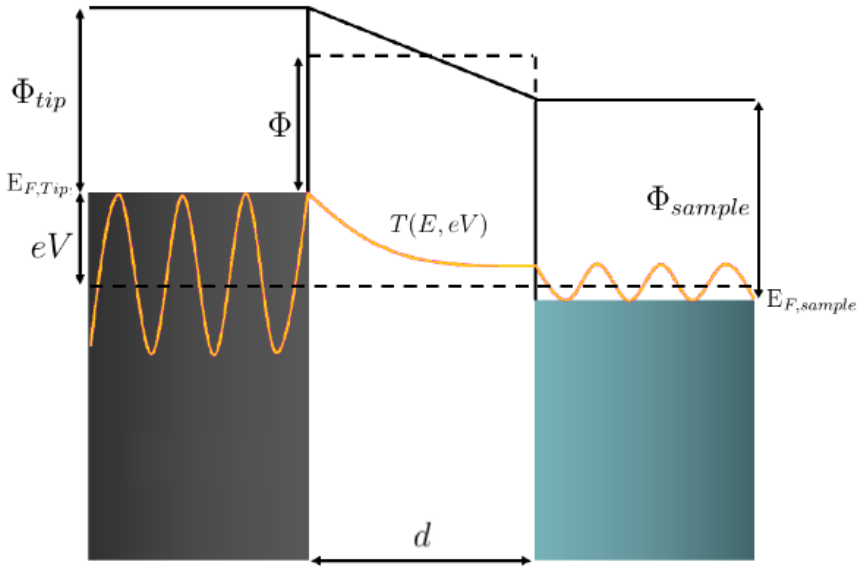

Figure 2. 2 : Schematic energy diagram of the tunnel junction in a STM. Adapted from[94].

As the applied polarization eV is usually small compared to the height of the tunneling barrier Φ, the energy barrier can be simplified in a square barrier with averaged height:

$$\Phi = \frac{\Phi_{tip} + \Phi_{sample}}{2} - \frac{eV}{2} \quad \textbf{(2. 4)}$$

where ϕ_{tip}, ϕ_{sample} are the work functions of the tip and sample respectively.

By taking Eq. (2. 3) with ϕ replaced ϕ_0 and considering a larger barrier of a few angstroms ($\alpha d >> 1$), we can obtain the approximation of T(E):

$$T(E) \sim \frac{16E(\phi - E)}{\phi^2} e^{-2\alpha d} \quad \textbf{(2. 5)}$$

and by replacing all terms and using Eq. (2. 4) we write T(E) as:

$$T(E) \sim \frac{16E(\Phi - E + \frac{eV}{2})}{\Phi^2} e^{-2d\sqrt{\frac{2m}{\hbar^2}(\Phi - E + \frac{eV}{2})}} \quad \textbf{(2. 6)}$$

At a given bias V applied on the sample, we need to integrate the transmission coefficient T(E,eV) of the electron across the barrier to all energy states between $E_{F,sample}$ and $E_{F,tip}$. We can write the integral between 0 and eV to determine the current through the tunnel junction as:

$$I = \int_0^{eV} T(E, eV)\rho_{tip}(E - eV)\rho_{sample}(E)dE \quad \textbf{(2. 7)}$$

with ρ_{tip} and ρ_{sample} the local densities of electronic states of the tip and the sample respectively. By using Eq. (2. 6) in Eq. (2. 7) we have:

$$I = \int_0^{eV} \frac{16E(\Phi - E + \frac{eV}{2})}{\Phi^2} \exp\left(-2d\sqrt{\frac{2m}{\hbar^2}\left(\Phi - E + \frac{eV}{2}\right)}\right)\rho_{tip}(E - eV)\rho_{sample}(E)dE \quad \textbf{(2. 8)}$$

This exponential dependence of the current I with the tip-sample distance d is fundamental for STM. For a variation of 1 Å, we have a variation of a decade in current. This change is enough to detect vertical variations at the atomic scale.

The sample topography represented in the z direction can be obtained by keeping a constant height across the entire sample and measuring the variation of the tunneling current. However, this method can cause the destruction of the tip if the roughness of the sample is higher than the tip-sample distance. The solution to this problem is to use a tunneling current value as setpoint; the piezoelectric transducers are controlled by a feedback loop to reach the distance for which the tunneling current is maintained to the setpoint current I. A schematic view of STM is presented in Figure 2. 3. To approach

the tip at several nanometers and obtain atomic resolution without crashing it on the surface, we need several conditions like a very sharp metallic tip and a feedback loop with faster response as compared to the scan speed.

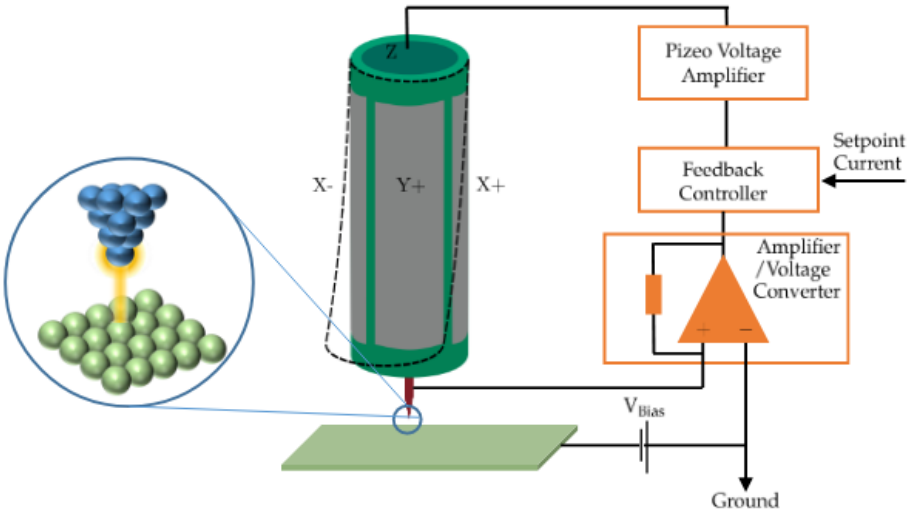

Figure 2. 3 : Sketch of the tunneling junction and the feedback controlling circuit in scanning tunneling microscopy. The tip, supported by a piezoelectric tube, is represented as atomically sharp with an ideal conic shape. A voltage bias is applied between the tip and the sample and the resulting current is collected from the tip and amplified. After the current is compared to the current set point value thanks to a feedback controller circuit, a voltage is applied to the piezo tube to change the tip-sample distance and maintain a constant current. Adapted from[95].

2.1.2 Atomic Force Microscopy

After the success of the STM, Gerd Binnig and Calvin Quate proposed a new scanning probe microscope using a flexible tip-cantilever assembly to scan the surface[11]. The apex of the tip is nanometric and the tip interacts with the sample through inter-atomic, frictional, magnetic or electrostatic forces. The big advantage of the AFM over STM is the possibility to analyze conductive but also insulating surfaces. In the past decade, the AFM has emerged as a powerful tool to obtain nanostructure details and biomechanical properties of biological samples, including biomolecules and cells. The two main AFM modes are the contact mode using the cantilever in static mode, or the dynamic mode obtained by oscillating the cantilever at a specific frequency. Typically, changes in oscillation amplitude (amplitude modulation AFM) are employed in intermittent contact mode (also known as tapping mode). Changes in the resonance frequency (frequency modulation AFM) are commonly used in non-contact AFM. Frequency and amplitude modulation (FM and AM) AFM modes are illustrated in Figure 2. 4.

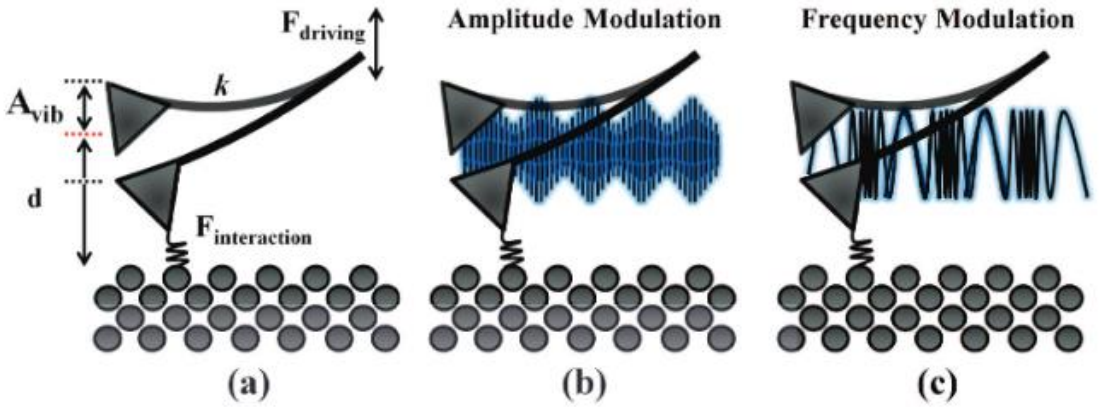

Figure 2. 4 : Driving force and tip-surface interaction force upon a vibrating cantilever (a) with a normal mode spring constant k, and with a vibrational amplitude, A_{vib}. Schematic representation of amplitude (b) and frequency modulation (c) AFM modes. Adapted from[93].

Force contribution

In AFM, different types of forces between the tip and the sample contribute to the total signal measured by the tip in the experiment. The potential energy V_{ts} between the AFM tip and the surface causes a z contribution to the sample tip force given by:

$$F_{ts} = -\frac{\partial V_{ts}}{\partial z} \quad \textbf{(2. 9)}$$

The z-dependence of this force induces an effective spring constant shift of the cantilever:

$$k_{ts} = -\frac{\partial F_{ts}}{\partial z} \quad \textbf{(2. 10)}$$

The frequency shift associated with the spring constant shift is used to regulate the z-position. Contrary to the tunneling current, which has a very short range, the force range between the tip and the sample can be both long-range or short range. There are short-ranged chemical forces (up to few nm) while at the long-range there are van der Waals, electrostatic and magnetic forces, which often exceed the short-range chemical interactions responsible for the atomic resolution. All interaction forces are presented in Figure 2. 5.

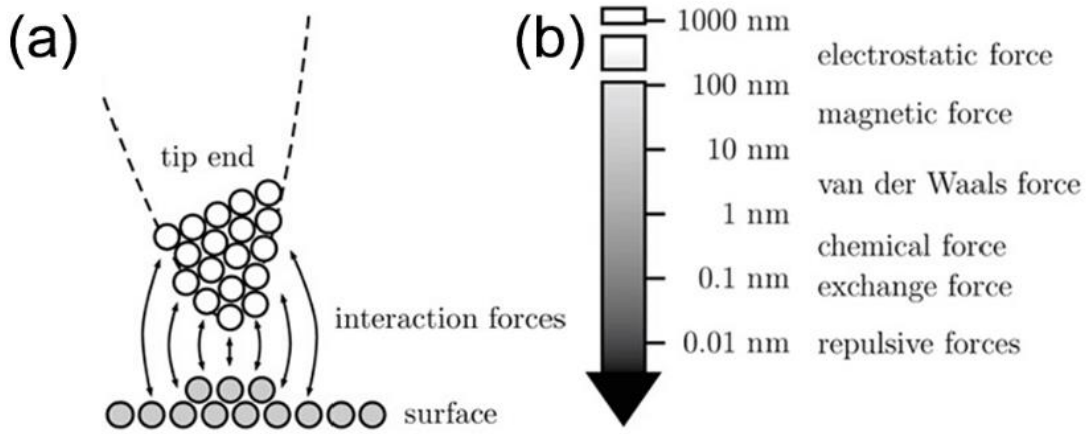

Figure 2. 5 : (a) Schematic representation of the tip-sample interaction forces (b) Representation of the forces that act at each z-scale. Adapted from[93].

Van der Waals forces are caused by an electrical interaction due to the dipoles of atoms or molecules. For two atoms separated by a distance z, the corresponding potential energy varies as $1/z^6$. The van der Waals force F_{vdw} for a spherical tip with radius R and an infinite plane is given by:

$$F_{vdw} = -\frac{A_H R}{6z^2} \qquad \textbf{(2. 11)}$$

where A_H is the Hamaker constant[96] which depends on the type of material of the tip and sample. A_H is of the order of 1 eV for most solids[96]. When the tip and the sample are conductive and a potential difference is applied between the tip and the surface, an electrostatic force is generated. Using a model of plane capacitor[97], the electrostatic force F_{el} can be expressed as:

$$F_{el} = 1/2 \frac{\partial C(z)}{\partial z} (V_{bias} - V_{CPD})^2 \qquad \textbf{(2. 12)}$$

where C(z) is a z dependent capacitance, V_{bias} is the voltage applied between the sample and the tip and V_{CPD} is the contact potential difference. Note, for V_{bias} = 0 V an electrostatic force is present due to the difference in work function between tip and sample materials. By applying the appropriate bias corresponding to V_{CPD}, we can suppress the capacitive electrostatic force[98,99] (see Figure 2. 6).

The last force that we will discuss is the case of chemical forces. Chemical forces correspond to a short-range interaction, which origin comes from the overlap of the electron wave function and repulsion of

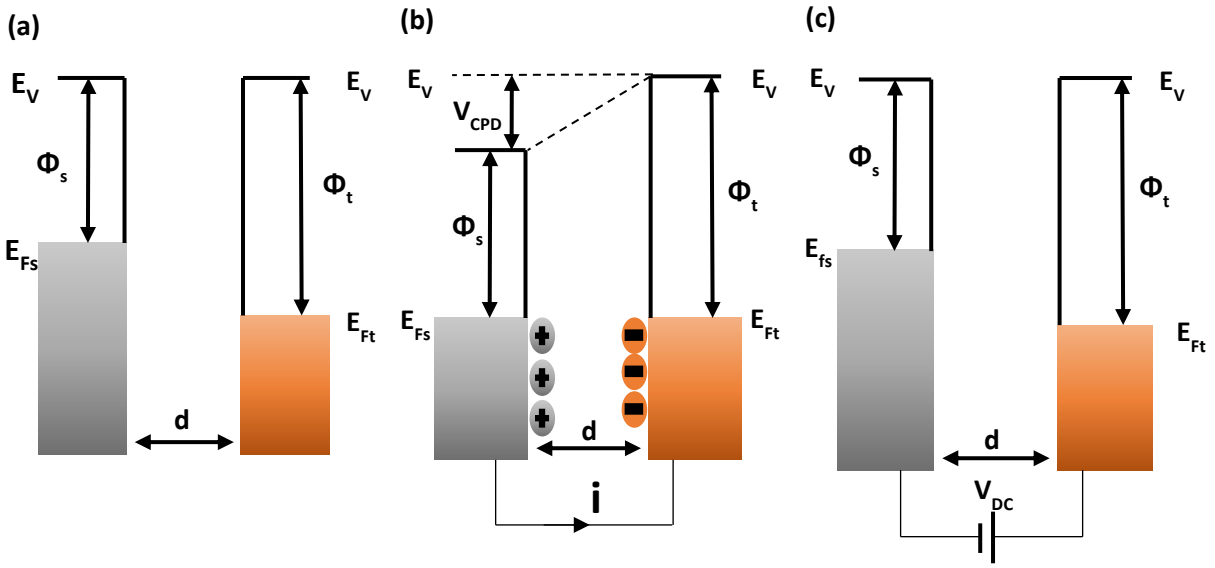

Figure 2. 6 : Contact Potential Difference voltage V_{CPD} between two different materials for the tip and sample with work functions Φ_s and Φ_t and Fermi energies of E_{Fs} and E_{Ft} respectively. E_V is the vacuum level corresponding to the energy of a free electron that is outside of the material. (a) Tip and sample, separated by a distance d and not electrically connected. (b) Establishment of an electrical connection and formation of V_{CPD}. (c) Compensation of the electrostatic force F_{el} by applying $V_{bias} = V_{CPD}$.

ion cores of the tips and sample atoms. The most common way to describe chemical forces is by using Lennard-Jones potential V_{Lj} [100] given by:

$$V_{LJ} = -E_{bond}[2\left(\frac{\alpha}{z}\right)^6 - \left(\frac{\alpha}{z}\right)^{12}] \quad \textbf{(2. 13)}$$

where E_{bond} is a bonding energy and α is the distance at which the potential energy V between particles is zero. The Lennard-Jones potential is shown on the Figure 2. 7 together with the long-range van der Waals attractive and Pauli repulsion forces.

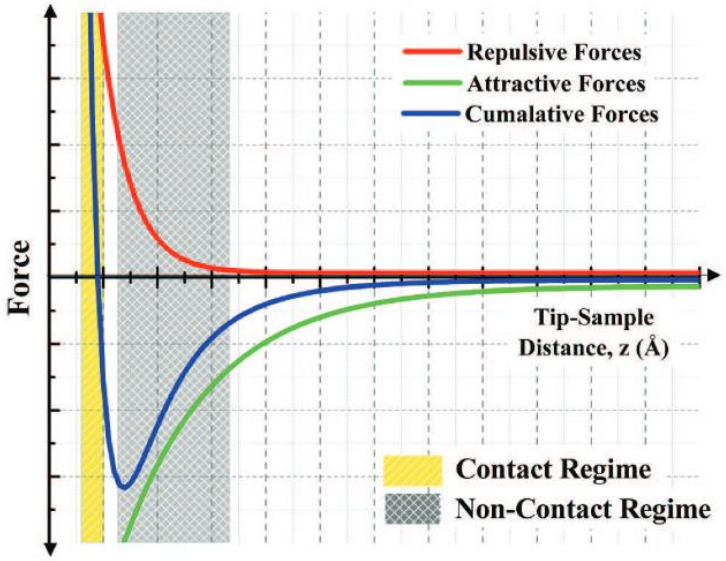

Figure 2. 7 : Force curve of an AFM tip as a function of surface distance. Extracted from[93].

2.2 Topography imaging modes

2.2.1 Tapping Mode AFM

A sharp cantilever positioned in close proximity to the surface is excited at its resonant frequency f_0. For this system the equation of motion can be described by a forced harmonic oscillator with damping[101]:

$$m\,\ddot{z(t)} + \gamma_0\,\dot{z(t)} + k\,z(t) = F_{ts} + F_0\cos(\omega t) \qquad \textbf{(2. 14)}$$

where k and m are the spring constant and the effective masse of the cantilever, F_0 and ω the amplitude and angular frequency of the driving force. F_{ts} describes the tip-surface interaction force, in absence of tip-sample interaction $F_{ts} = 0$, the angular resonance frequency of the driving force is equal to $\omega_0 = 2\pi f_0 = \sqrt{\frac{k}{m}}$. Finally, $\gamma_0 = m\frac{\omega_0}{Q}$ the damping factor, in which Q is the oscillator quality factor.

The force sensibility of an AFM depends on the quality factor of the vibrating cantilever. The quality factor (Q-factor) is a parameter that describes the damping of the oscillator. A higher Q-factor indicates a low rate of energy loss relative to the stored energy of the oscillator[101]. The Q-factor can be measured directly from the resonance frequency curves using:

$$Q = \frac{f_0}{FWHM} \qquad \textbf{(2. 15)}$$

with FWHM the Full Width at Half Maximum.

The solution of the harmonic oscillator[102] can be described as follows

$$z = B\exp(-\alpha t)\cos(wt + \beta) + A\cos(wt - \Phi) \qquad \textbf{(2. 16)}$$

Eq. (2. 16) presents a transient term and a stable solution where A, B, α and β are real numbers. At t=0, the two solutions are prominent. However, after a time of $2Q/\omega_0$, the transient term is reduced by exp(-αt) at this point the motion is dominated by the stable solution. The stable solution is the sinusoidal function with phase shift with respect to the excitation force. The amplitude can be written as follows, as a function of the excitation frequency:

$$A(\omega) = \frac{F_0/m}{\left[(\omega_0^2 - \omega^2)^2 + \left(\frac{\omega\omega_0}{Q}\right)^2\right]^{\frac{1}{2}}} \qquad \textbf{(2. 17)}$$

and the phase shift is described by:

$$tan\Phi = \frac{\omega\omega_0/Q}{\omega_0^2 - \omega^2} \quad \textbf{(2. 18)}$$

The Eq. (2. 19) shows that the oscillation amplitude depends on the driving force F_0, the damping and the position of the excitation frequency with respect to the natural frequency (the frequency at which a system tends to oscillate in the absence of any driving force).

When approaching the tip to the sample e.g. when the harmonic oscillator is under influence, the interaction forces cause a shift of the resonance curve of the cantilever. For small displacements with respect to the equilibrium position of the cantilever z_0, the force acting on the tip can be expressed as:

$$F = F_0 + \left(\frac{dF}{dz}\right)_{z0}(z - z_0) \quad \textbf{(2. 19)}$$

The effective spring constant of the harmonic oscillator is given by:

$$k_e = -\frac{dF}{dz} = \left(k - \frac{dF_{ts}}{dz}\right)_{z_0} \quad \textbf{(2. 20)}$$

Now considering the motion of the harmonic oscillator described by Eq. (2. 19) with the effective spring constant given by Eq. (2. 20), we can write the new effective resonance frequency ω_e as follows

$$\omega_e = \left(\frac{k - \left(\frac{dF_{ts}}{dz}\right)}{m}\right)^{\frac{1}{2}} \quad \textbf{(2. 21)}$$

The Eq. (2 .21) shows the resonance frequency of a weakly perturbed harmonic oscillator depends on the gradient of the force interaction. Assuming small force gradient in compared to the spring constant[103] ($k_{ts} << k$ where k_{ts} is defined by Eq. (2. 10)), the Eq. (2. 21) can be written as

$$\omega_e = \left(\frac{k - k_{ts}}{m}\right)^{\frac{1}{2}} \approx \omega_0(1 - \frac{1}{2}\frac{k_{ts}}{k}) \quad \textbf{(2. 22)}$$

$$\Delta f = -\frac{f_0}{2k}\frac{dF_{ts}}{dz} \quad \textbf{(2. 23)}$$

A change in the tip-sample distance leads to a change in the force gradient, which results in a complete shift of the resonance curve according to Eq. (2. 17). If we consider that the tip is excited at its natural frequency f_0, approaching the tip toward the surface modifies the resonance frequency, which implies a modification of the oscillation amplitude (Figure 2. 8).

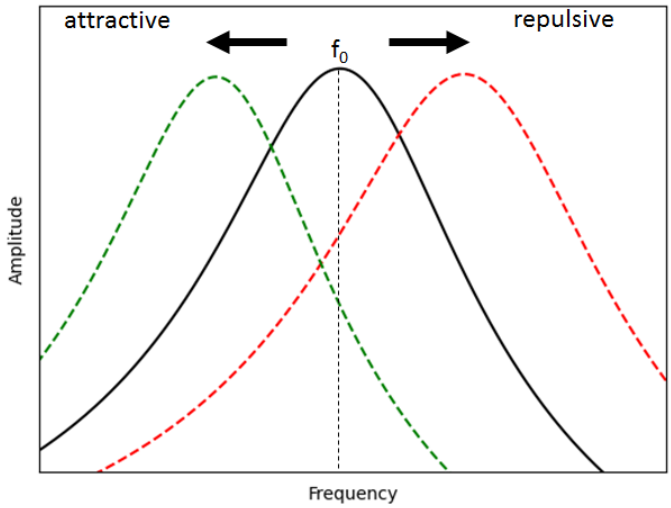

Figure 2. 8 : Resonance curve (solid line). The influence of attractive and repulsive force (dashed lines).

A study of the different limitations of using the harmonic model for dynamic AFM has been done by Holscher et al[104].

In most situations, Eq. (2. 23) allows to obtain easily an interpretation of the data. The above approximation is no longer valid for large oscillations compared to tip sample distance. In classical first-order perturbation theory[105], the solution is given by :

$$\Delta f = -\frac{{f_0}^2}{kA_0^2}\int_0^{1/f_0} F_{ts}(d + A_0 + A_0\cos(2\pi f_0 t))A_0\cos(2\pi f_0 t)dt \qquad \textbf{(2. 24)}$$

with A_0 the oscillation amplitude . This equation is much more complicated and obtaining the force value from the frequency shift in the experiment is not a trivial task. Different expressions for this force have been proposed[106–108].

2.2.2 Non-contact frequency modulation Atomic Force Microscopy

In general, the topography of the sample is imaged by scanning with a tip along a sample while keeping the interaction setpoint constant thanks to a feedback loop. A variety of AFM modes can be used depending on the objectives. In contact mode, the tip is in direct and permanent contact with the surface, the repulsive interaction between the tip and the sample is measured. In non-contact mode, the cantilever oscillates at its resonant frequency thanks to a piezoelectric element.

In non-contact mode (nc-AFM) the interaction force between the tip and the surface is considerably reduced in comparison with the contact-mode. The change of oscillation due to this interaction can be monitored using two different detection modes: amplitude modulation (AM-AFM) and frequency modulation technique[103] (FM-AFM). In FM-AFM, the tip is driven with a constant amplitude and the frequency shift $\Delta f = f - f_0$, is measured. Thanks to a feedback loop, Δf is maintained constant by adjusting the tip-sample distance. When operating nc-AFM in vacuum, the quality factor Q increases by several order of magnitude ($\approx 10^5$)[109]. Due to this, FM-AFM is more efficient in vacuum[110].

FM-AFM allows the separation of the elastic interaction from the dissipative interaction[103]. The minimum force gradient detectable in FM-AFM F'_{min} depends on the cantilever parameters (spring constant k and quality factor Q) and the detection bandwidth B, and can be written as[103]:

$$F'_{min} = \left(\frac{\partial F}{\partial z}\right)_{min} = \sqrt{\frac{4k(k_B T)B}{2\pi f_0 Q A_0^2}} \qquad \textbf{(2. 25)}$$

where A_0^2 is the mean-square amplitude of the driven cantilever vibration, k_B the Boltzmann constant and T the temperature, F the force interaction and z the distance between the tip and the sample. As shown in the equation above up (Eq. (2. 25)), we can use high-Q factor cantilevers to increase the sensitivity. As seen in Figure 2. 9, different feedback loops are present. The Phase locked loop (PLL) uses amplitude and phase of detected signal to obtain the frequency f and the frequency shift Δf. An amplitude feedback circuit keeps the amplitude constant by adjusting the excitation signal.

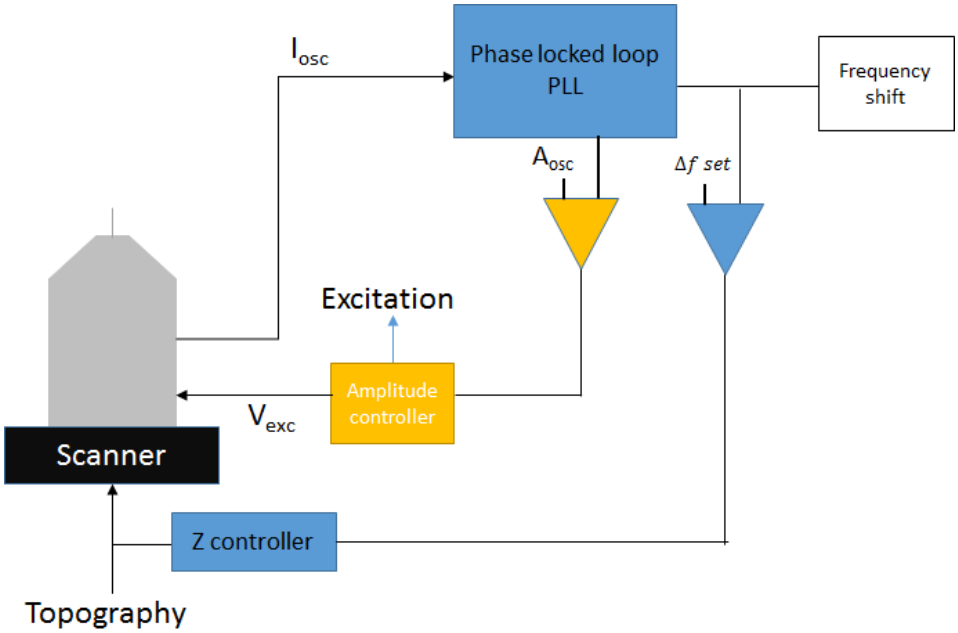

Figure 2. 9 : Schematic representation of a nc-AFM measurement with frequency modulation

2.2.3 Combined STM and non-contact-AFM

Using a conductive tip allows to combine STM and NC-AFM measurements at the same time. However, the tunnel current when the tip oscillates with an amplitude A_{osc}, oscillates also with time. The recorded average tunnel current can be written as[100]

$$\langle I_t(z, A_{osc})\rangle \approx \frac{I_t(z,0)}{\sqrt{4\pi\kappa A_{osc}}} \qquad \textbf{(2. 26)}$$

where $\kappa = \sqrt{2m\Phi}/\hbar$, with $\Phi = (\Phi_{tip} + \Phi_{sample})/2$. The oscillation of the tip causes a decrease in the tunnel current, and it is therefore necessary to move closer to the surface to have a tunnel current value identical to that of a non-oscillating tip.

2.2.4 Topography feedback modes for STM and non-contact AFM

In the chapters 4 and 5 both STM and nc-AFM UHV measurements were performed. Most often, the STM precedes the AFM experiments. STM imaging is done at a constant current I_t regulation, such that the tip follows the profile of constant density of states (often called STM topography). To perform an nc-AFM measurement at constant height, the z-feedback loop is set off and the voltage on the sample is reduced (generally set to zero). The tip scans the sample surface at a constant height while acquiring the Δf signal which corresponds to the difference in frequency recorded in comparison to the resonant frequency. By moving the tip closer or further away from the surface (steps about 10 pm), we can access the different forces and obtain a high resolution of the sample. The Figure 2. 10 presents the different image modes with the constant current regulation and the constant height mode.

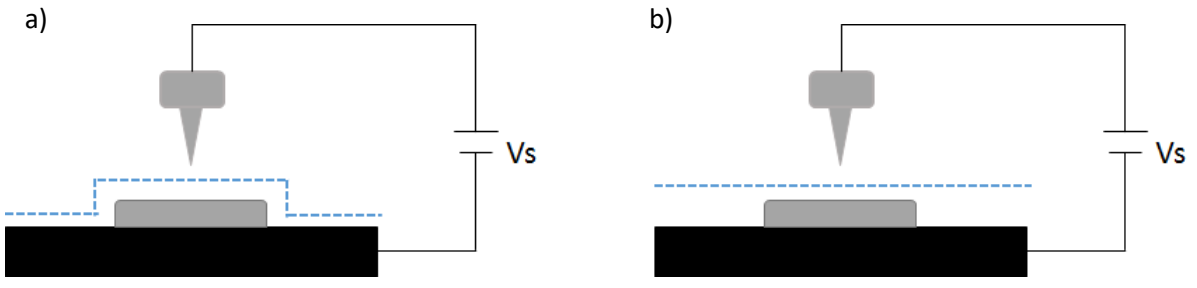

Figure 2. 10 : Imaging modes a) STM with constant current regulation with z feedback closed b) AFM constant height mode with z feedback open.

2.3 Type of STM/AFM probes

2.3.1 Metallic tips

In the chapter 3, when measuring under ambient conditions, n-doped silicon (n-Si) cantilever probes metallized by a platinum iridium alloy (PtIr) (SCM-PIT-V2, Bruker) are used. However, as the metal layer covering the tip is very fragile, the life of such probes is short.

Model	Manufacturer	Curvature radius [nm]	Spring constant [N/m]	Materials
SCM-PIT-V2	Bruker, US-MA	25	3	n-Si/ PtIr

Table 2. 1 : Characteristics of the SCM-PIT-V2 probes used according to the manufacturer's data

2.3.2 Length extensional resonator (LER) sensor

Silicon cantilevers used for nc-AFM measurements have spring constants of k ≈ 10 N/m and thus have the disadvantage of requiring large amplitudes (1-5 nm) to avoid the contact jump problem[111]. Due to this large amplitude, the capability in detecting short-range forces is limited because the cantilever only uses a small fraction of the oscillation cycle in the lower point. Also, combined STM/nc-AFM is not trivial due to the limited conductivity of the silicon cantilevers. To overcome this issue, a stiff probe has to be used and an example is the Kolibri sensor (KS) from SPECS. This piezoelectric quartz sensor is based on a length extensional resonator (LER) and has a separate wiring for the tunneling current signal. The oscillating quartz rod with the tungsten tip attached to its end has a spring constant k = 1080 kN/m and a resonant frequency of 1 MHz[109]. To avoid damage component during sputtering, a metallic shield covers the quartz resonator and electrodes. The oscillation of the rod is caused by the piezoelectric effect: the sinusoidal U_{exc} (see Figure 2. 11 a)) is applied on one side electrode and will create periodic contraction and extension of the quartz material and therefore oscillation of the tip. The conductive tip is isolated from the quartz resonator, which results in a separated readout of the tunneling current I_t from the oscillation current I_{osc}. The Figure 2. 11 presents a schematics of the Kolibri sensor with its different elements[109]. Due to the high stiffness of the probe, we can approach the tip really close to the surface (2-0.02 nm), which allows the possibility of recording short distance interactions. In the next part the noise comparison between the Kolibri and the Qplus is made. The Qplus sensor is a quark fork couple with an AFM tip[112].Typical parameter for a Qplus senor k= 1800 N/m and a resonance frequency about 23.41 kHz.

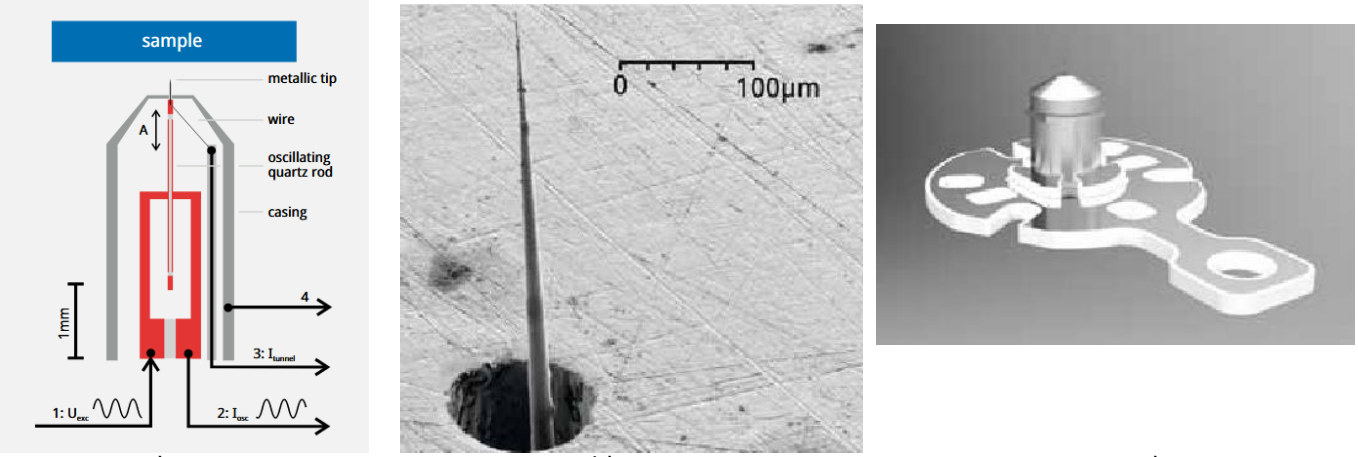

a) b) c)

Figure 2. 11 : a) Schematic drawing of the KolibriSensor b) SEM image of Kolibri tip c) Handle plate of the KolibriSensor. Extracted from[109].

2.4 Noise sources in AFM

AFM measurements are sensible to several types of noise sources that can limit the sensitivity or even prevent the measurement of certain physical properties. There are relevant noise contributions that need to be considered[113–115].

- Thermal noise
- Detection noise
- Frequency drifts caused by temperature changes

Thermal noise

The thermal noise $\delta f_{thermal}$ of a sensor with a measurement bandwidth B is given by[103]:

$$\frac{\delta f_{thermal}}{f_0} = \sqrt{\frac{k_B T B}{\pi k A_{osc}^2 f_0 Q}} \qquad \textbf{(2. 27)}$$

Detection Noise

The contribution of detection noise depends on the type of sensor used and the properties of the oscillation detection system. An important factor is the detection noise density η_q that denotes the precision at which frequency changes can be measured[113,116,117]. The frequency and force gradient noise can be written as:

$$\Delta k_{det} = \sqrt{\frac{8}{3}} \frac{k\eta_q B^{3/2}}{A_{osc} f_0} \quad \textbf{(2. 28)}$$

Values for the detection noise density were taken from Giessibl et al.[113] For the Kolibri that is $1.89\ fm/\sqrt{Hz}$ and $31\ fm/\sqrt{Hz}$ for Qplus at 4 K.

Frequency drifts caused by temperature changes

Temperature variation causes the drift of the natural frequency f_0. When performing an accurate AFM experiment, it is important to keep the frequency at its natural frequency. The oscillation frequency of a sensor changes slightly with the temperature. The material determines the amplitude of the drift, for example silicon cantilevers have a relative frequency variation linear with temperature with a value -35 ppm/K at room temperature[114]. Quartz sensors have a quadratic frequency shift with temperature. The natural frequency varies with the temperature as follows:

$$\frac{\delta f_{sensor}}{f_0} = -\chi (T - T_p)^2 \quad \textbf{(2. 29)}$$

T_p is the turnover temperature which depends on the crystal cut. Usually, for Kolibri sensor T_p is around $\approx 313\ K$. The temperature stability χ of the quartz got a very small value of $\chi = 35 \times 10^{-9}\ K^{-2}$. The noise related to this type of drift is:

$$\delta k_{tsdrift} = -2k\chi (T - T_p)^2 \quad \textbf{(2. 30)}$$

A more detailed analysis was made for tuning fork and different geometries of Qplus sensors[118].

Thermal noise and other noises for QPlus and Kolibri are summarized in Table 2. 2. Reasonable Q values are 50 000 at room temperature and rise up to 100 000 at 4 K for Kolibri sensor (SPECS), Q = 3000 for QPlus sensor[112] at room temperature and reaching up to 200 000 at 4 K.

Temperature	Sensor	$\delta k_{thermal}$ (N/m)	Δk_{det} (μN/m)	Δk_{drift} (mN/m) ΔT = 0.1 K at 300 K ΔT = 10 mK at 4 K
300 K	Qplus	0.032	25.7	0.012
	Kolibri	0.033	33.2	7.5
4 K	Qplus	0.0004	25.7	0.0012
	Kolibri	0.0027	33.2	0.756

Table 2. 2 : The summary of noise contributions for both QPlus and Kolibri sensors at 300 K and 4 K. The quality factor Q values taken for the calculations are 50000 and 3000 at 300 K and 100000 and 200000 at 4 K for the Kolibri and Qplus sensors respectively. The resonant frequency is 1 MHz for Kolibri and 23.41 kHz for Qplus sensor, spring constant is 1080 kN/m and, 1800 N/m for Kolibri and Qplus sensors. All noise sources were calculated for B = 100 Hz and A_{osc} = 100 with Eq. (2. 27), Eq. (2. 28) and Eq. (2. 30).

2.5 Our setups

2.5.1 Air ambient Atomic Force Microscope

The measurements under ambient conditions performed in Chapter 3 of this thesis were obtained with a Dimension Bruker Icon (Bruker, US-MA) (Figure 2. 12) equipped with a Nanoscope V controller and a PF-TUNA module with a wide calibration range from 20 pA/V to 100 nA/V. In this thesis, the 1nA/V range has been used to detect low currents. The Nanoscope V9.1 software is used to drive the microscope. Imaging with the Bruker ICON AFM does not require a complex set-up. The electrical contact between the sample and the plate on which the voltage is applied is established by a metal tab. The topography of the surface is measured using the deflection of the cantilever by detecting a laser beam reflected off the back of the cantilever onto a photodiode. Before and after each experiment, the vertical deflection setpoint relative to the support force (in nN) is calculated from the sensitivity of the optical system (in nm/V). The relationship between deflection and force is:

$$V_{ds} - V_{d0} = \frac{F}{s \times k} \qquad \textbf{(2. 31)}$$

Where V_{ds} is the vertical deflection setpoint, V_{d0} the vertical deflection, k the spring constant of the cantilever given by the manufacturer or by measurement of the thermal noise with the Thermal Tune function of the Bruker ICON[119].

Figure 2. 12: Photo of the Bruker ICON microscope.

2.5.2 UHV Joule Thomson Scanning Probe Microscope (JT-SPM)

The SPECS Joule-Thomson SPM (JT-SPM) is a low temperature setup operated under ultra-high vacuum (UHV). It has been used for the measurements in chapters 4 and 5. The JT-SPM allows scanning tunneling microscopy, non-contact atomic force microscopy and Kelvin Probe Force Microscopy (KPFM). With all this different types of probe microscopy the JT-SPM performs topographic, morphologic, electronic characterizations of samples at different temperatures, depending on the cryogenics used (77 K with liquid Nitrogen, 4.3 K with liquid Helium or 1.3 K with superfluid Helium formed with the Joule-Thomson stage). There is also a possibility of using a magnetic field up to 3 T. The system is composed of three chambers. The load lock chamber where samples are inserted, the preparation chamber where the samples and tips are prepared, and the analysis chamber where the JT-SPM is situated (see Figure 2. 13).

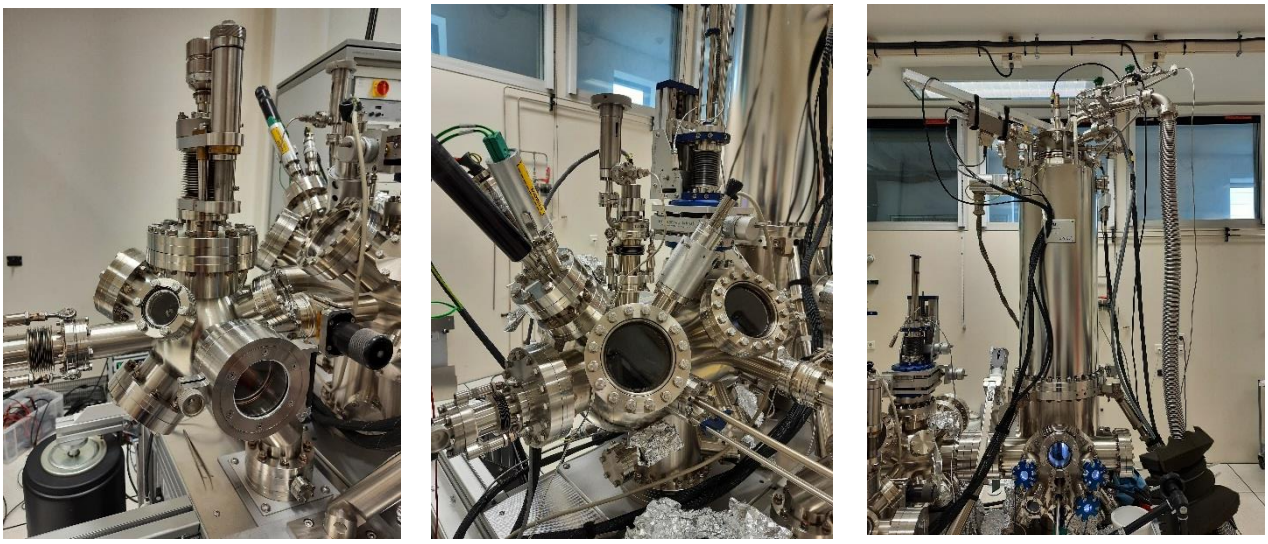

Figure 2. 13 : (left) Photo of the load lock side of the JT system (middle) photo of the preparation chamber of the JT system (right) Photo of the analysis chamber of the JT system.

Ultra High Vacuum (~10^{-10} mbar) in preparation and analysis chambers is obtained via the association of a scroll pump with a turbomolecular pump after a bake out of the chamber at T = 100-150°C and titanium sublimation pumping (TSP). To preserve the system of mechanical vibration induced by the turbomolecular and scroll pumps, the vacuum during the measurement is preserved via ionic pumps and TSPs. Tip and multiple samples can be transferred from ambient air to vacuum via the load lock chamber who is sealed with a Viton gasket with a base pressure of 10^{-8} mbar. Thanks to a manipulator, we can transfer samples and tips to the preparation chamber situated between load-lock and analysis chambers. It is equipped with an ion sputter gun for bombarding with high energy argon ions, a heating stage used for annealings, a Kentax 3-cell TCE-BSC evaporator and a Low-Energy Electron diffractometer (LEED).

In the analysis chamber, we have the JT microscope, with JT stage below liquid helium bath cryostat which is itself surrounded by another vessel of liquid nitrogen. Four parking positions for storage and cooling are available for samples and probes before introducing them into the microscope. The liquid nitrogen cryostat (21 liters) has to be filled about every 80 hours and the liquid helium one (9.5 liters) every 110 hours or more often. When the microscope is already thermalized to 4 K and no sample or tip is removed or inserted, the liquid helium consumption is about 0.10 liter /hour.

2.6 Tip and sample preparation for UHV experiments

2.6.1 Sputter of the Kolibri Sensor (KS)

In the previous part we have introduced the KS. However, before being able to carry out measurements with it it is necessary to clean the KS tip thanks to sputtering during 15-30 min with 3 keV argon ions, under a maximum pressure of $1x10^{-5}$ mbar. An example of cleaning is shown in Figure 2. 14. During the scanning, the tip can be sharpened with bias pulses and gentle tip indentation into the surface. In case of a tip crash on the surface, the tips can be recovered using Focused Ion Beam (FIB) technique.

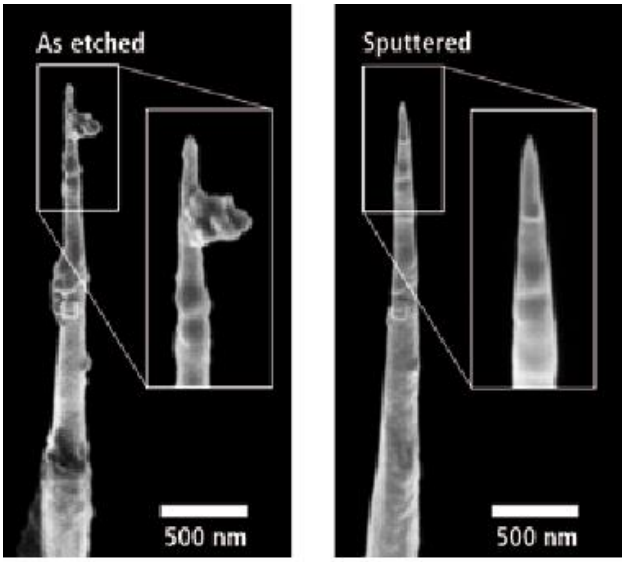

Figure 2. 14 : Scanning electron microscopy of the same tip, before and after sputtering with an AR^+ ion beam from Kolibri sensor (SPECS) booklet.

2.6.2 Deposition of molecules under UHV

To deposit the molecules under UHV on our substrate, we use the Kentax evaporator which is placed in the preparation chamber. The evaporator is composed of three crucibles in quartz with a shutter mounted on the top. This shutter makes it possible to deposit but also to co-deposit molecules from two or three different crucibles. The molecules in the crucibles are in the form of powder, which is heated using a tungsten wire until the sublimation. A thermocouple measures the temperature and permits to regulate the temperature of the power supply. The evaporator is mounted on a linear translation stage (170 mm) behind a gate valve, allowing loading molecules without venting out the preparation chamber. Before evaporating molecules, the crucible is degassed slowly up to remove water and solvent used in the synthesis process. A water cooling system prevents heating all crucibles when one is in use. Molecule deposition were made with the host substrate at ambient temperature.

2.6.3 Au(111) substrate

Au(111) (bought from MaTeck, Jülich, Germany) crystallizes in a faces centered cubic (fcc) structure with a lattice parameter of a = 2.950 Å. However, Au(111) surfaces show off an anisotropic " herringbones structure". This pattern is formed by a stress-induced surface contraction along the $[1\bar{1}0]$ direction[120–122] (Figure 2. 15 a)). In half of the reconstruction unit cell, the surface atoms occupy hexagonal close packed (hcp) sites, while in the other adjacent half they occupy fcc sites. Stripes are formed by the surface atoms occupying bridge sites between the fcc and the hcp regions (Figure 2. 15 b). To evaporate molecules or perform STM/nc-AFM on the Au(111) substrate, it needs to be cleaned. To clean the Au(111) surface, various cycles of 0.8 keV Ar^+ sputtering (10 min) and annealing at 700 K are performed.

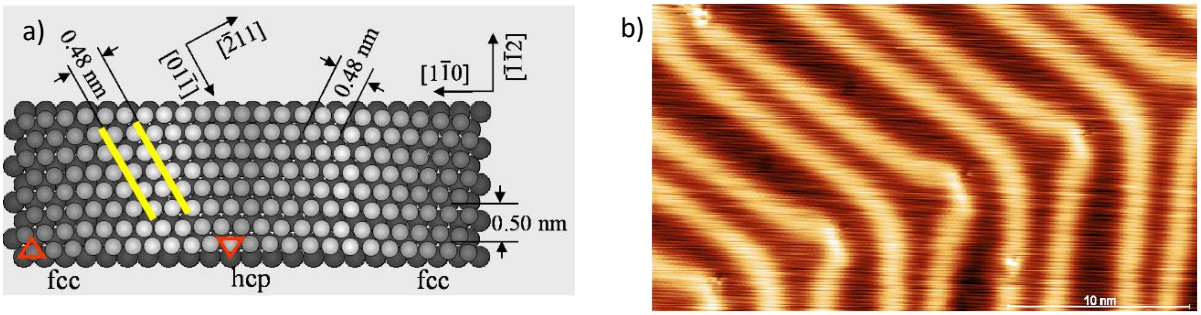

Figure 2. 15 : a) A model of the reconstructed Au(111) surface from[122]. b) STM image of herringbones structure on Au(111) substrate.

2.7 KPFM spectroscopy: frequency shift versus bias

From the electrostatic force described in the equation (2. 12), we can write the $\Delta f(V_{bias})$ as:

$$\Delta f(V_{bias}) = -\frac{f_0}{4k}\frac{\partial^2 C(z)}{\partial z^2}(V_{bias} - V_{CPD})^2 \qquad \textbf{(2. 32)}$$

A tip-sample system is modeled by an ideal plate capacitor $C(z) = \varepsilon A/z$, where A is the surface area of the plate capacitor, ε the dielectric constant of the dielectric material between the plates and z the distance between the tip and the substrate. The equation (2. 32) is:

$$\Delta f = -\frac{f_0}{2k}\frac{\varepsilon_0 A}{z^3}(V_{bias} - V_{CPD})^2 \qquad \textbf{(2. 33)}$$

To have a simpler equation, we can write it as:

$$\Delta f = A + B(V_{bias} - V_{CPD})^2 \qquad \textbf{(2. 34)}$$

The coefficient A represents all the interactions independent on the tip bias like van der Waals forces and image charge contributions. B is the capacitance signal (Hz/V²).

The contact potential difference value depends on the work functions of the tip and the sample, it is defined as:

$$V_{CPD} = \frac{\Phi_{sample} - \Phi_{tip}}{e} \quad \textbf{(2. 35)}$$

The $\Delta f(V_{bias})$ spectroscopy experiment consists in recording the frequency shift in function of the applied bias on the sample. From this measurement, we extract a parabolic curve of the frequency shift in function of the bias applied, from which we can extract various information like the capacitance, the surface potential[123] and van der Waals interaction. The different contributions of the signal can also be studied[124]. A calibration is necessary[125] for quantitative analysis. If the V_{CPD} values are measured over different surfaces with the same tip apex and work function, by knowing one of the two work functions, the other can be calculated by using:

$$\Delta\Phi = e(V_{CPD}(B) - V_{CPD}(A)) \quad \textbf{(2. 36)}$$

where $V_{CPD}(A)$ and $V_{CPD}(B)$ correspond to the bias for nullified electrostatic contribution for surface A or B respectively.

At the atomic scale, the CPD is defined as LCPD (local contact potential difference). The LCPD refers to the local work function, which illustrates the short-ranged atomic scale variation of work function on metallic surfaces[126–128]. An example of $\Delta f(V_{bias})$ spectroscopic curve made on Au(111) is presented in Figure 2. 16.

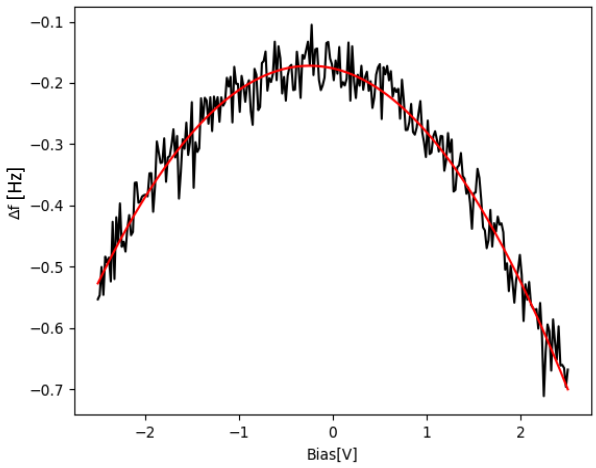

Figure 2. 16 : Frequency shift versus bias spectroscopy made on a Au(111) substrate (A_{osc} = 100 pm). The black line is the raw value of measurements and the red line is the fitted parabolic curve using the Eq. (2. 34).

Δf spectroscopy done in this thesis are in constant height mode with z-feedback loop opened. Before launching the spectroscopy, nc-AFM images are acquired. The Δf signal of the AFM image permits to have an estimation of the tip-sample distance before the spectroscopy. Before launching the spectroscopy measurement, some adjustments have to be made by lifting up the tip of 100-150 pm from the nc-AFM scanning condition, to reduce the current on the molecule and to avoid perturbing the Δf signal[129]. Increasing the oscillation amplitude of the tip increases the signal to noise ratio of Δf. A bias sweep is made in a bias range selected for the experiment.

2.8 Conclusion

In this chapter, the principles of scanning probe microscopy techniques have been explained, including STM and AFM. All experimental setups used in this thesis have been detailed. The ambient air AFM, the UHV JT-SPM and the oscillator used for combined STM and nc-AFM experiments were described. The characteristics of the Au(111) substrate and the method of deposition of molecules for our UHV experiment have been presented. Noise sources, topography imaging modes and the KPFM grids spectroscopy experiments have been explained.

Chapter 3: Charge transport through CsCoFe Prussian blue analogue (PBA) nanocrystals

PBA nanocrystals (here with sizes in the 15-50 nm range) are nano-objects at the frontier between molecules and bulk materials, and have molecular properties that can be used for different applications[130] such as gas storage[131–133], environmental purification[134,135], cathode materials for batteries[136–138] and also for their magnetic properties for information storage[139]. Keggin and Miles proposed a structure for Prussian blue in the 1930s based on X-ray diffraction data[140]. This structure consists of a face-centered cubic (fcc) arrangement of transition metal elements (originally: Fe) bridged by cyanide ligands, while additional transition metal elements are placed on interstitial sites to preserve the charge neutrality of the structure. A wide variety of Prussian Blue Analogues (PBAs) has been synthesized using different transition metals such as Cr, Mn, Co[141,142]. In this chapter, we present an electrical investigation of isolated nanocrystals of PBAs composed of $Cs\{Co^{III}[Fe^{II}(CN)_6]\}$ noted CsCoFe thereafter. CsCoFe PBAs can adopt a ferrimagnetic state[143,144], making CsCoFe nanocrystals interesting candidates as molecular magnets. The results presented in this chapter consist of a preliminary study of the electrical properties of PBA nanocrystals by AFM at room temperature (including the sample preparation steps), in view of further studies at low temperature and under magnetic field. The CsCoFe nanocrystal samples were provided by Pr. Talal Mallah from the Institute of Molecular Chemistry and Materials (ICMMO – Orsay).

3.1 Structure and properties of Prussian blue analogue

3.1.1 Structure of Prussian Blue analogues (PBAs)

The structure of PBAs is shown in Figure 3. 1. The general formula is given by $A_xP^j[R^k(CN)_6]_{1-y}.wH_2O$, where A is an alkali cation; P and R are transition metals with an octahedral bonding environment of carbon and nitrogen, respectively; y is the number of *hexacyanometallate* vacancy sites; and w is the amount of water molecules[136,145,146]. The oxidation state is represented by j and k for the P and R transition metals, respectively. The transition metals are organized in a fcc arrangement bridged by the cyanide ligands forming a cubic structure[147]. The charge neutrality of the system is due to a relationship between the transition metals oxidation states, vacancy content and alkali cations. A large number of metallic atoms can be substituted into PBA structure on the A, P and R sites[130,136,143,148]. As for the site P, the most frequently used elements are 3d transition metal. Up to six 3d electrons can

accommodate the R site. The transition metal elements of the P and R sites can take several oxidation states[130,136,149].

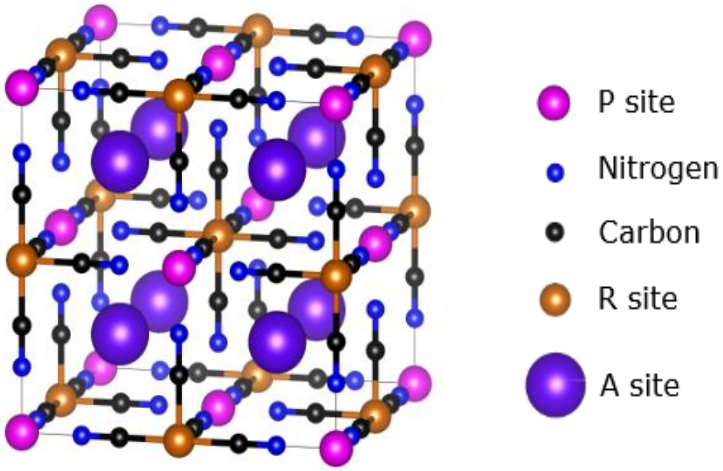

Figure 3. 1 : Schematic view of the Prussian blue analogue (PBA) crystal structure. The crystal structure is presented with no vacancies and all interstitial sites occupied. Adapted from[147].

3.1.3 Cyanide bridge

The cyanide (C-N) ligands have an essential role in PBA crystals. Cyanide is a ligand with a negative charge that acts as σ donor and π acceptor[145]. Transition metal elements form octahedral complexes with cyanide ligands[150]. The octahedral coordination affects the energy levels of the transition metal d electron orbitals as shown in Figure 3. 2. If we distribute six negative charges uniformly over the surface of a sphere, the d orbital remains degenerate. However if the six negative charges are at the vertices of an octahedron like cyanide ligands, the d orbital is not degenerate anymore, d_{xy}, d_{xz}, and d_{yz} orbitals see their energy levels reduced, while $d_{x^2-y^2}$ and d_{z^2} orbitals increase in energy (see Figure 3. 2). The crystal field splitting energy Δ_0, depends on the nature of the ligand: it is large ($\Delta_0 \approx 33200\ cm^{-1}$) in the case of cyanide which is at the end of spectrochemical series.

In this work, the PBA is CsCoFe, in which Fe is attached to the carbon of the cyanide bridge, and Co to the azote. The interstitial sites are occupied by Cs^+ ions, which play the role of counter cations[151] (see Figure 3. 3).

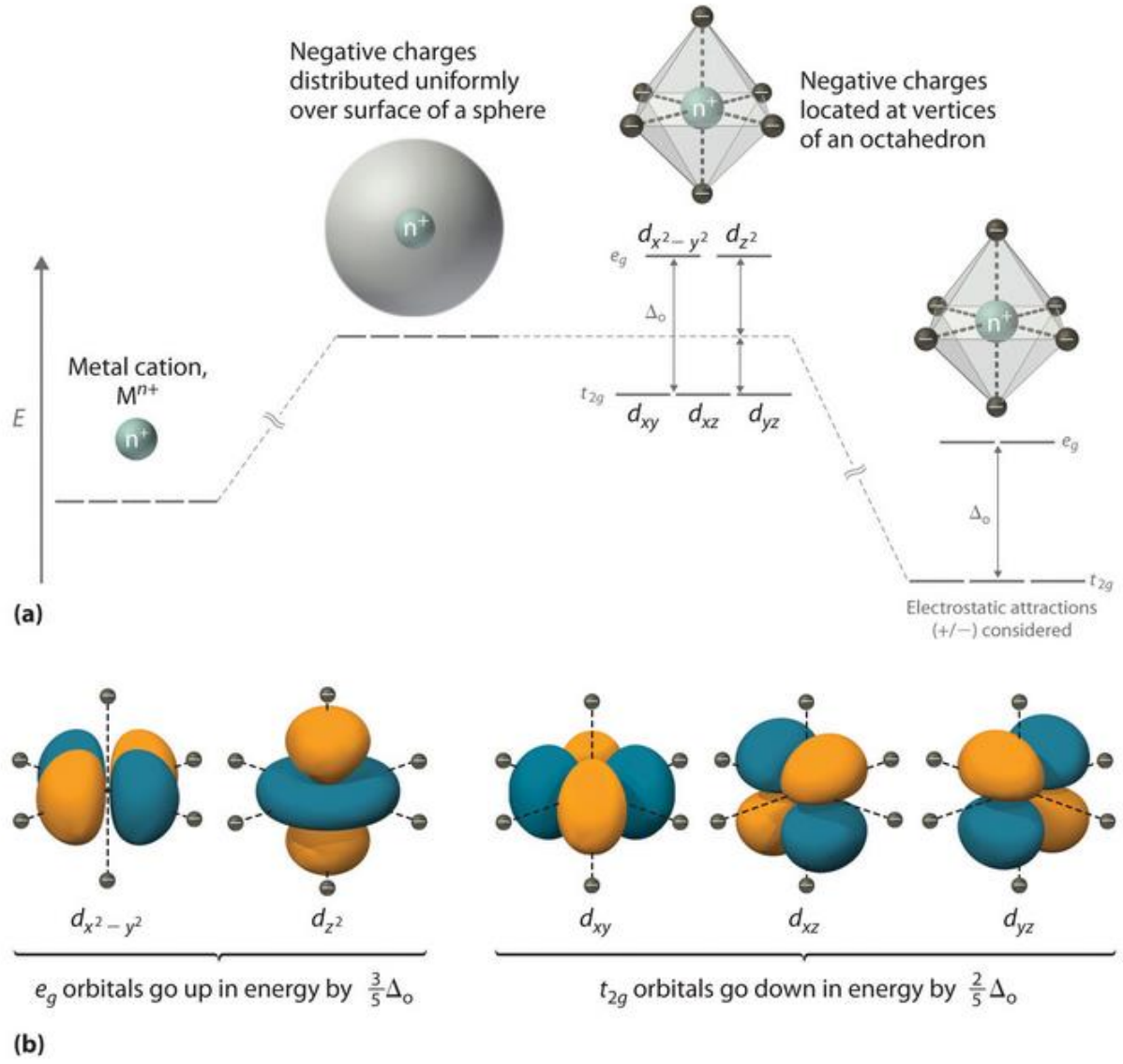

Figure 3. 2: Degeneracy lifting of transition metal energy levels surrounded by an octahedral arrangement of negative charges. (a) Uniformly distributed charges on a spherical surface around the metal ion leave the energy level of d orbitals degenerate; charges located at each vertex of the octahedron induce a d orbital splitting. (b) Representation of the geometry of the d orbitals of the metallic ion. Adapted from[150].

CsCoFe is made from low diamagnetic spin (S = 0, $t_{2g}^6 e_g^0$) Co^{III} and Fe^{II} metal ions. The structure at the nanoscale dimension brings interesting properties : for example, CoFe PBA nanocrystals in the powder form show an electron transfer at low temperature upon light irradiation, leading to a magnetic Co^{II} (S = 3/2, $t_{2g}^5 e_g^2$) – Fe^{III}(S = 1/2, $t_{2g}^5 e_g^0$) state[152,153]. CsCoFe nanocrystals exhibit a fast (ps range) electron transfer at ambient temperature upon light irradiation[144,153,154] (the electronic configuration of transition metals are shown in Figure 3. 4.

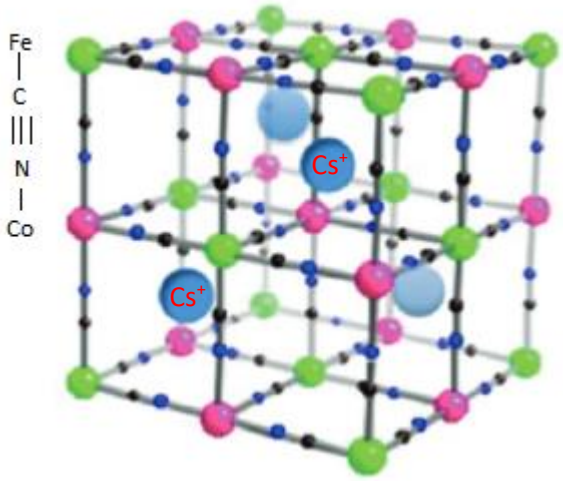

Figure 3. 3 : View of the unit cell of the fcc structure of the PBA CsCoFe nanocrystals, in which Fe(II) is represented in green and Co(III) in purple. Adapted from[172].

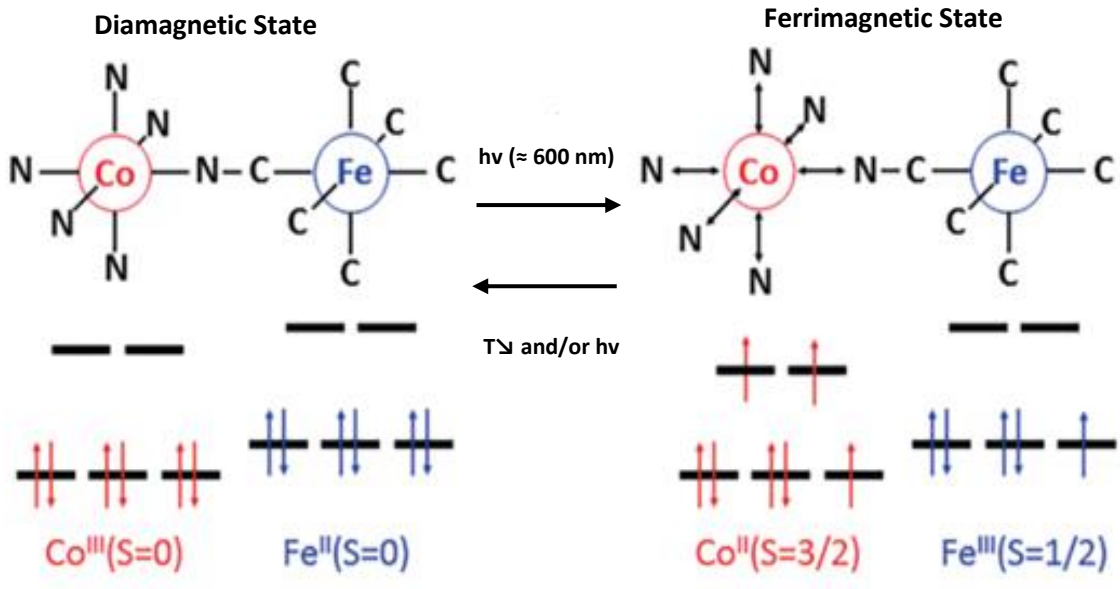

Figure 3. 4 : Schematic representation of the electronic structure changes upon charge transfer in CsCoFe. Left: low spin state. Right: high spin state established upon irradiation with red light (≈600 nm) due to a charge transfer: the structure now has a spin S=1/2 for Fe^{III} and S=3/2 for Co^{II}. Adapted from[154].

The reversible and the persistent modification of magnetic properties by external stimuli hence constitutes one of the most interesting properties of PBAs[144,152,155,156]. It has been reported that PBAs composed of Fe and Co metal ions exhibit a reversible change between paramagnetic to diamagnetic[143,157–159], as illustrated in Figure 3. 5: the molar magnetization (M) versus the magnetic field (H) demonstrates the magnetization change before and after illumination, while the molar

magnetization (M) versus temperature (T) demonstrates the magnetization relaxation after heat treatment.

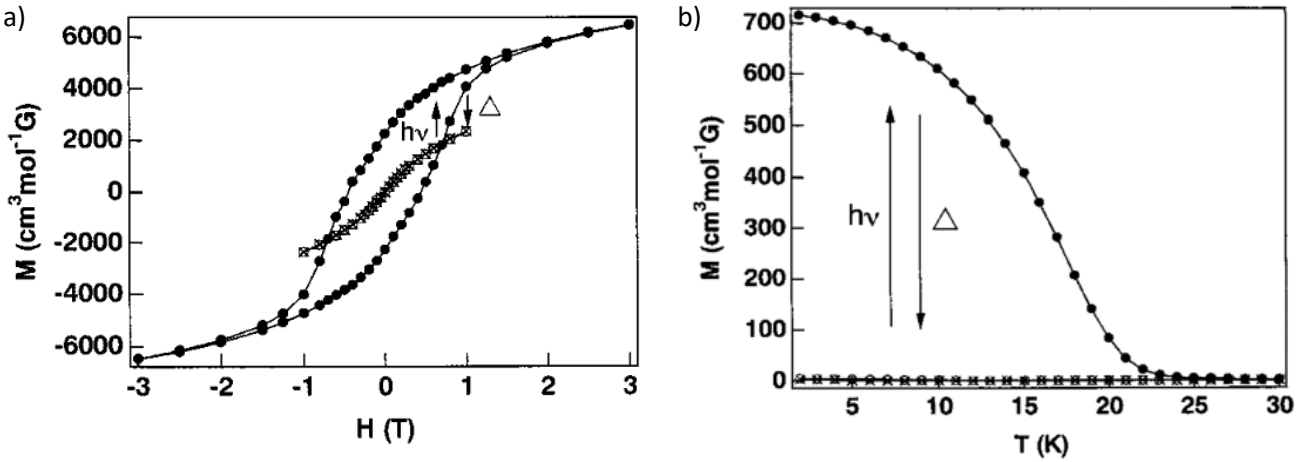

*Figure 3. 5 : a) Hysteresis loops for $Rb_{0.66}Co_{1.25}[Fe(CN)_6].4.3H_2O$ at 2 K **(o)** before illumination, **(●)** after illumination, **(x)** after thermal treatment at 150 K. (**o** and **x** fall on the same line) b) Dependence of the magnetization of $Rb_{0.66}Co_{1.25}[Fe(CN)_6].4.3H_2O$ under an applied field H = 0.5 mT before (empty dots) and after (black dot) light irradiation, and after thermal treatment at 150 K (crosses). Adapted from[32].*

3.2 Charge transport

Two models are presented here, which are later used to study the charge transport across PBA nanocrystals (NCs): (i) resonant transport through molecular orbitals (metal-molecule-metal junction) and (ii) transport through a double Schottky barrier.

3.2.1 Electron transmission and Laudauer expression for the current through a Metal-Molecule-Metal (MMM) junction

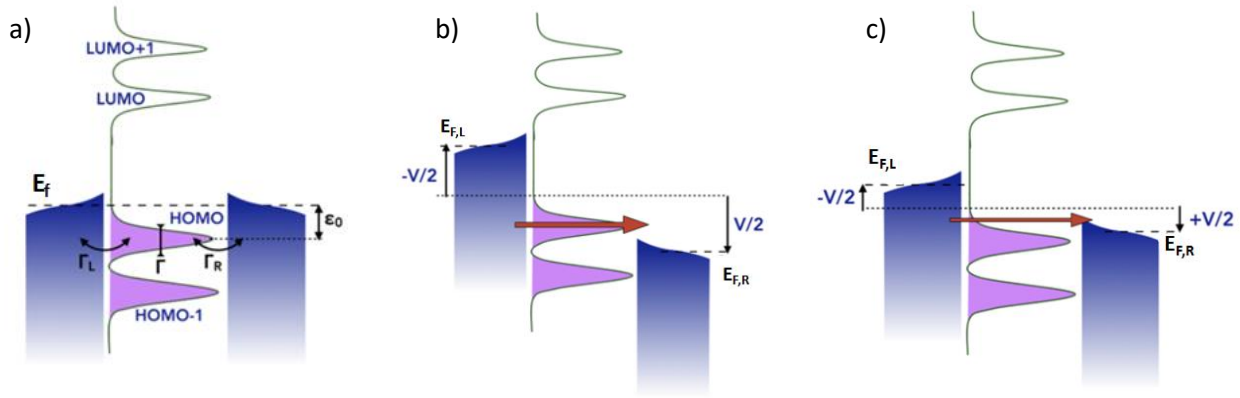

Figure 3. 6 : a) Simplified energy diagram of a molecular junction at V=0V; b) Coherent, resonant, electron transport at a positive bias V > 0V; c) Coherent, off-resonant, electron transport at a positive bias V > 0V. Adapted from[52].

When a molecule is contacted by two metallic electrodes and a potential difference is applied, charge transport will take place via a tunnel transfer[52,160]. Molecular orbitals are used to calculate the electronic configuration, spatial distribution and energy of the electrons in the molecule. A molecule contacted between two metallic electrodes will see its energy level translate and broaden[160]. The HOMO (highest occupied molecular orbital), and the LUMO (lowest unoccupied molecular orbital) define the HOMO-LUMO gap[161–163].

Landauer was the first to develop an approach to express mathematically the tunnel current through a molecular junction[161,164]:

$$I = \frac{e}{\pi\hbar}\int T(E)\,[f(E,E_{F,L}) - f(E,E_{f,R})]dE$$
$$f(E,\varepsilon) = \left(1 + exp\left[\frac{(E-\varepsilon)}{kT}\right]\right)^{-1} \quad \textbf{(3. 1)}$$

in which $f(E,\varepsilon)$ is the Fermi distribution function at the left (L) or right (R) electrode, e the electron charge, k the Boltzmann constant, T the temperature, $\hbar$ the reduced Planck constant, $\left|E_{F,L} - E_{F,R}\right| = eV$, V the applied voltage and T(E) the electron transmission function given by

$$T(E) = \frac{\Gamma_L\Gamma_R}{(E-\varepsilon_0)^2 + (\Gamma/2)^2} \quad \textbf{(3. 2)}$$

in which Γ_L and Γ_R describe the coupling with the left/right electrodes, $\Gamma = \Gamma_L + \Gamma_R$, and ε_0 is the energy position of the involved molecular orbital (see Figure 3. 6). Considering a symmetrical junction, the integration of the Equation (3. 1) gives the following expression for the current:

$$I = \frac{e}{\pi\hbar}\frac{\Gamma_L\Gamma_R}{\Gamma}\left[arctan\left(\frac{2\varepsilon_0 + eV\frac{\Gamma_L - \Gamma_R}{\Gamma} + eV}{2(\Gamma)}\right) - arctan\left(\frac{2\varepsilon_0 + eV\frac{\Gamma_L - \Gamma_R}{\Gamma} - eV}{2(\Gamma)}\right)\right] \quad \textbf{(3. 3)}$$

Named single energy level (SEL) model, the equation (3. 3) give an S-like shape I(V) curve at low bias (see Figure 3. 7). The parameter ε_0 controls the position of the resonant transport step and curvature of the S-like shape at low voltage. The coupling $\Gamma_{L,R}$ controls the current amplitude. If $\Gamma_L \neq \Gamma_R$, an asymmetry appears in the I(V) curves, it can be the case experimentally when the molecule has a larger interaction with one electrode than another[165] or is highly coupled to an electrode by an anchoring group[166].

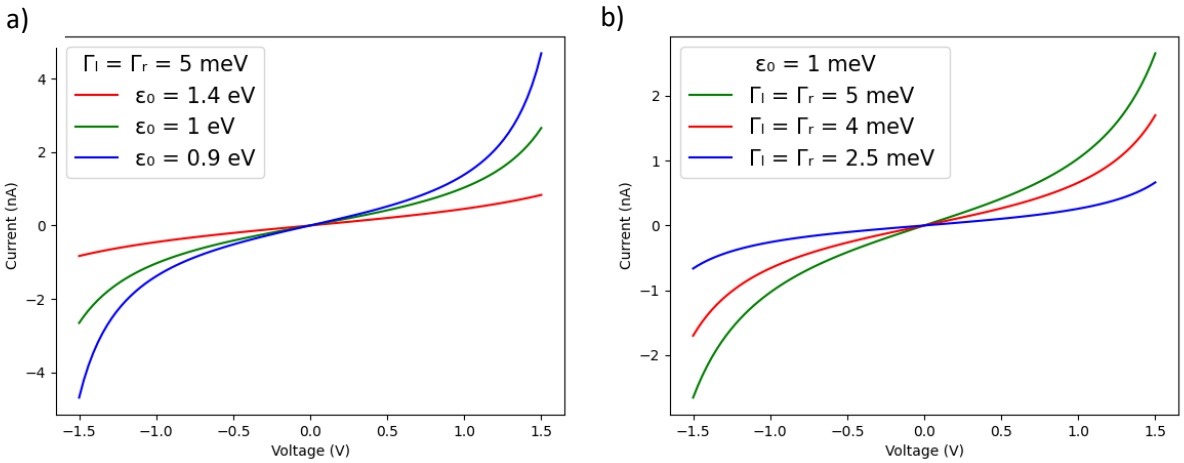

Figure 3. 7 : a) simulated I(V) curves for different values of the energy level ε_0 and for $\Gamma_L = \Gamma_R = 5$ meV. b) Simulated I(V) curves for different values of the coupling energy $\Gamma_L = \Gamma_R$ and for $\varepsilon_0 = 1$ eV.

3.2.2 Double Schottky barrier model

Schottky barriers (SBs) are often formed at semiconductor/metal contacts and affect the electronic transport through the semiconductor. SB heights can be extracted from I-V measurements in a single diode model[167–169], when the metal-semiconductor-metal junction presents a Schottky character on one side, and an ohmic character on the other side. Here, we apply a simple model to describe the

conduction in a two-terminal device in which two rectifying contacts are present. The model allows extracting both SB heights simultaneously[170,171]. We consider a p-type nanocrystal (NC) in accordance with Bonnet *et al*.[172] As illustrated in Figure 3. 8 the SB height is defined as

$$\Phi_B = \Phi_m - \chi_S \qquad \textbf{(3. 4)}$$

where ϕ_B is the SB heights for hole injection and ϕ_m is the metal work fonction, χ_s is the semiconductor electron affinity.

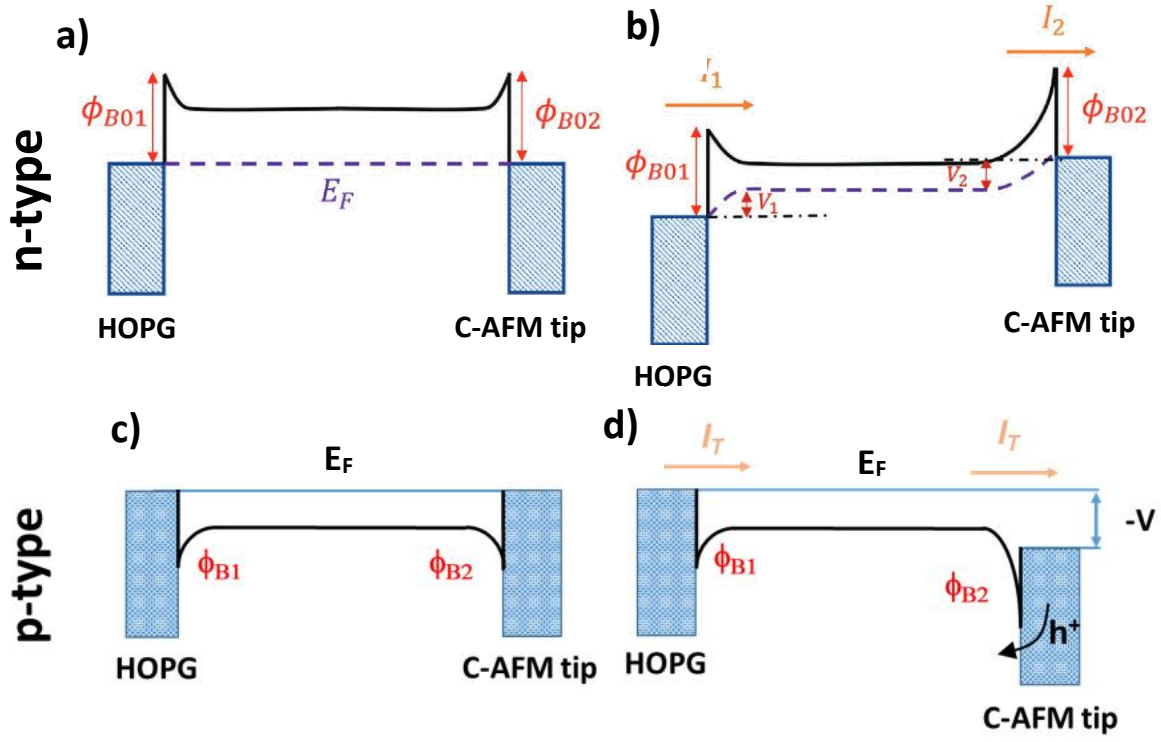

Figure 3. 8 Energy diagram of the HOPG//NC//C-AFM tip junction with two SBs for a n-type semiconductor a) without applied bias b) after applied bias, +V is applied on the C-AFM tip. c) Energy diagram of the HOPG//NC//C-AFM tip junction with two SBs without applied bias for a p-type semiconductor. d) Energy diagram of the same junction with a bias -V applied on the HOPG substrate. Adapted from [171].

This type of junction can be modeled using two back-to-back Schottky diodes (Figure 3. 9 a)). Based on thermionic emission, the current can be analytically obtained as[171]:

$$I_T = \frac{2I_{S1}I_{S2}sinh\left(\frac{qV}{2kT}\right)}{I_{S1}e^{\frac{-qV}{2kTn_1}} + I_{S2}e^{\frac{qV}{2kTn_2}}} \quad \textbf{(3. 5)}$$

$$I_{S1,S2} = S_{1,2}A^*T^2exp\left(-\frac{\Phi_{B01,B02}}{kT}\right)$$

where I_{S1}, I_{S2} are the reverse saturation current at the two contacts, A^* is the Richardson constant, T is the temperature, k is the Boltzmann constant, $S_{1,2}$ are the areas of the junctions and $n_{1,2}$ ideality factor. Here, we assumed that the voltage drops at the junction are V/2 on each side. Figure 3. 9 shows examples of simulated I-V curves with or without saturation within the voltage range, or with asymmetrical behavior due to different SB heights.

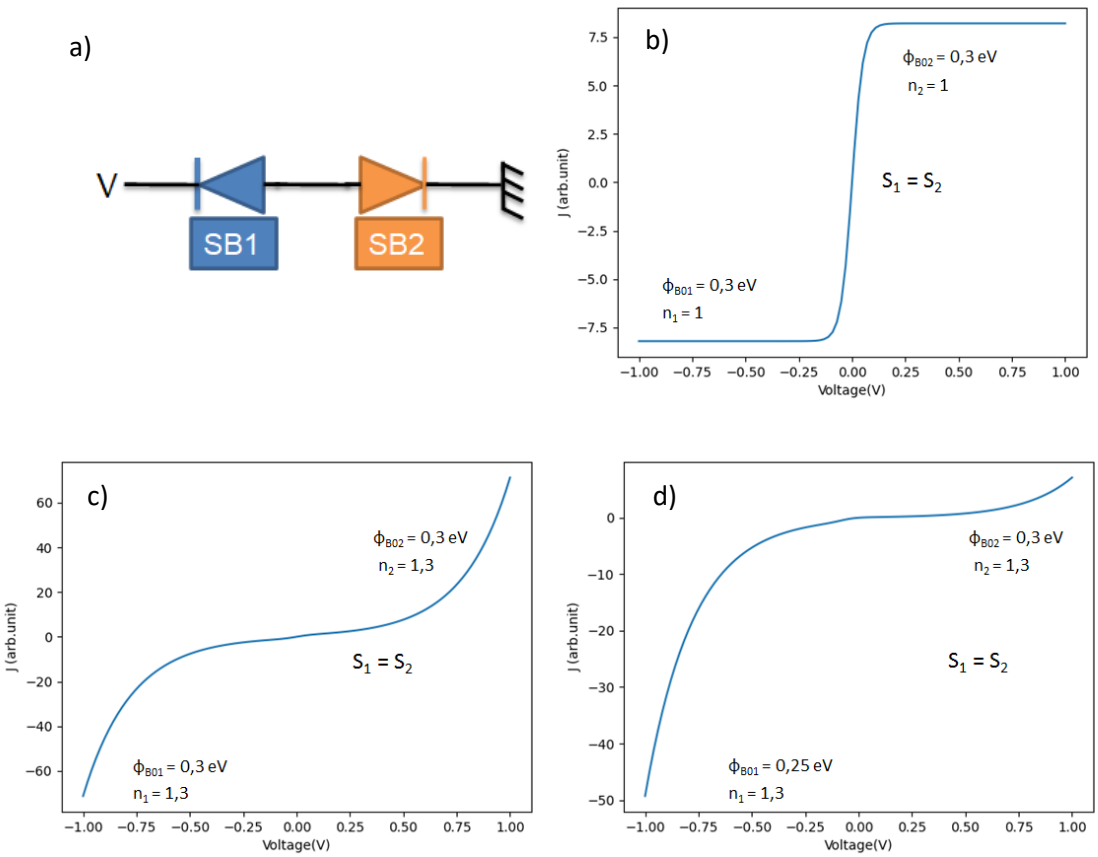

Figure 3. 9 : a) Equivalent circuit modeled by Eq. (3. 5). b) Simulated I-V characteristics for contact using ϕ_{B01} = ϕ_{B02} = 0.3 V, the same junction area S_1 = S_2, and a perfect ideality factor (n=1). c) Simulated characteristics, introducing an ideality factor n=1.3. c) Simulated I-V characteristic using asymmetric barrier heights ϕ_{B01} =0.25 V, ϕ_{B02} = 0.3 V, S_1 = S_2, and an ideality factor n=1.3.

3.3 AFM study of isolated 15/30/50 nm PBA nanocrystals

This part reports the physical characterization of PBA CsCoFe nanocrystals deposited on HOPG using a Dimension ICON atomic force microscope (AFM) in ambient air. The nanocrystals must be electrically isolated from neighboring nanocrystals (and only in contact with the substrate) in order to avoid leakage current between nanocrystals. The impact of the size of the nanocrystal on the current is observed in sections 3.4 and 3.5, and an electronic analysis is made, showing the relevance of the double Schottky model with respect to experimental data.

3.3.1 Sample preparation protocol

We received the HOPG substrate with PBAs from Pr Talal Mallah from the Institute of Molecular Chemistry and Materials of Orsay. The CsCoFe PBAs synthesized by his group was described in ref [144,151] and the main steps can be summarized as follows: an aqueous solution (100 mL) containing $CoCl_2.6H_2O$ (0.2×10^{-3} mol, c= 2×10^{-3} M) and CsCl (0.4×10^{-3} mol, c = 4×10^{-3} M) is added rapidly in an equal volume of an aqueous solution of $K_3[Fe(CN)_6]$ (0.2×10^{-3} mol, c = 2×10^{-3} M) under vigorous stirring. The solution is then stirred for one hour. A HOPG substrate is then cleaved using a Scotch tape and immediately immersed in the colloidal solution. The vial temperature is maintained at room temperature. The substrate is removed from the solution after 20 seconds of immersion, and rinsed thoroughly with water and then methanol. It is finally dried under vacuum for several hours. The samples are stable over time in ambient air and at room temperature. They are nevertheless kept under nitrogen environment for storage purposes, in order to avoid surface contamination.

3.3.2 Organization of the PBA on HOPG substrate

The tapping mode AFM measurements are obtained with a Dimension Icon microscope (Bruker) with a Nanoscope V controller. Platinum-iridium coated tip SCM-PIT-V2 from Bruker (apex radius = <25 nm, k = 2.8 N/m, Resonance Frequency = 75 kHz) have been chosen to perform tapping imaging.

Typical images of the CsCoFe nanocrystals for the different sizes and freshly deposited on HOPG substrates from a colloidal solution are presented in Figure 3. 10. Tapping mode AFM images confirmed the presence of mainly a monolayer on the HOPG substrates. Due to the deposition method in solution, not perfectly controlled, the substrate with the 30 nm nanocrystals presents a lower surface coverage around 8.7×10^{-5}, to be compared with the other samples with surface coverage close to 1. For samples

with a high coverage with nanocrystals size of nominal values of 15 and 50 nm, histograms of heights show a Gaussian distribution centered at 15.8 ± 4.9 nm and 42.4 ± 18.1 nm respectively.

For the 30 nm sample with a lower surface coverage, the grain recognition analysis is more appropriate for this sample. The histograms of grain heights show a Gaussian distribution centered at 26.9 ± 7.2 nm. These surface analyzes are in good agreement with TM-AFM and TEM characterizations presented previously on CsCoFe[172].

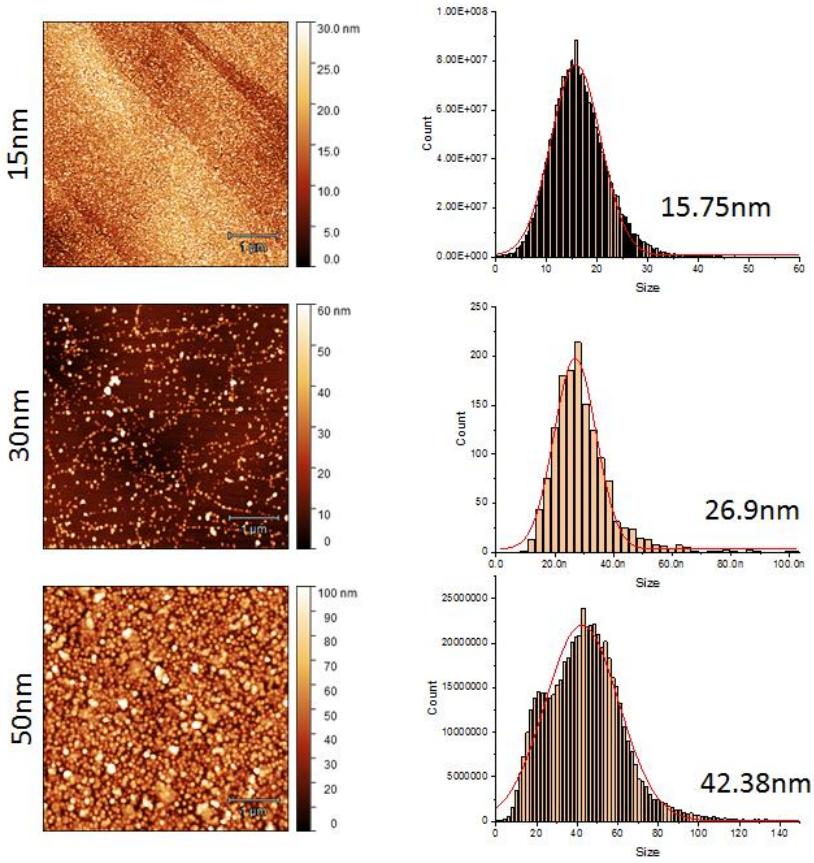

Figure 3. 10 : Topographic TM-AFM images for the three sizes of CsCoFe nanocrystals deposited on HOPG substrates and corresponding histograms of heights and grain height recognition of CsCoFe layer. Average heights and the standard deviations were obtained from the fit of the histogram of heights with a Gaussian distribution (red line).

The Figure 3. 11 a)-c) shows images of isolated CsCoFe nanocrystals of nominal 15, 30 and 50 nm heights, together with corresponding height profiles. We find the nominal characteristic dimensions for each nanocrystal with, however, a convolution effect due to the radius of curvature of the AFM tip (estimated by the supplier around 25 nm).

Due to the low interaction force between the nanocrystal and the substrate, obtaining the topography of our sample by contact-mode AFM is not possible despite very low pressing forces because PBA nanocrystals are swept from the scan area (see Figure 3. 11 d)) during contact mode scanning.

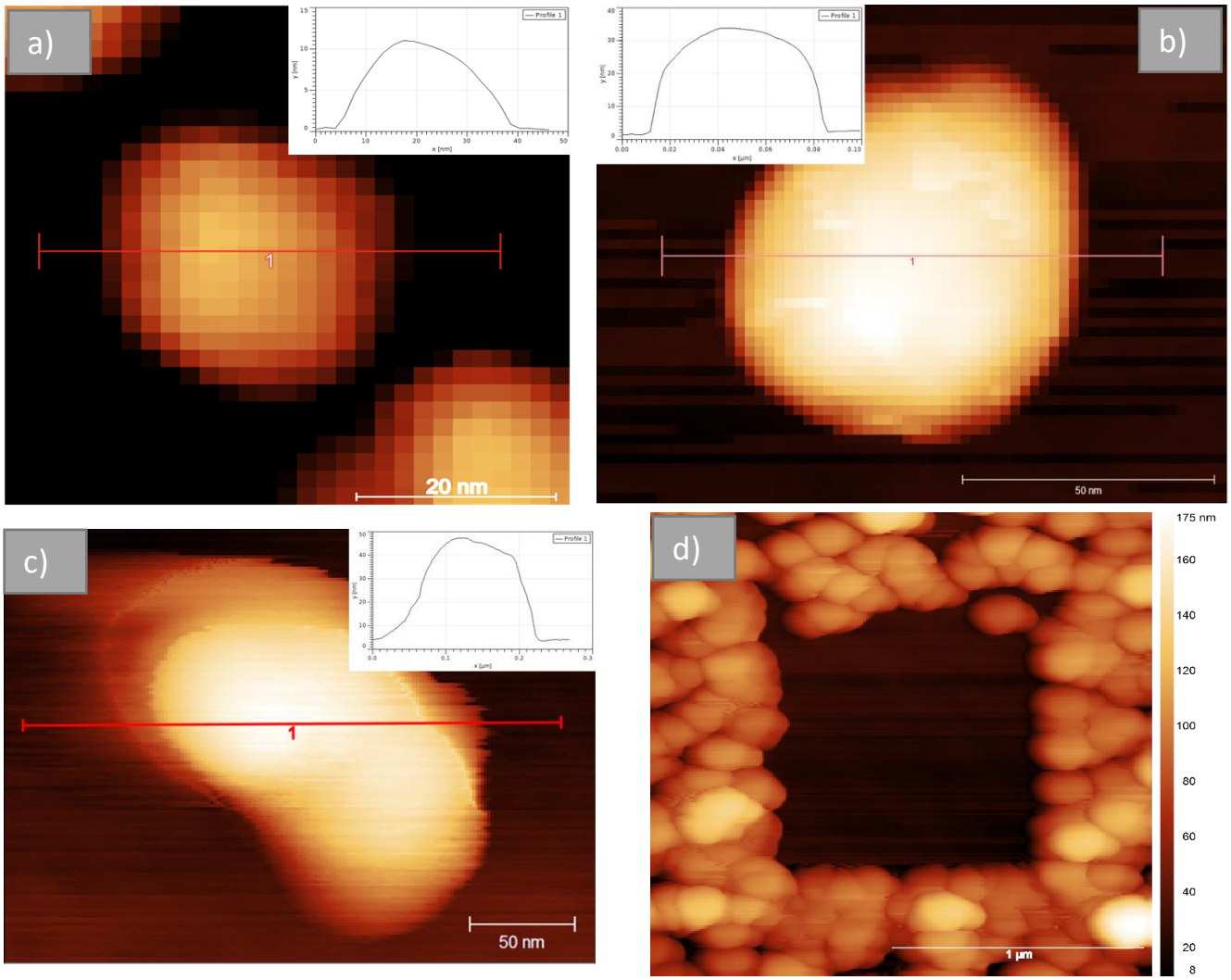

Figure 3. 11 : Example of different isolated PBA nanocrystals on the substrate of 15 nm a), 30 nm b), 50 nm c) with their profile along the red line. d) Tapping-mode AFM image after performing a smaller contact-mode AFM scan using a force of 5 nN on 50 nm PBAs. The area scanned in contact-mode is empty from nanocrystals.

3.4 Variable force electrical characterization of 15 nm PBA nanocrystals

3.4.1 Protocol for electrical characterization

The measurements performed in this part were obtained with a Dimension Icon microscope (Bruker) equipped with a Nanoscope V controller and a conducting-AFM PF-TUNA module that enables to record currents down to a few pico-amperes. Platinum-iridium coated tip SCM-PIT-V2 from Bruker (apex radius = <25 nm, k = 2.8 N/m, Resonance Frequency = 75 kHz) have been chosen in order to perform tapping-mode and contact-mode AFM, together with electrical measurements. To circumvent issue of sweeping nanocrystals described in part 3.3.2, the following methodology is used: (i) the

topography is first acquired with the AFM tapping mode; (ii) an isolated PBA nanocrystal is selected; (iii) a focus (zoom-in) on the chosen nanocrystal is progressively achieved with a final scan size of about 10 x 10 nm; (iv) the driving amplitude of the AFM cantilever is set to zero in order to stop the cantilever oscillation; (v) the AFM tip is gently brought into contact with the nanocrystal by gradually increasing the pressing force as measured from the cantilever static deflection. A typical force for the I-V acquisition is fixed around 15 nN. Around 200 I(V) curves are then successively recorded by applying a voltage ramp between -1V and +1V. The voltage ramp is applied in the forward and backward direction. After the measurement a new acquisition of the topography was made to verify that the molecule was not damaged.

3.4.2 Variable force electrical characterization

Before realizing the I(V) spectroscopy on PBA nanocrystals, it is important to characterize the substrate as a reference. A 10 x 10 nm² grid was recorded with a 50 nm step between each point and at each point a voltage sweep from -1 V to +1 V was made in the forward and backward direction with a 1 nA/V sensitivity for the amplifier PF-TUNA. In our case the tip is grounded and the voltage is applied on the HOPG substrate. The 2D histograms of Log(|I|) of the I-Vs measured for a force of F = 18 nN are presented in Figure 3. 12. Most of the measurements saturate at $|I| \sim 10^{-8}$ A, nevertheless some branches appear at low bias (|V|<0.4V). This large dispersion depends on the quality of the contact between the tip on substrate and measurement location. Bonnet et al.[172] have performed HOPG substrate measurements for their experiment, at ± 400 mV current above 10 nA on HOPG is recorded. The current obtain in our measurement on HOPG is similar with a value of 15 nA at ± 400 mV.

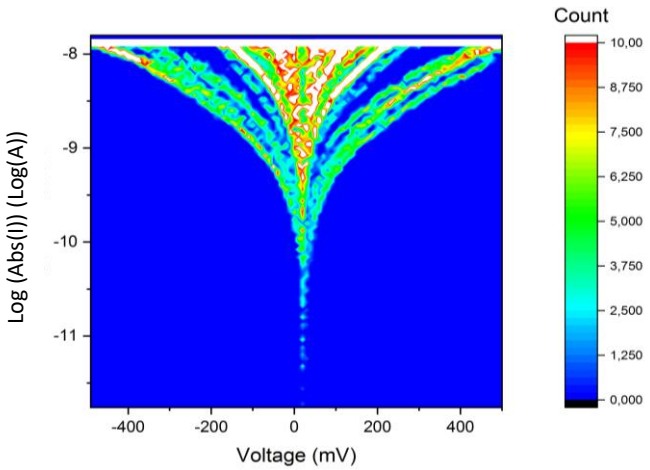

Figure 3. 12 : Typical I-V 2D histograms of bare HOPG substrate used for the deposition of CsCoFe

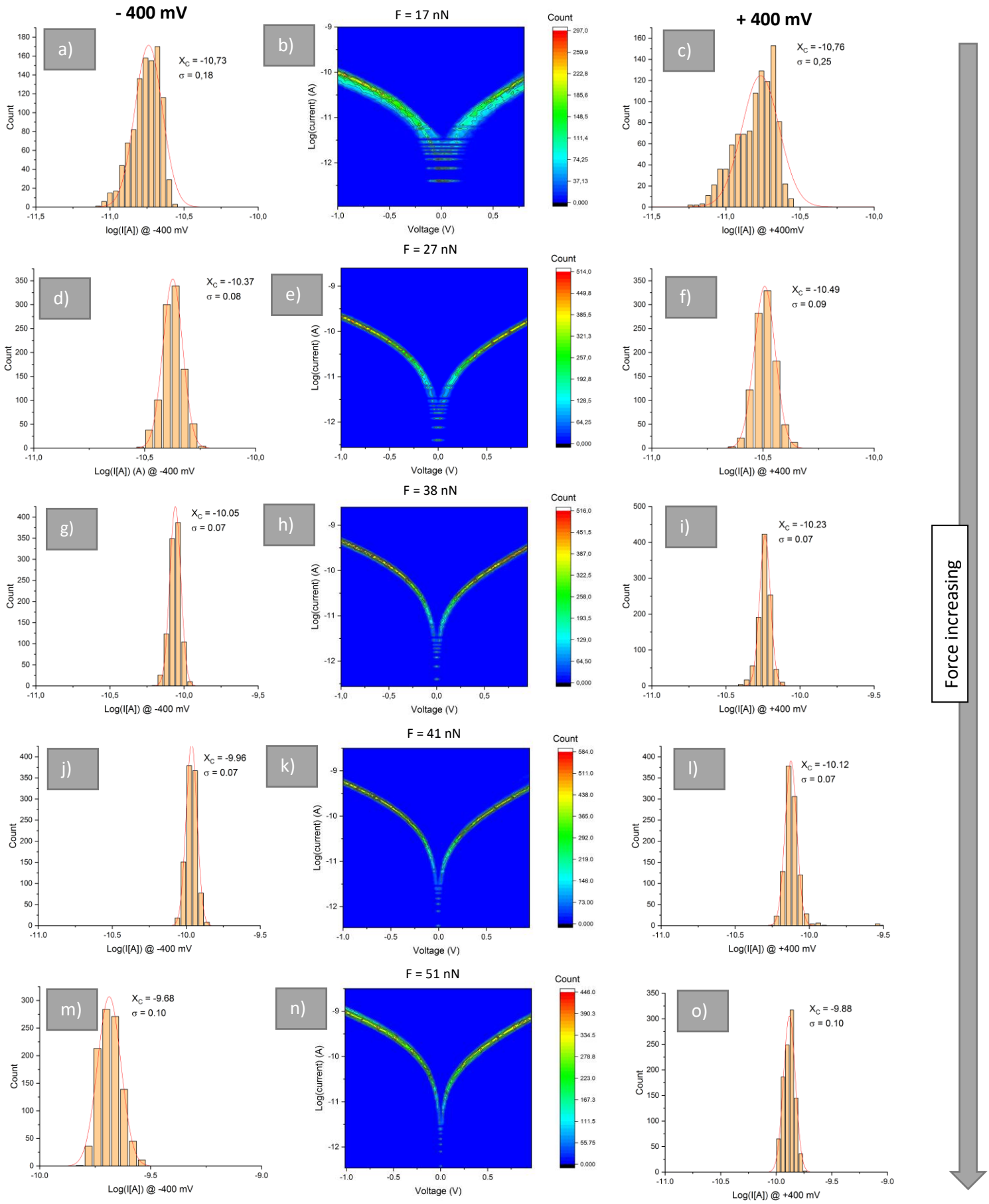

Figure 3. 13 (A, C) Histograms and Gaussian fittings of log(I[A])@-400 mV and log(I[A])@+400 mV,(B) 2D histograms of log(|I|[A]) for PBA NCs of 15 nm height, recorded with a force F= 17 nN. (D, F) Histograms and Gaussian fittings of log(I[A])@-400 mV and log(I[A])@+400 mV, (E) 2D histogram of log(|I|[A]) for a PBA NC of 15 nm height, with F= 27 nN. (G, I) Histograms and Gaussian curve fittings of log(I[A])@-400 mV and log(I[A])@+400 mV,(H) 2D histograms of log(|I|[A]) for a PBA NC of 15 nm height at F= 38 nN. (J, L) Histograms and Gaussian fittings of log(I[A])@-400 mV and log(I[A])@+400 mV,(K) 2D histogram of log(I[A]) for PBA a NC of 15 nm height at F= 41 nN. (M, O) Histogram and Gaussian curve fitting de log(I[A])@-400 mV and log(I[A])@+400 mV,(N) 2D histogram of log(|I|[A]) for a PBA NC of 15 nm height at F= 51 nN.

The conductance properties of a 15 nm PBA nanocrystal as a function of the applied force is investigated to see how electronic transport occurs in CsCoFe PBA system. The method to acquire the I(V) curves has been described in part 3.4.1 except that the process is repeated with increased forces. The result of the experiment is presented in Figure 3. 13. At F = 17 nN (smallest applied force), Figure 3. 13 (B)), the samples show log(|I|[A]) distributions on -10.73 for -400 mV and -10.76 for + 400 mV. When the force is increased to F = 51 nN the log(I[A]) (see Figure 3. 13 n)) dispersion is centered on -9.68 for -400 mV and -9.88 for +400 mV.

Figure 3. 14 shows the plot of Log(Abs(I[A])) together with the of Log(Surface (nm²)) as a function of the force applied by the AFM tip on the PBA CsCoFe nanocrystal. The surface accounts for the contact area between the tip and NC with a Hertz model[173] by using PBA Young modulus E = 24 GPa [174], PBA Poisson coefficient P = 0, tip Young modulus E_{tip} = 200 GPa, tip Poisson coefficient P_{tip} = 0.3 and tip radius of curvature r = 25 nm . Figure 3. 14 emphasizes the fact that, while the contact surface increases by a factor of 2 between the tip and the nanocrystal, the current increases by a factor of 7.2.

We therefore used the experimental data shown in Figure 3. 13. to fit on each average I(V) curve to extract from the double Schottky barrier model (Eq. 3. 5) the evolution of the Schottky barrier height as a function of the force applied to the 15 nm PBA molecule. The Figure 3. 15 present the barrier height evolution value obtained in this way. The results reveal a Schottky barrier height variation of 0.05 eV between 17 nN and 51 nN. The variations in current can be explained by the change of the Schottky barrier heights at the tip/NC and NC/HOPG contact depending on the applied force.

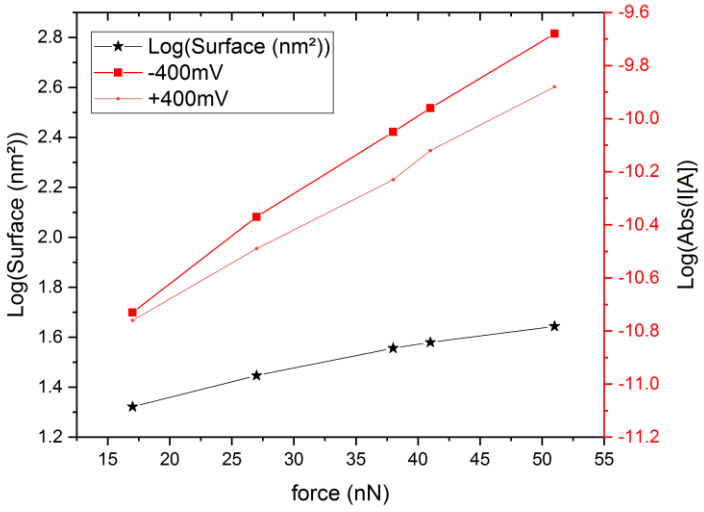

Figure 3. 14 : Calculated surface with Hertz model in Log(S (nm²)) in function of the applied force and force-current curve of the experiment on PBA CsCoFe 15 nm.

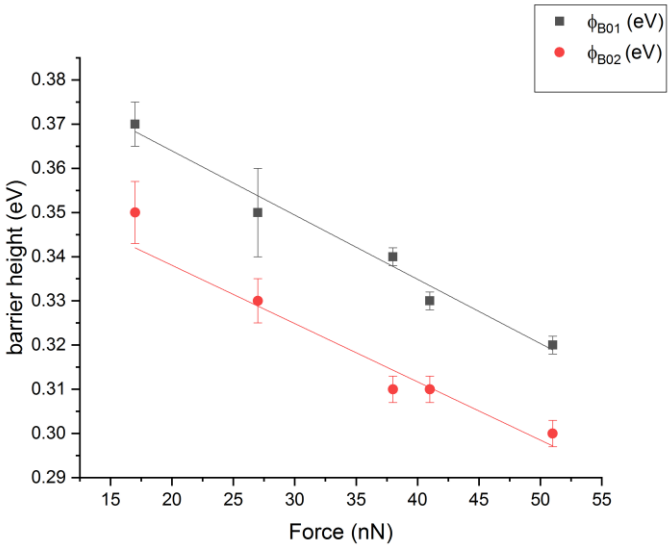

Figure 3. 15 : Barrier Height in function of applied force. Φ_{B01} and Φ_{B01} decrease of few meV when the applied force increase.. The y-scale error bars were obtained by fitting all current-voltage curves independently and running a statistic on all returned barrier height values.

3.5 Electrical characterization as a function of PBA size

3.5.1 Single Energy Level model (SEL)

In this part the C-AFM measurements are perf ormed as a function of the nanocrystal size. The SEL and Double Schottky barrier model will be used to fit the current curves. The Figure 3. 16 (a), c) and e) shows the different 2D histograms of Log(|I[A]|) as a function of the applied voltage for PBAs of size 15, 30 and 50 nm, respectively, with a force F ≈ 15 nN. This value for the applied force is a compromise to maintain a good electrical contact with the PBA nanocrystal, without inducing an important deformation of the NC. The average current-voltage characteristics are obtained from the 2D histograms and are shown in Figure 3. 16 b), d), f), respectively. The Figure 3. 16(b), d), f)) also presents fits to average current-voltage curves made using the SEL molecular model of Eq. (3. 3). For 15 nm PBAs the current distribution (Figure 3. 16 g)) is centered around Log(|I[A]|) = -10.73 (σ = 0.18) @ -400 mV and Log(|I[A]|) = -10.76 (σ = 0.25) @ +400 mV. For 30 nm PBAs the current distribution is centered around Log(|I[A]|) = -9.72 (σ = 0.12) @ -400 mV and Log(|I[A]|) = -9.72 (σ = 0.06) @ +400 mV (Figure 3. 16 h)). For 50 nm PBAs the current distribution is centered around Log(|I[A]|) = -9.31 (σ = 0.26) @-400 mV and Log(|I[A]|) = -9.51 (σ = 0.25) @ +400mV (Figure 3. 16 i)).

A summary showing the Log(|I[A]|) as a function of size is shown in Figure 3. 17. The results are somewhat counter-intuitive because current levels increase with the NC thickness, thus leading to a

negative factor β = -0.1 nm^{-1} in an exponential model $I \propto \exp(-\beta d)$, in which *d* is the NC thickness. The single molecular energy model also does not fit the system perfectly, as seen *e.g.* from discrepancies observed at low bias (V<0.5V) or larger bias in Figure 3. 16 b), d), f). Parameters ε_0, Γ_L, Γ_R (Table 3. 1) are extracted from the SEL model fit do not explain the negative value of the β.

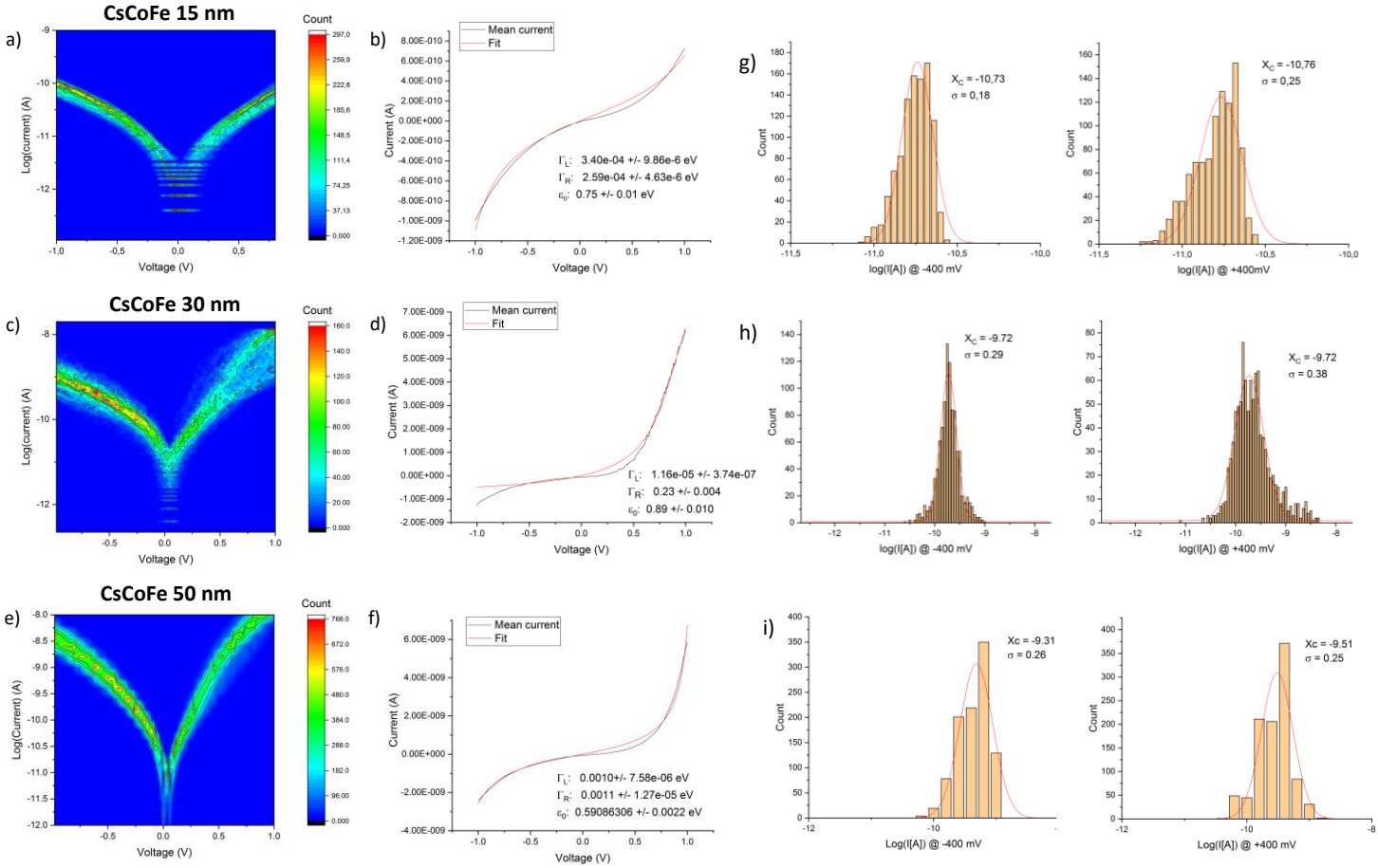

Figure 3. 16 (a), c), e)) 2D histograms of Log(|I[A]|) for 15/30/30 nm PBAs using a force F=15 nN. (b), d), f)) Average current-voltage curves (black lines) and fits (red lines) using a single molecular energy level model (see 3.2.1). (g), h), i))) Histograms and Gaussian fittings of log(I[A])@-400 mV and log(I[A])@+400 mV.

Size	Log(I[A])@-400 mV	Log(I[A])@+400 mV	Γ_L (eV)	Γ_R (eV)	ε_0
15 nm	-10.73	-10.76	3.4E-4	2.59E-4	0.75
30 nm	-9.72	-9.72	-1.16E-4	0.25	0.89
50 nm	-9.31	-9.51	1.0E-3	1.1E-3	0.59

Table 3. 1 : Analysis of I-V curves fitted with the Single Energy Level models

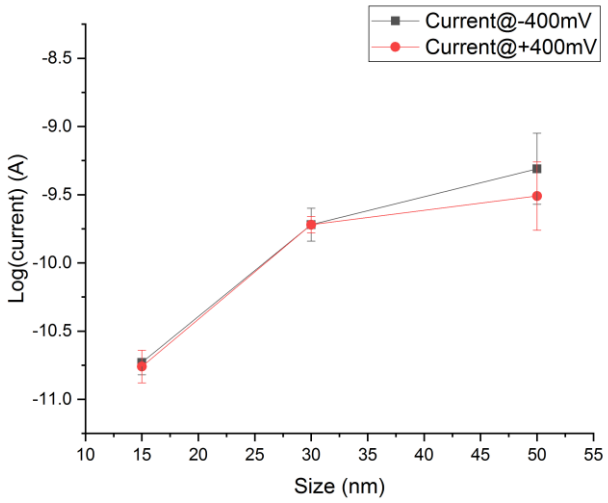

Figure 3. 17 : Log(current)@ ± 400 mV in function of the size of the PBA at F fixed around 15 nN. The y-scale error bars were obtained from the Gaussian fitting of histogram shown in the Figure 3. 16 g), h).

3.5.2 Double Schottky model

In the previous section, we used the single electron level (SEL) molecular model to analyze experimental data from nanocrystals of 15, 30, 50 nm. However, the SEL model does not allow finding an explanation for the evolution of the current with respect to the NC size. The NC size of 15, 30 and 50 nm is on the other hand at the frontier between molecules and the bulk materials. The I(V) characteristics can therefore be interpreted differently in the framework of a metal-semiconductor-metal contact, in which each of the metal-semiconductor contacts can be treated as a Schottky barrier.

The Figure 3. 19 shows the average I-V of PBA 15, 30 and 50 nm fitted with the double Schottky barrier model of Eq. (3. 5). For the surface area S_1 we take the surface area of the nanocrystal i.e. 15 x 15 nm², 30 x 30 nm² and 50 x 50 nm². S_2 is obtained through the use of Hertz model[173] with PBA Young modulus E = 24 GPa [174], PBA Poisson coefficient P = 0, tip Young modulus E_{tip} = 200 GPa, tip Poisson coefficient P_{tip} = 0.3 and tip radius of curvature r = 25 nm which provides a contact area of ≈ 12 nm² for a tip force of ≈15 nN. Fits fall in good agreement with experimental data. The Figure 3. 18 shows the evolution of the fitted Schottky barrier height as a function of the PBA NC size.

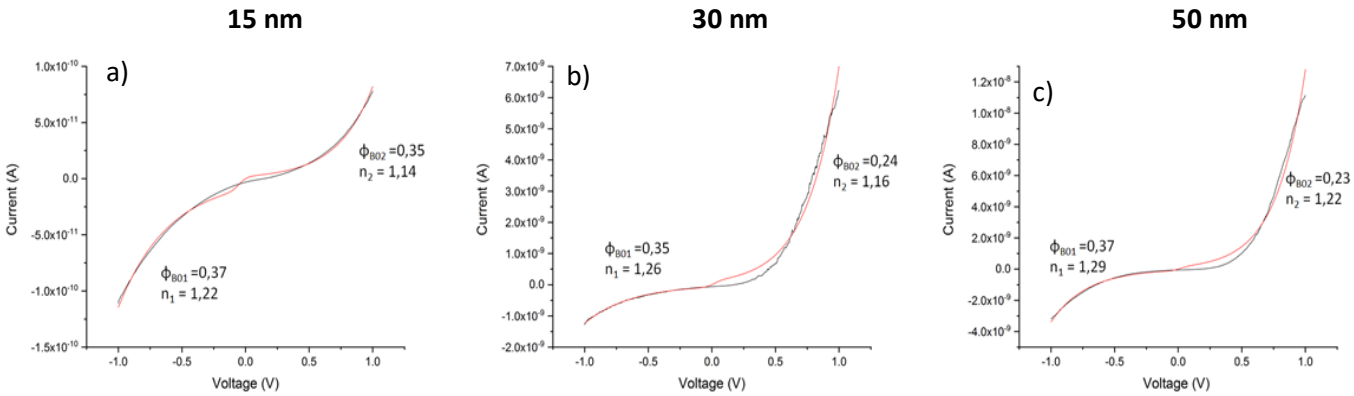

Figure 3. 19 : a-c) I-V characteristics of PBA NCs of 15, 30 and 50 nm respectively, using a force F= 15 nN. The black line corresponds to average of the current-voltage curves and the red line is the fit using the double Schottky barrier model of Eq (3. 5). We also report on graph the value of ideality factor and barrier height provided by the fit.

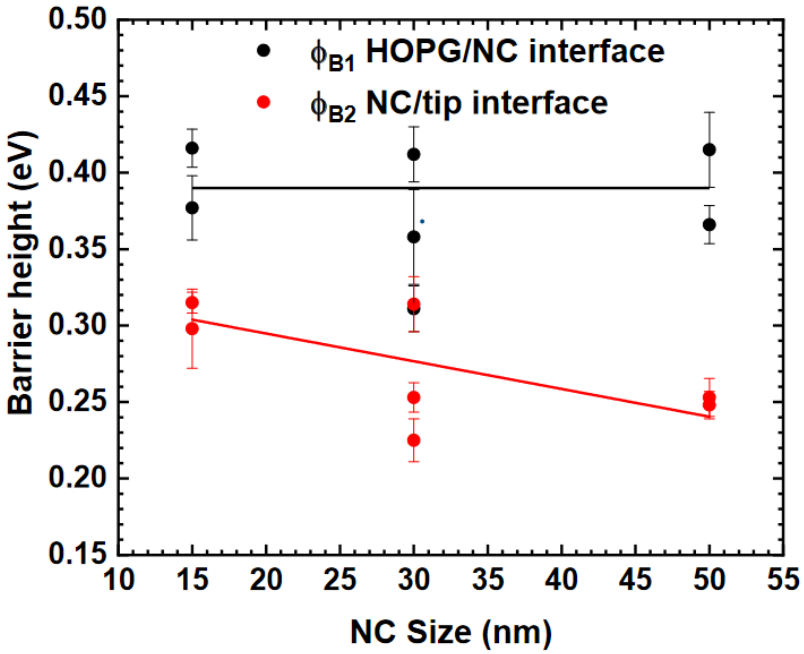

Figure 3. 18 : Barrier Height in function of the size of the nanocrystal. Φ_{B01} does not vary with the size of nanocrystal while Φ_{B02} decrease in function when the size of the nanocrystal increase. The y-scale error bars were obtained by fitting all current-voltage curves independently and running a statistic on all returned barrier height values.

The Table 3. 2 summarizes the barrier height values obtained by fitting the experimental values to the Double Schottky barrier model. Within the fit experimental error bars, the barrier ϕ_{B01} (corresponding to Schottky barrier at the NC/substrate interface as defined in the Eq. (3. 5) and because the bias is applied on the substrate in our experiment) does not depend on the PBA NC size, while ϕ_{B02} (corresponding to Schottky barrier at the tip/NC interface as defined in the Eq. (3. 5) and because the tip is grounded in our experiment) decreases when the PBA NC size increases. This change in Schottky

barrier account for the current level increase with larger PBA NC sizes and the negative β factor of ~-0.1 nm^{-1} reported in the previous section.

Size	ϕ_{B01}	Err ϕ_{B01}	ϕ_{B02}	Err ϕ_{B02}
15 nm	0.37	0.005	0.35	0.007
	0.35	0.050	0.31	0.026
30 nm	0.35	0.014	0.24	0.038
	0.35	0.014	0.25	0.038
	0.41	0.012	0.32	0.009
50 nm	0.37	0.025	0.23	0.033

Table 3. 2 : Fitted Schottky barrier heights on PBA NCs as a function the PBA NC size.

3.5.3 Energies of the molecular orbitals of the molecular junction

In the previous section, the Double Schottky barrier model was used and we obtained barrier height values for the tip-molecule and molecule-substrate junctions. The obtained barrier heights allowed us to find an explanation for the non-dependence of the current on the nanocrystal size. It remains to be seen if this model can be used to determine the molecular orbital energy.

The fact that the current increases as a function of the size of the PBA for a given voltage indicates that the voltage drop across the nanocrystal is likely weak. Classic elastic tunneling current depend exponentially of the distance between electrodes and due to the large size of the PBAs this type of transport is unlikely. The charge transport is therefore attributed to coherent resonant transport via the molecular orbital of the NC (see Figure 3. 20).

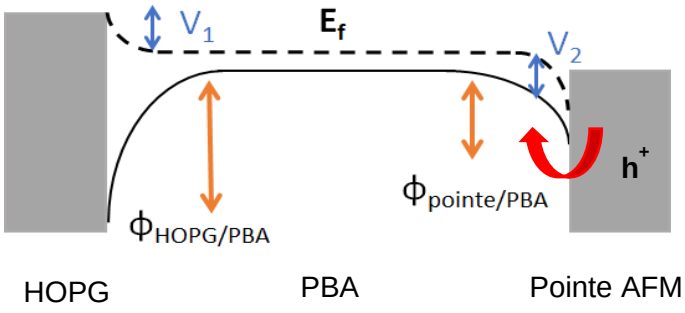

Figure 3. 20 : Energy diagram of Double barrier Schottky model when the tip is negatively biased with respect to the substrate.

For PBA, first-principles relativistic many-electron calculations[175] have revealed that the LUMO is located at about 1.6-1.9 eV from the Fermi energy, corresponding to the e_g orbital for Co^{III}, while the HOMO is very close to the Fermi energy at about 0.2-0.3 eV (Figure 3. 21) and it is ascribed to the t_{2g} orbital of the Fe^{II}. With this information, the molecular orbital responsible of the electron transport in the HOPG/PBA/Tip is the Fe^{II}- t_{2g} d band (HOMO), the LUMO being far away. Figure 3. 21 shows comparisons with calculated energy levels of the PBA nanocrystal in gas phase[175] and the energy level obtained from the double Schottky model. The barrier heights (Φ_{B01} and Φ_{B02}) at the two interfaces corresponds to the position of the PBA HOMO relative to the Fermi energy of the HOPG and PtIr tip respectively. For the shake of comparison, we compare with the average barrier height values (Φ_{B01} + Φ_{B02})/2. Note that the energy level found with the Double Schottky model for the PBA is close to the value found theoretically for the gas phase. In addition, the gas phase does not consider any charge transfer and interaction between the nanocrystal and the electrode that likely occur in a solid-state and can result in a shift of energy level with respect of the Fermi energy of the electrodes.

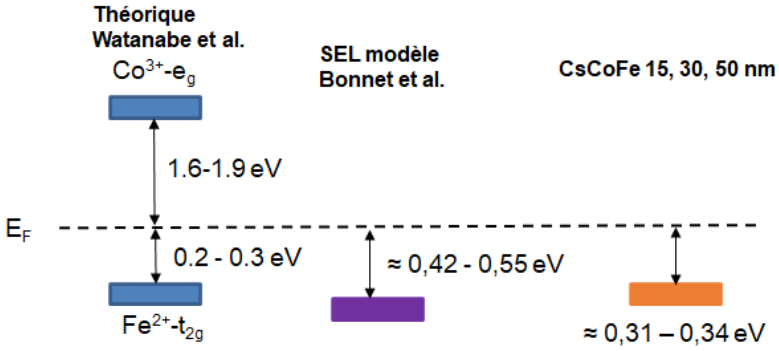

Figure 3. 21 : Energy diagrams for CsCoFe PBAs from transport experiments and ab initio calculations in function of the size. Calculated value come from[175].

3.6 Conclusion

In conclusion, electron transport measurements have been achieved through nanoscale devices consisting of one Prussian blue analogue CsCoFe nanocrystals of size 15/30/50 nm connected between a HOPG electrode and a metal-coated tip of a conducting-AFM. Results show a non-decay of the current with increased NC size. This behavior is not understood in the framework of a single molecular energy level model, and attributed to the large size of the NCs. Another approach considering the tip-PBA-substrate system as a metal-semiconductor-metal double Schottky barrier junction was taken. The electronic transport is understood as coherent tunneling through the molecular highest occupied molecular orbital (localized filled Fe^{II}-t_{2g} HOMO orbitals), in agreement with gas-phase calculations of CsCoFe electronic structure, together with Schottky barriers at the tip/NC and NC/substrate interfaces. We would thus obtain the remarkable result that: (i) as a function of the NC size, only the tip-NC junction is impacted; (ii) as a function of applied force, both junctions (tip-NC and NC-substrate) are impacted.

Chapter 4: BDPA individual molecules and self-assemblies on Au(111) studied by STM, nc-AFM and KPFM

Applications of nanotechnology are vast and include the possibility to address many challenges of physical, chemical, environmental and biological analysis[176]. In this chapter, we report on molecular systems forming one-dimensional self-assemblies (molecular chains). Such one-dimensional chains have shown a behavior of mechanical oscillators at low temperature[177]. They thus consist of an ultimate design of mechanical or electromechanical resonators such as at the macroscopic or microscopic scales, flexural plates, quartz crystals, microbalances and surface acoustic wave devices[178] used for applications in SPM[9] or the accurate detection of tiny masses and forces[179–183]. Mechanical resonators at the nanometer scale have hence enabled new insights in fundamental quantum physics[184–186]. The molecular chains investigated in this work consist in α,γ-bisdiphenylene-β-phenylallyl (BDPA) molecules[177,187]. Usually used to build light emitting diodes[188,189], such free π-radicals have only one electron in the highest molecular orbital. Neutral radicals are generally unstable molecules and the number of stable radicals is small[190] because of the necessity to stabilize the unpaired electron state against reaction with surrounding environment. In this chapter of this thesis, we studied BDPA chains with different lengths on Au (111) using STM, nc-AFM and KPFM performed under ultrahigh vacuum conditions at 4 K and 32 K temperatures using a Joule-Thomson STM/AFM (SPECS, Berlin) with a base pressure of 10^{-10} mbar (see part 2.5.2 for more details). One-dimensional chain oscillations are observed at 32 K as in [177,187,191], however with a behavior which depends on the STM tip bias, which rules out an explanation based on the chain oscillation via substrate phonons[177] solely. The charge state of the molecular chain is analyzed by KPFM, and shown to be neutral with respect to the Au (111) surface at negative tip bias, but undergoes a charging effect for voltages close to the theoretical single unoccupied molecular energy (SUMO) level[187].

4.1 α,γ-bisdiphenylene-β-phenylallyl (BDPA) molecule radical state of the art

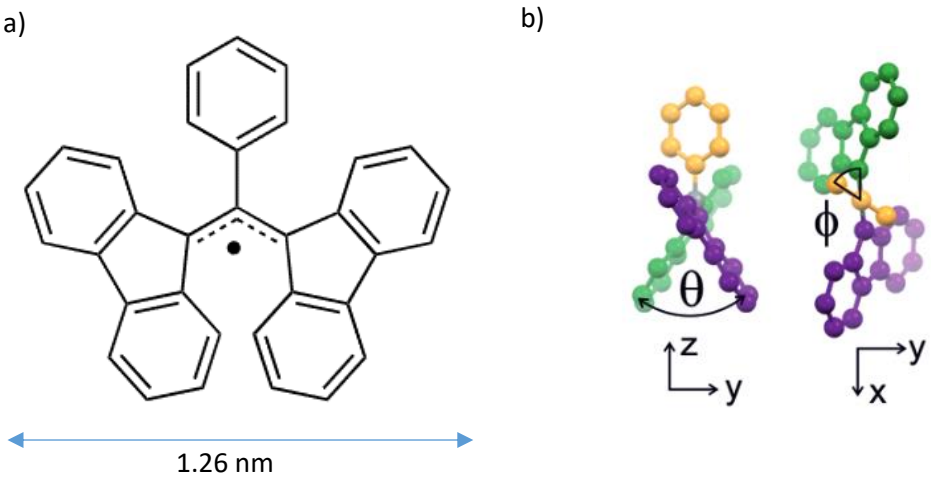

Figure 4. 1 : a) Structure of the BDPA molecule b) Side-view of the BDPA, θ and ϕ denote dihedral and torsion angles. Adapted from[187].

The BDPA molecule is a well-known stable spin ½ complex. Its electrons are delocalized. BDPA have been used as a reference molecule in electron paramagnetic resonance (EPR) experiments[192]. This carbon-centered molecule has attracted great attention in the field of organic electronic materials[193]. It has been first synthesized by Koelsch in 1932[194,195]. The carbon-centered radical presents narrow SOMO-LUMO or HOMO-SOMO energy gaps. Radicals absorb and emit long-wavelength light even when they are not part of π-conjugated systems. Each of the two fluorenyl units is almost planar, but tilted by a dihedral angle θ with respect to the other. In the crystalline bulk phase[196], the dihedral angle was found to be θ = 60° (and θ = 64° in the gas phase). In BDPA, the phenyl unit is twisted by a torsion angle ϕ = 51°. The BDPA molecule is a nonpolar radical[197].

The BDPA molecule was studied when deposited on an Au(111) surface by Müllegger et al.[177,187,191]. The observation of the formation of assemblies of BDPA molecules in the form of one-dimensional chains, indicating a unidirectional attraction of neighboring radicals. BDPA do not have functional chemical groups and the non-polarity of the molecule implies that the interaction between the radicals is of stereochemical nature[177,192]. The formation of one-dimensional chains indicates a preference for aligning fluorenyl units of neighboring radicals with their π-planes parallel to each other (Figure 4. 2 b)). BDPA molecules are separated in the one-dimensional chain by a distance of 0.73 nm along the chain as observed by STM[187] in Figure 4. 2 b). A model of the arrangement of BDPA chains[187] is presented in Figure 4. 2 a). The radical is oriented in a side position with their phenyl groups pointing

toward the central carbon atom of the next-neighbor radical. At low coverage BDPA chains have preferential growth on the fcc regions of the Au(111) substrate (see Figure 4. 2 b)). The shape of a single monomer of BDPA stays unaffected by the chain clustering, which underlines the noncovalent character of the radical-radical interaction.

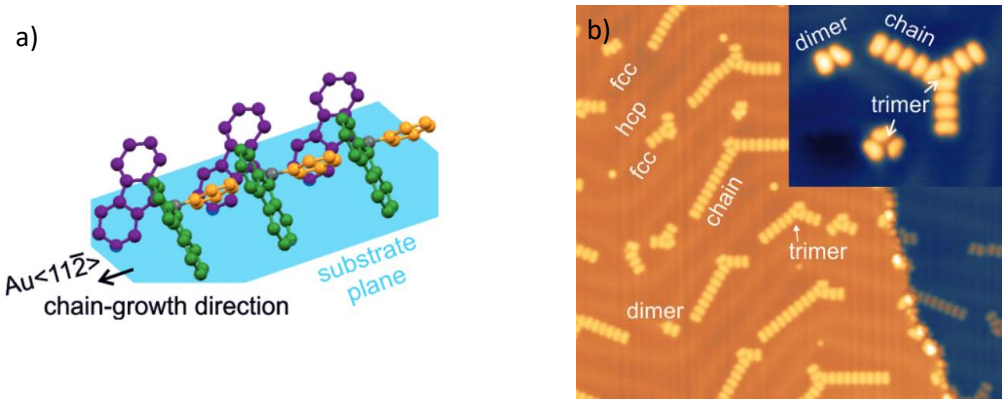

Figure 4. 2 : a) Model structure of a one-dimensional BDPA chain on Au(111). b) 0.2 monolayers of BDPA on Au(111) at 4 K. Extracted from[187].

STM topographic images at 25 K showing enhanced chain oscillations (Figure 4. 3 b)-d)), which puts forward that the mechanical vibrations of the chains are temperature dependent. The thermal bath of the substrate was assigned to be responsible of the motion of BDPA chains. The phonon dispersion of reconstructed Au(111) surface is shown in Figure 4. 4 a). At 4 K, phonons of Au(111) are excited with a wave vector k close to the Γ point of the surface Brillouin zone, the wavelength lambda is therefore $\lambda = 2\pi / k$ and exceeding the length of BDPA chains. Indeed, at $E/k_B = 4$ K maximum wave vector k = 0.05 $Å^{-1}$ in the Γ M direction and corresponds to a phonon wavelength of 13 nm.

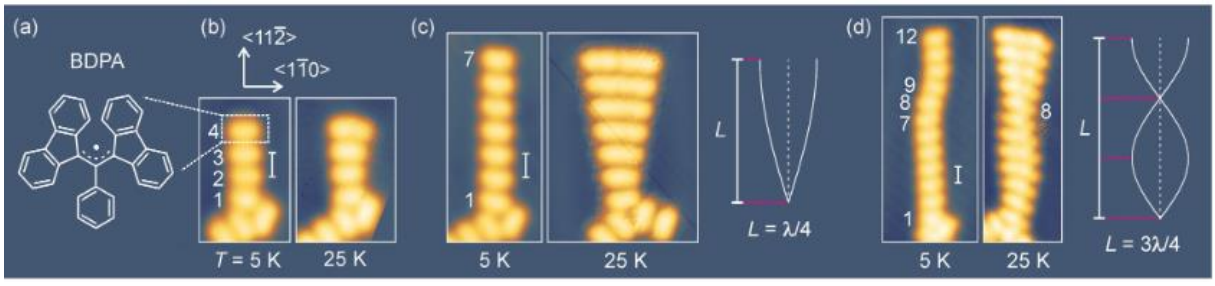

Figure 4. 3 : One-dimensional resonators based on molecular chains of BDPA on Au(111). a) Chemical structure of BDPA. b)-d) STM topographic images (+1 V, 50pA) of BDPA chains obtained at a substrate temperature of 5K (left) and 25 K (right), scale bar = 0.73 nm, individual BDPA monomers are labeled by numbers 1-12. An illustration of first and second vibrational eigenmode of one dimensional harmonic resonator length L and wavelength λ. Extracted from[177].

In order to induce a transverse mechanical vibration, a phonon wavelength is expected to be $\lambda/4 = r$ where r is the monomer separation along the chain (see Figure 4. 4 b)). For a distance r = 0.73 nm, Müllegger et al.[177] concluded that a phonon with wave vector $k = 2\pi/4r = 0.22$ $Å^{-1}$ is needed to excite the mechanical vibration of BDPA chain. According to the Figure 4. 4 a), transverse phonons along Γ M

with similar wave vector have energies of E/k_B = 20 K. Because BDPA chains have a one-dimensional resonator behavior, the frequency of the oscillation was estimated by Müllegger et al. by using the formula for the eigenfrequency of a cantilever[177]. A semi-quantitative result of the resonance frequency of a cantilever is found. Studies, by using a STM equipped with an additional radio frequency (rf) wiring with a bandwidth ranging from 10 MHz to 1 GHz have been used to record the resonance frequency of the BDPA chain of about f_c = 98 MHz with a quality factor of Q = 40 for a 5-BDPA chain. By repeating measurement on 4-BDPA chain and also 7-BDPA chains, authors have measured f_c = 127 ± 26 MHz (4 BDPA chain) and 51 ± 10 MHz (7-BDPA chain)[177].

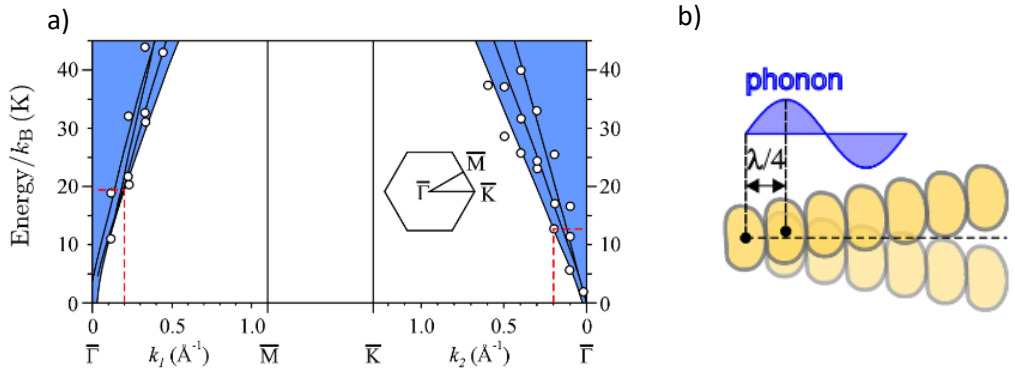

Figure 4. 4 : a) Phonon dispersion of the reconstructed surface Au(111). b) Illustration of a substrate phonon with wavelength λ exciting individual monomers of BDPA chain. Extracted from[177].

Scanning tunneling spectroscopy[191] obtained the dI/dV spectrum of the BDPA molecules on Au(111) substrate with the STM tip placed over the single monomer of a chain on Au(111) (see Figure 4. 5). The spectrum shows the position of the different molecular orbitals of the molecules on the Au(111) substrate. The LUMO peak appears at +1.9 V when the HOMO peak appears at -1 V. A peak at -0.6 V is attributed to the SOMO level. The Figure 4. 5 b) presents a summary of all molecular orbitals with the addition of the SUMO at +0.6 V[187]. No prominent SOMO/SUMO resonances are observed in the spectra of the Figure 4. 5.

a)

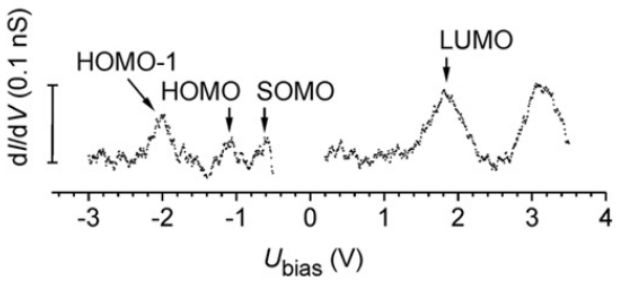

b)

resonance	energy (±0.2 eV)	assignment
1	< −2	HOMO-1
2	−1.1 to −0.75	HOMO
3	≈ −0.6	SOMO
4	≈ +0.6	SUMO
5	+1.9	LUMO
6	+3.1	LUMO+1, +2

Figure 4. 5 : a) Tunneling conductance (dI/dV) spectrum of BDPA/Au(111) after subtraction of the Au background signal. Extracted from[21]. b) Energy of molecular orbital obtained by point spectroscopy at constant z and constant I of BDPA radicals in chains absorbed on Au(111).Extracted from[177,187].

4.2 Self-assembly properties of BDPA on Au(111)

4.2.1 Sample preparation

BDPA molecules purchased from Sigma-Aldrich were thermally evaporated from a quartz crucible at about 370 K inside the UHV preparation chamber of the JT-SPM system after a thorough degassing at 373 K. During the deposition of the molecules, the sample was kept at room temperature. The Au(111) surface was prepared by repeated cycles of 0.8 keV Ar^+ sputtering and annealing at 700 K.

4.2.2 BDPA radical chain

The Figure 4. 6 presents an STM image at 4K with different lengths of BDPA chains on the surface. The STM image taken at a sample voltage +1 V has the same appearance as Mülleger et al.[177] and shows a totally frozen chain oscillation. The apparent height of BDPA at ± 1 V varies between 0.10 – 0.14 nm, which is significantly smaller than the nominal width of a BDPA radical (see Figure 4. 1), thus an upright standing orientation is unlikely. The STM image validates the value of r = 0.73 nm between the BDPA monomers in the chain.

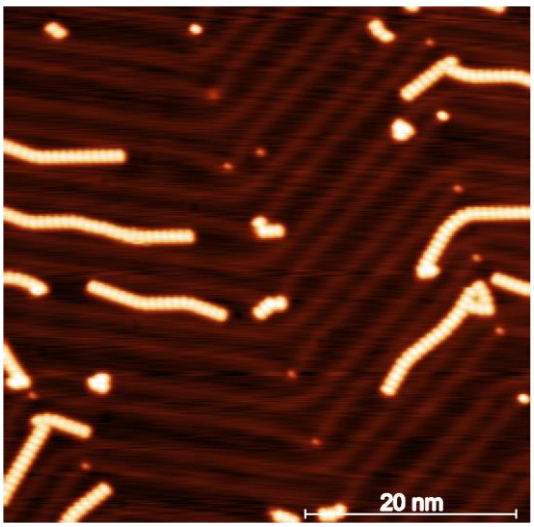

Figure 4. 6 : STM topographic image of BDPA on Au(111) at 4 K (1 V/10 pA) and showing different structural clusters.

nc-AFM measurements at 4K have been performed on one of the one-dimensional BDPA chains. A high resolution is obtained without intentional tip functionalization (apart from tip preparation/shaping into the Au substrate). The constant height Δf image of BDPA chain and BDPA trimer is shown in Figure 4. 7 b). The white contrast is due to the repulsive force interaction with the tip, while black contrast corresponds to the attractive van der Waals force contribution. The two fluorenyl units at the edge of the molecules are observed thanks to the white contrast. The phenyl group of the molecule can be

distinguished by a black dot on the AFM image (Figure 4. 7 b) and c)). The phenyl group is stepped a bit down in comparison with the fluorenyl group and corresponds to a lower Δf signal. So, we can conclude that the convex side of the bean-shape on the STM current image (see Figure 4. 7a)) gives information about the fluorenyl group and the dark contrast on the Δf nc-AFM images (see Figure 4. 7b)) of the BDPA monomer coincides with the position of the phenyl. With this information, it is possible to give the orientation of BDPA molecule inside the structure. The Figure 4. 7 c) shows the BDPA placement for the trimer structure image with AFM. It was common to be able to move the monomer at the end of the chains during nc-AFM scanning which underlines the weak coupling of the molecules with the substrate.

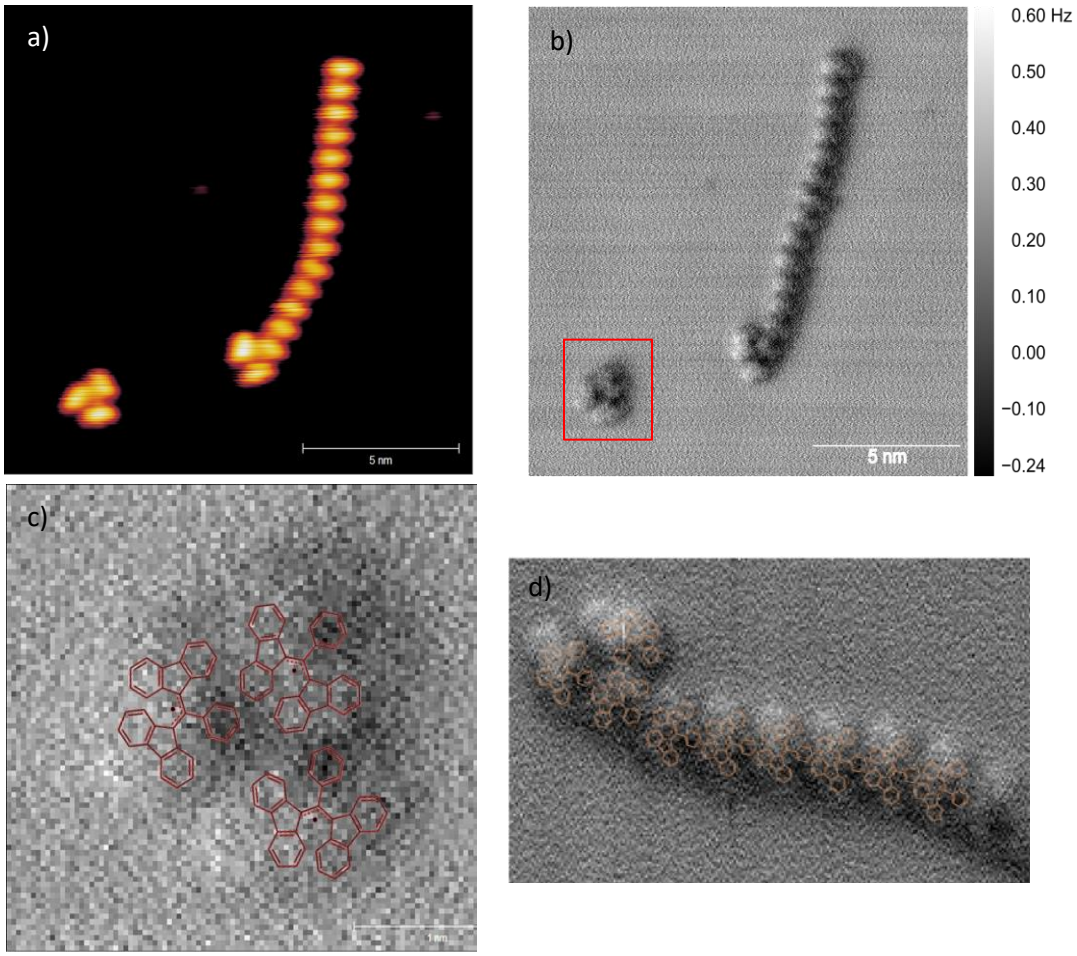

Figure 4. 7 : a) STM image of BDPA molecules at 4 K (1 V/10 pA) b) Δf image of BDPA molecules (A_{osc} = 100 pm, V_{bias} = 0 V). in nc-AFM. The red rectangle is the area zoomed made in c). c)-d) Trimer and chain structure of BDPA respectively. The high-resolution permits to overlay BDPA molecule in red and in orange color, and to determine the molecule orientations (see text).

4.2.3 Vibration mechanism of BDPA chains as from literature

When the temperature is risen up to 32 K, the chain looks broadened perpendicularly to the axis of the chain (see Figure 4. 8 a) b)). The broadening indicates transverse mechanical vibrations of individual monomers in the chain relative to the Au(111) substrate. For some chains, the magnitude of the transverse broadening is maximum at their free end. When the chain is pinned at the two extremities, the maximal transverse broadening is located at the middle of the chains. This observation at 4 K and 32 K is in agreement with literature[177].

The blurring of the chain indicates that the chain vibrations occur on a time scale much faster than the scan speed of the STM tip (1 sec per scanned line) and the bandwidth of the STM feedback loop (few kHz). The first and second vibrational eigenmodes of one-dimensional BDPA chain on the Figure 4. 8 b) with L = λ/4 (Figure 4. 8 b) left chain) and L = 3λ/4 are shown. Most of the time the resonator is in the first vibration mode and sometimes the resonator adopts the second vibration mode, which also corresponds to the observations of Müllegger et al.[177,187,191].

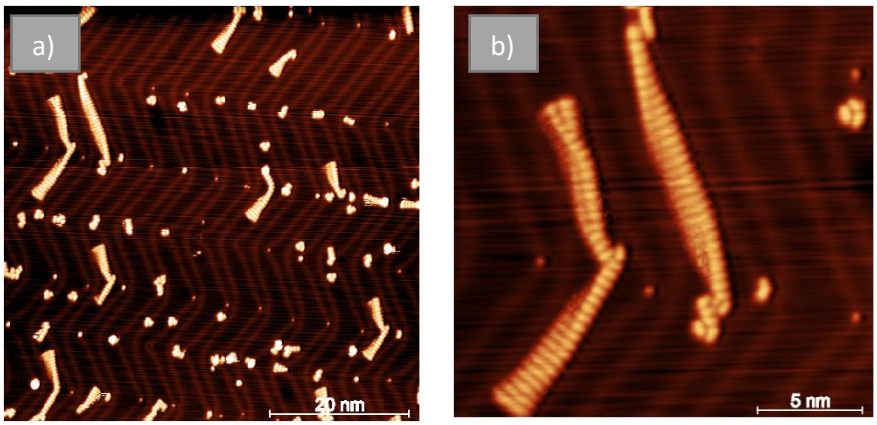

Figure 4. 8 : a) STM topographic image of BDPA on Au(111) at 32 K (1 V/10 pA). The observed broadening results from the transverse mechanical vibrations of BDPA molecules. b) Zoom on a BDPA chain at 32 K where different modes of vibrations are observed (1 V/10 pA).

STM topographic images at 32 K (Figure 4. 9 a), b)) show in more detail the transversal mechanical vibration induces by the thermal bath of the substrate via phonon-molecule coupling. The node and anti-node pattern suggest that each individual monomer of the chain oscillates in a concerted manner with intramolecular coupling. One or more additional nodes are observed and shown in Figure 4. 9. The additional node is located between the free end and the fixed beginning and is located at the 2/3 of the total chain length denote the one-dimensional harmonic resonator (Figure 4. 9 a)).

The envelope of vibratory motion allows us to extract the wavelengths associated with the length of the chain. The length L and wavelength λ are given in Figure 4. 9 a)-b). An energy of E/k_B = 20 K is

necessary to start the vibration of the chain, and our experiments are in agreement with this value. At 4 K the movement is totally frozen (see Figure 4. 6), and at 32 K transverse vibrations are present.

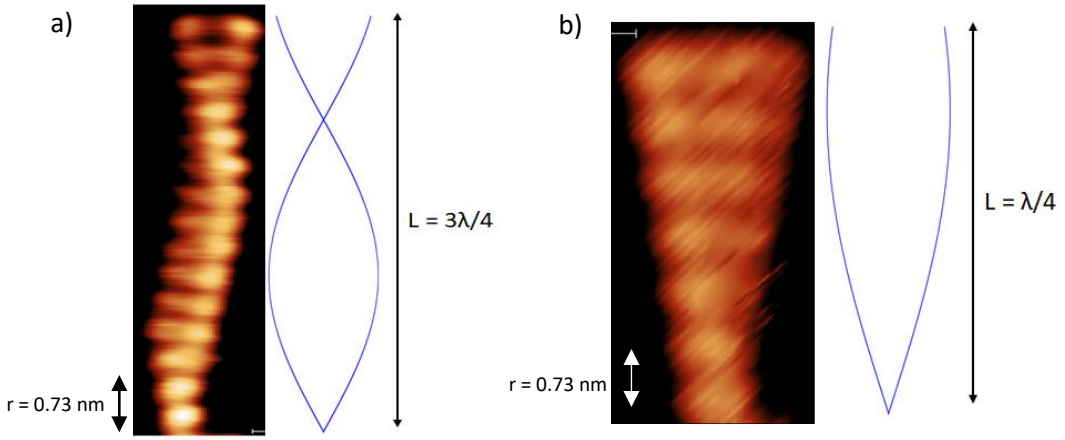

Figure 4. 9 : a)-b) STM topographic image (1V / 10 pA) of BDPA chain at 32 K. Illustration of first and second vibrational eigenmode of a one-dimensional harmonic resonator of length L and wavelength λ.

4.2.4 Effect of the Bias polarization on mechanical vibration of BDPA chain

STM topographic images were done with different polarizations at 32 K (+1 V and -1 V) to test the impact of the STM bias onto the mechanical vibration of the BDPA molecule. Firstly, a STM image at condition of +1 V/10 pA is obtained on a BDPA chain. At this condition, mechanical transversal vibrations are observed (see part 4.2.3). On the same BDPA chain, consecutive STM images are performed with the opposite polarization e.g STM condition of -1 V/10 pA. A different behavior is observed. The mechanical transversal vibrations are absent or at least strongly reduced (Figure 4. 10 b) and d)) at -1V. This phenomenon has not been described in the literature.

To try to understand why such an effect happened, the density of states of the BDPA needs to be analyzed (see Figure 4. 5). The presence of the HOMO at -1 V means that the STM image at -1 V is done via a part of the current through the HOMO orbital. At this bias the Fermi level of the electrode is aligned with the HOMO: the conductivity increases, and the tip-substrate distance consequently increases. This shows that an increased STM tip interaction with the molecule (which would disrupt the mechanical vibration) does not hold to explain experimental data. The charge state of the molecule in addition to the coupling with phonons may have a role for the vibration of the molecule on Au(111). Following this observation, a more detailed study of the charge state of the molecule will be carried in the part 4.3 using KPFM spectroscopy grid.

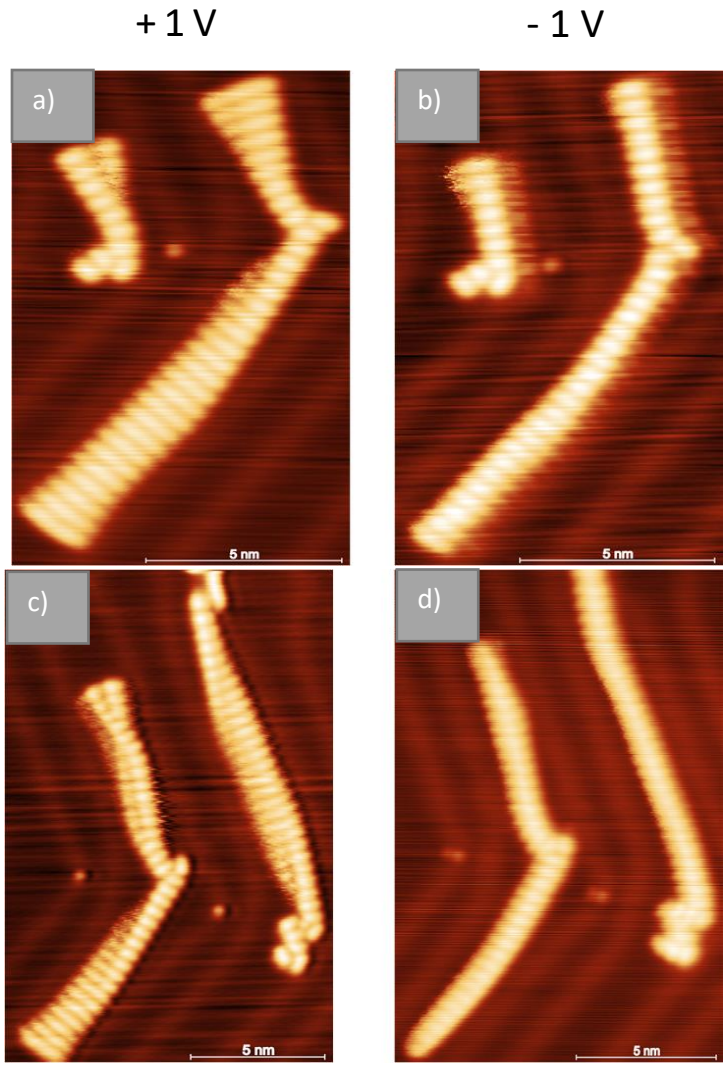

Figure 4. 10 : a) and c), STM image (+1 V/10 pA) of BDPA at 32 K. Transversal mechanical vibration due to the coupling with the phonon can be seen thanks to the broadened aspect. b) and d), STM image (-1 V/10 pA) of same BDPA chain of a) and d) respectivly. The broadened aspect which denotes of the vibration of the chain is not present anymore.

4.3 KPFM grid measurements

4.3.1 Single point Δf(V) spectroscopy and grid procedure

Spectroscopy measurements were done in constant height mode with the z-feedback loop off, as in nc-AFM measurements. The KPFM spectroscopy consists in recording the AFM resonator frequency shift Δf(V) as a function of the sample bias (see part 2.7).

In order to acquire distribution of surface potential, van der Waals and capacitive force contributions, a spectroscopy grid is performed along the chain. The grid was set over an AFM image of the BDPA chain. In every point of the grid, several spectroscopy measurements Δf(V) were acquired. To verify the reproducibility of the experiment and to increase the signal to noise ratio of Δf measurements,

multiple spectroscopies are done on a single point. All the average curves were analyzed thanks to a homemade software created especially to this application. It allows processing simply and quickly the large number of curves that is generated by this kind of experiment. The software development was done in Python and the graphical interface was created with the PyQt module.

Due to the potentially long acquisition time (up to 10h), small lateral and horizontal drifts at low temperature occurred. In order to estimate this drift, nc-AFM or STM images need to be performed before and after grid spectroscopy.

The tip-sample system is considered as a parallel plate capacitor that leads to a frequency shift signal proportional to the second derivative of the tip-sample capacitance. Δf(V) exhibits a parabolic behavior with the sample bias as described in part 2.7 with the Eq. 2. 32. The model can be simply described by a canonic parabolic form $\Delta f = A + B * (V_{bias} - V_s)^2$. This equation is used to fit the experimental data and gives us access to van der Waals force, capacitance, and surface potential. The Figure 4. 11 shows experimental data of single point Δf(V) spectroscopy on Au(111) fitted with the canonic parabolic equation.

- surface potential V_s: this value corresponds to the bias at the maximum of the Δf(V) spectroscopy. It contains information about the tip and sample work function difference. A local electrostatic contribution is also contained in V_s as defined in Eq. 2. 32. Since V is applied to the sample, a positive (negative) surface charge will be compensated by a negative (positive) surface potential contribution.
- "capacitance" B: this pre-factor represents the concavity of the parabola and is expressed in Hz/V^2. It is proportional to the tip-substrate capacitance second derivative d^2C/dz^2, and will be (improperly) called capacitance coefficient in the following.
- parameter A (independent of the tip bias): it corresponds to a map of $\Delta f(V_s)$. It contains van der Waals force contributions (attractive force gradients corresponding to negative frequency shifts or dark features in images) but includes as well short-range repulsive force contributions (repulsive force gradients corresponding to positive frequency shifts or bright features in images), and electrostatic image effects at $V_{bias} = V_s$, if any. This parameter is also sensitive to any long-term drift of the probe eigenfrequency f_0 during the image acquisition (for example, a temperature drift or a tip-surface distance drift).

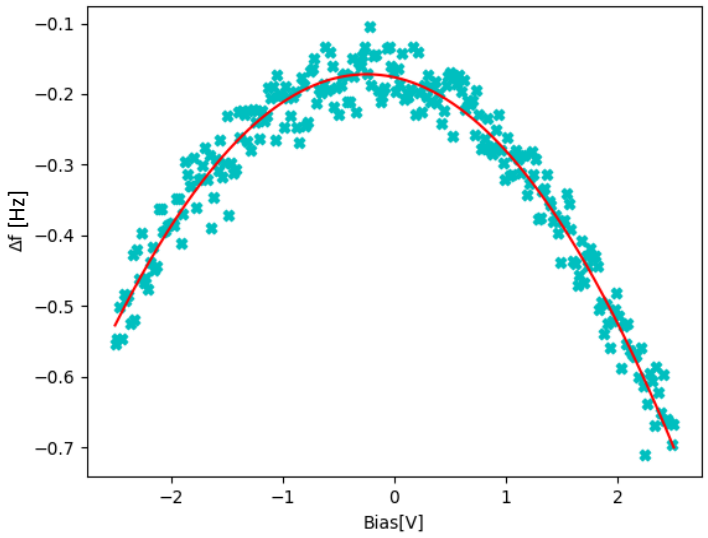

Figure 4. 11 : Example of a Δf(V) spectroscopy curve recorded above the Au(111) substrate. Experimental points (blue crosses) show a parabolic dependence (fitted curve in red) from which the parameters V_s, A and B can be extracted (see text).

4.3.2 Grid spectroscopy

Figure 4. 12 shows the maps of the surface potential, Root Mean Square (RMS), capacitance and van der Waals signals obtained from a BDPA chain on Au(111). In a first step, a nc-AFM image was acquired. A grid of 3 nm x 4.1 nm (25 x 32 points) (see Figure 4. 12 b)) is superimposed on the constant height AFM image and centered on the BDPA chain. Bias sweeps are made from -0.8 V to +1.8 V on the molecule and on the Au(111) substrate to check if the tunneling current is not too high, since a high current can damage the molecule or the tip during the spectroscopy bias sweep. The oscillation amplitude of the tip is fixed at 100 pm (200 pm peak to peak). The acquisition time for a typical grid was ≈ 7 h, with here a lateral drift of ≈ 200 pm during the KPFM scan acquisition. In the middle of all maps, a sudden change appears (white arrow in Figure 4. 12 d)). This change is certainly due to a modification of the tip state during a bias sweep, which likely alters the tip-sample distance. For this reason, only the bottom of the images (represented by red rectangle in Figure 4. 12 d)-f)) will be exploited in the following. The Root Mean Square (RMS) shown in Figure 4. 12 c) corresponds to the error on the fit of the curve. It provides a quantification of non-parabolic effects (in any) which may

occur at certain points of the Δf(V) spectroscopy grid[129].The Figure 4. 13 shows a zoom on the interesting part of the grid spectroscopy experiment presented in Figure 4. 12.

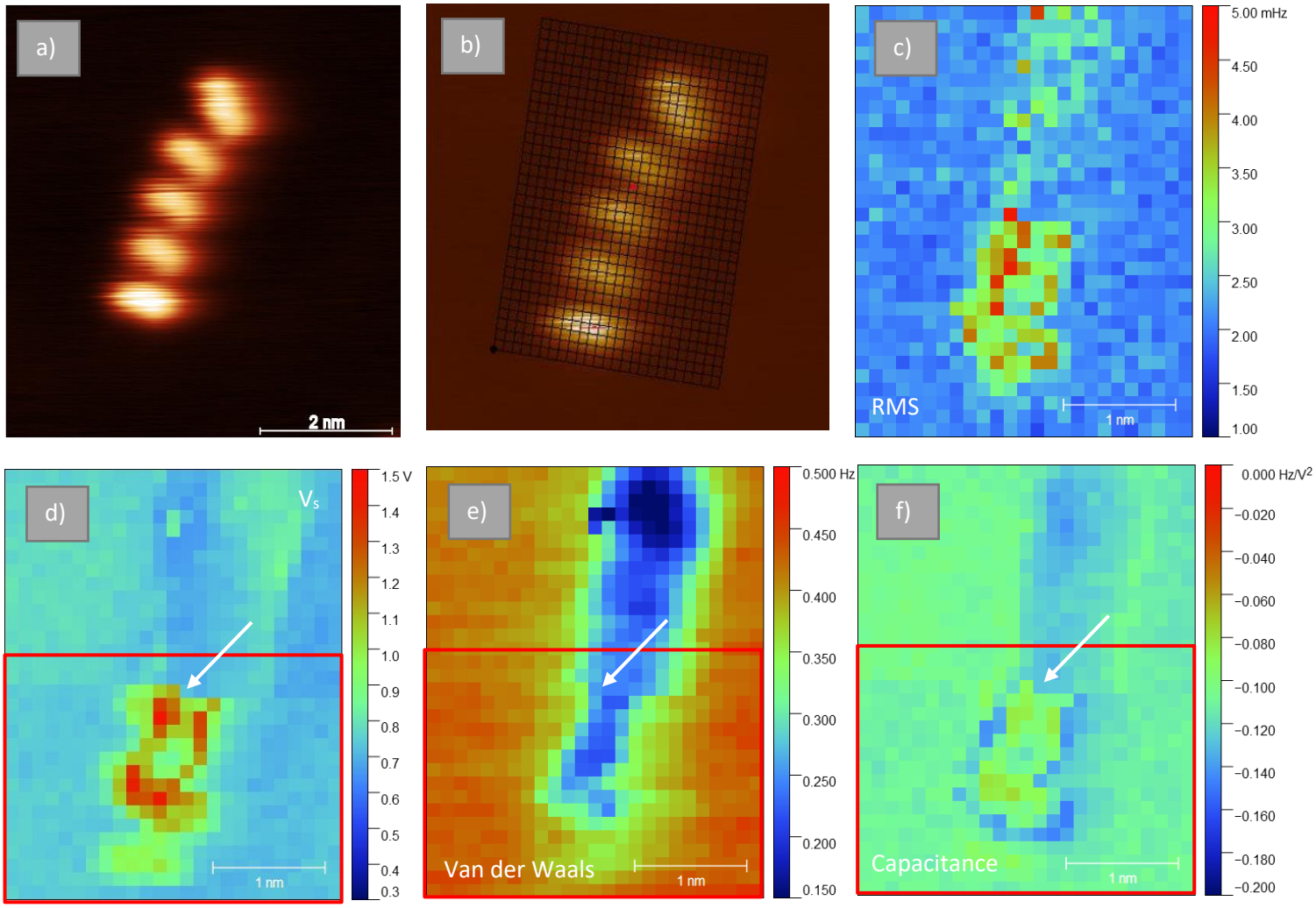

Figure 4. 12 : Grid spectroscopy measurement on a BDPA chain using a bias range [-0.8 V; +1.8 V] a) STM image at V_{bias} = 0 V before the grid Δf(V) spectroscopy. b) grid placement before the grid experiment. Signal maps extracted from the Δf(V) spectroscopy of c) fit error (root mean square or RMS) d) Surface potential, e) van der Waals signal, f) capacitance signal. The grid spectroscopy was done with A_{osc} = 100 pm. The red rectangle represents the area used before (but including) the tip state change, which is marked by a white arrow.

The surface potential map (Figure 4. 13 a)), shows important variations of ≈ 0.8 V between the substrate and the BDPA molecule indicate the negative charge behavior of the molecule. The error on the surface potential is about 10 mV on the worst case at the middle of the molecule as denote the Figure 4. 13 b). The capacitance map represented by the Figure 4. 13 d) is flat on the Au(111) substrate. A variation (increase) of the capacitance signal is detected over the BDPA molecule, which is consistent with the dielectric presence of the molecule on the surface. The value of the capacitance is also seen to differ provided the tip is positioned at the edge or the center of the molecule, which corresponds to the positions of the fluorenyl and phenyl groups, respectively. In the Δf(V_s) map (Figure 4. 13 c)), the

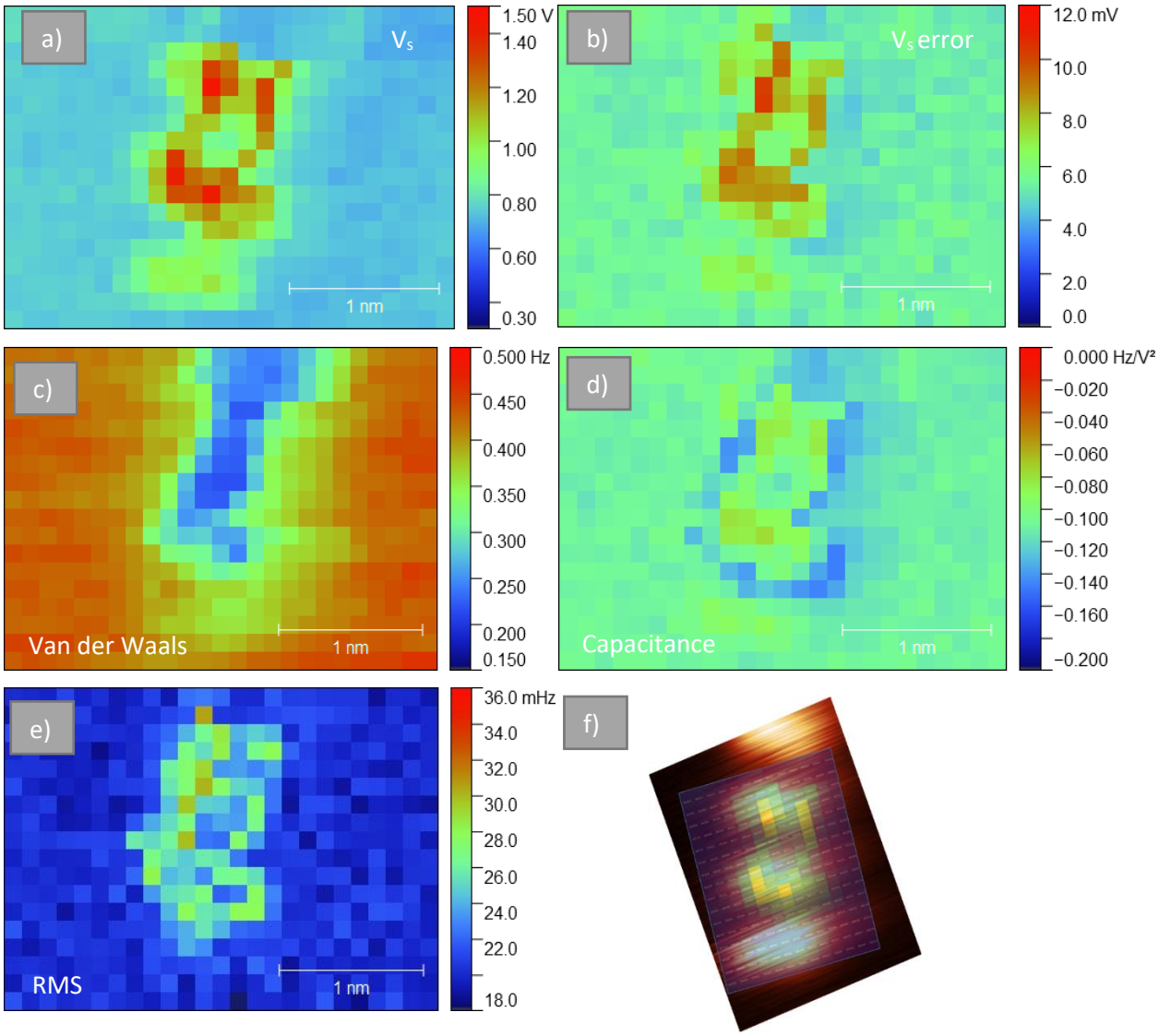

Figure 4. 13 : Zoom of the spectroscopy grid measurement on BDPA molecules using bias range [-0.8 V ; +1.8 V]. Signal maps extracted from Δf(V) spectroscopy of a) surface potential b) error on surface potential c) van der Waals d) capacitance e) fit error (RMS) f) Superposition of the STM image and the surface potential map extracted from the grid spectroscopy.

signal is clearly different on the molecule or on the substrate and highlights an attractive signal at the junction of two BDPA molecules that denotes the radical-radical interaction between BDPA. It can be noted that the first molecule at the bottom of the image is visible by STM and nc-AFM, however the signal obtained by spectroscopy is weak compared to the other molecules. The RMS value increases (Figure 4. 13 e)) on the molecules (with an average value up to 26 mHz), which denotes a change on the Δf(V) parabolicity. The investigation of frequency shift and current curves at a given grid point is necessary to understand why the RMS value changes. The Figure 4. 14 a) and b) shows examples of Δf(V) spectroscopy curves together with the associated current curves acquired on the BDPA molecule (Figure 4. 14 c) and d)). A Δf(V) spectroscopy on the Au(111) substrate is also presented in the Figure 4. 14 e) in comparison. The Figure 4. 14 a) and b) shows an increase of the frequency shift signal taken

on two different points on the BDPA molecule. A modification of the shape of the parabola is noticed for the positive bias ≈ +0.6 V. This change in the frequency shift signal happened repetitively on different points of the grid during a spectroscopy on the molecule and accounts for the augmentation of the fit RMS value. A possible explanation for the non-parabolic behavior of the Δf(V) curve is an electron transfer from the tip to the molecule[129,198,199]. Such charging appears on the Δf(V) spectroscopy by a shift of the parabolic function[129,200,201], which should, in principle, be also associated to a modification of the tunneling rate, and hence corresponds to a feature in the I(V) spectroscopy.

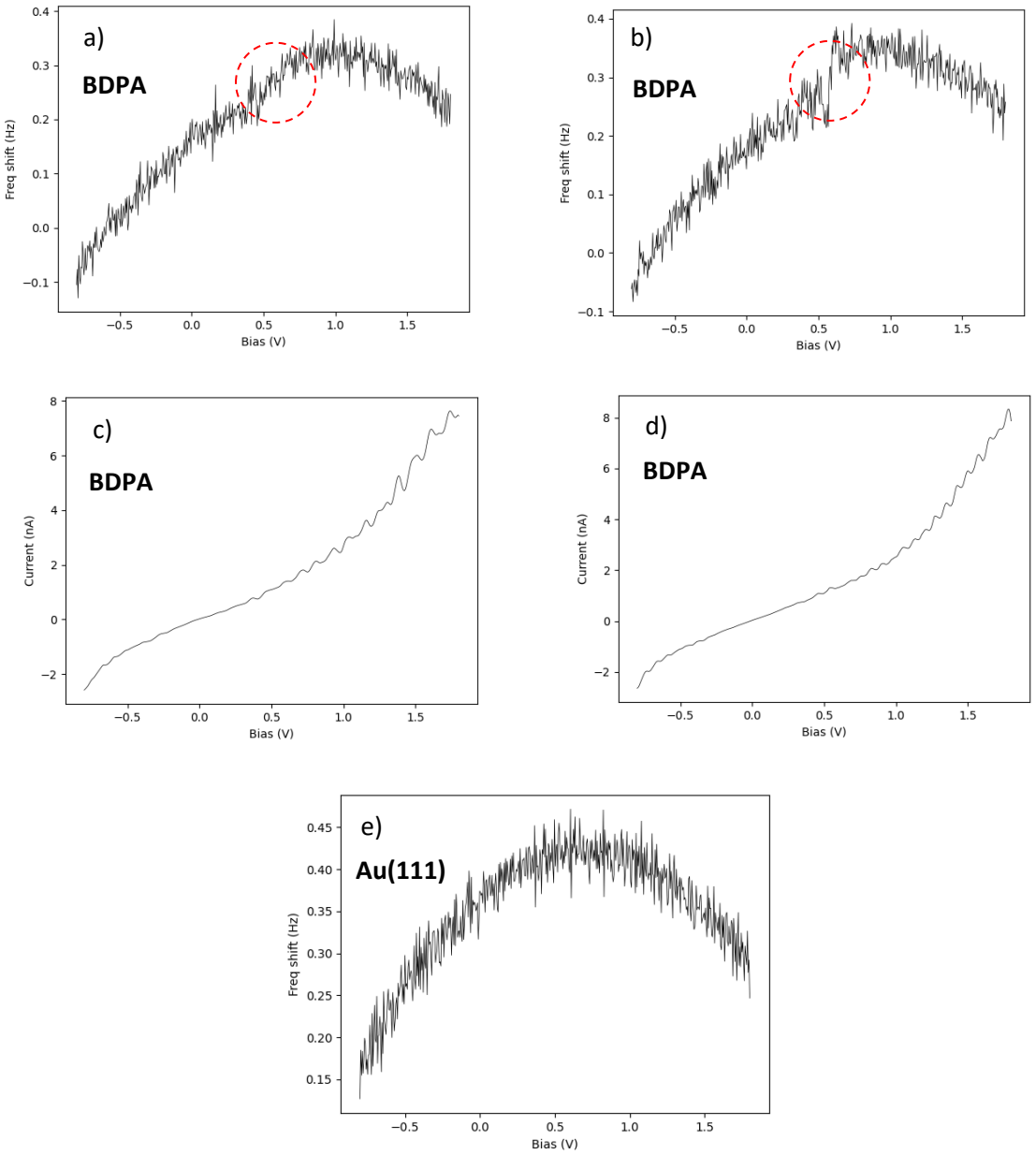

Figure 4. 14 : a),b) Δf(V) spectroscopy on BDPA with corresponding c),d) I(V) curves. The tunneling current at 0.6 V does not match with the parabola increase frequency shift. The change in the shape of parabola is indicated with red circle in a) and b). e) Δf(V) spectroscopy on Au(111).

Here, the increase of the frequency shift signal does, however, not match with an increase in the tunneling current. This is consistent with the hypothesis of the SUMO charging, since the SUMO is not clearly seen in experimental dI/dV spectroscopic data[187,191].

4.3.4 Fitting range on BDPA KPFM grid spectroscopy

We have shown in Section 4.3.3 the presence of non-parabolic $\Delta f(V)$ spectroscopies in the grid spectroscopy of BDPA molecules. If the non-parabolicity has been evidenced via changes in the RMS fit map, the deliberate fit of non-parabolic curves with a parabolic model (as done in Figure 4. 12 and Figure 4. 13) also introduces by principle artefacts in $\Delta f(V_s)$, B and V_s images, since all three coefficients are used to account, at best, the non-parabolicity of the $\Delta f(V)$ curve. In particular, the Vs images of Figures 4.12 and 4.13 have to be interpreted with care. In view of obtaining images free of artefacts, one simple method is to perform the fit on a reduced bias range either smaller or larger as compared to the transition bias at ≈+0.6V. The fitting range is thus reduced to [-0.8 V; 0 V] range. The corresponding maps for V_s, $\Delta f(V_s)$ and B coefficients are presented in the Figure 4. 15, together with maps of the fit RMS and of the corresponding fit RMS value for V_s.

In Figure 4. 15 d) the fit RMS still shows a feature associated with the molecule, but it is blurred and less intense, though the fit RMS color scalar is identical as in Figure 4. 13. This indicates that non-parabolicity effects are relaxed in the fit using a [-0.8 V; 0 V] range. The surface potential map (Figure 4. 15 a)) also now appears as uniform, although showing a larger noise, which we ascribe to the fact that only less than one half of a parabola is taking into account of the fit, thus increasing the uncertainty on Vs (the RMS fit error on V_s shown in Figure 4. 15 b) is a good indication of this, as compared to Figure 4. 14 b). In particular, the presence of scattered red dots in Figure 4. 15 a) showing large surface potentials is caused by the reduced bias range for the fit. The capacitance map (Figure 4. 15 e)) showing larger noise and the molecule is only slightly distinguishable. The capacitance map is roughly uniform and in suitability with the fact the tip-sample height is constant during the spectroscopy grid.

We now analyze the $\Delta f(V)$ spectroscopic data in the [0.6 V, 1.8 V] range. We fix the capacitance value to the value extracted from the fit in Figure 4.15. Maps of the fitted coefficients V_s, $\Delta f(Vs)$ as well as fit error signals are presented in the Figure 4. 16.

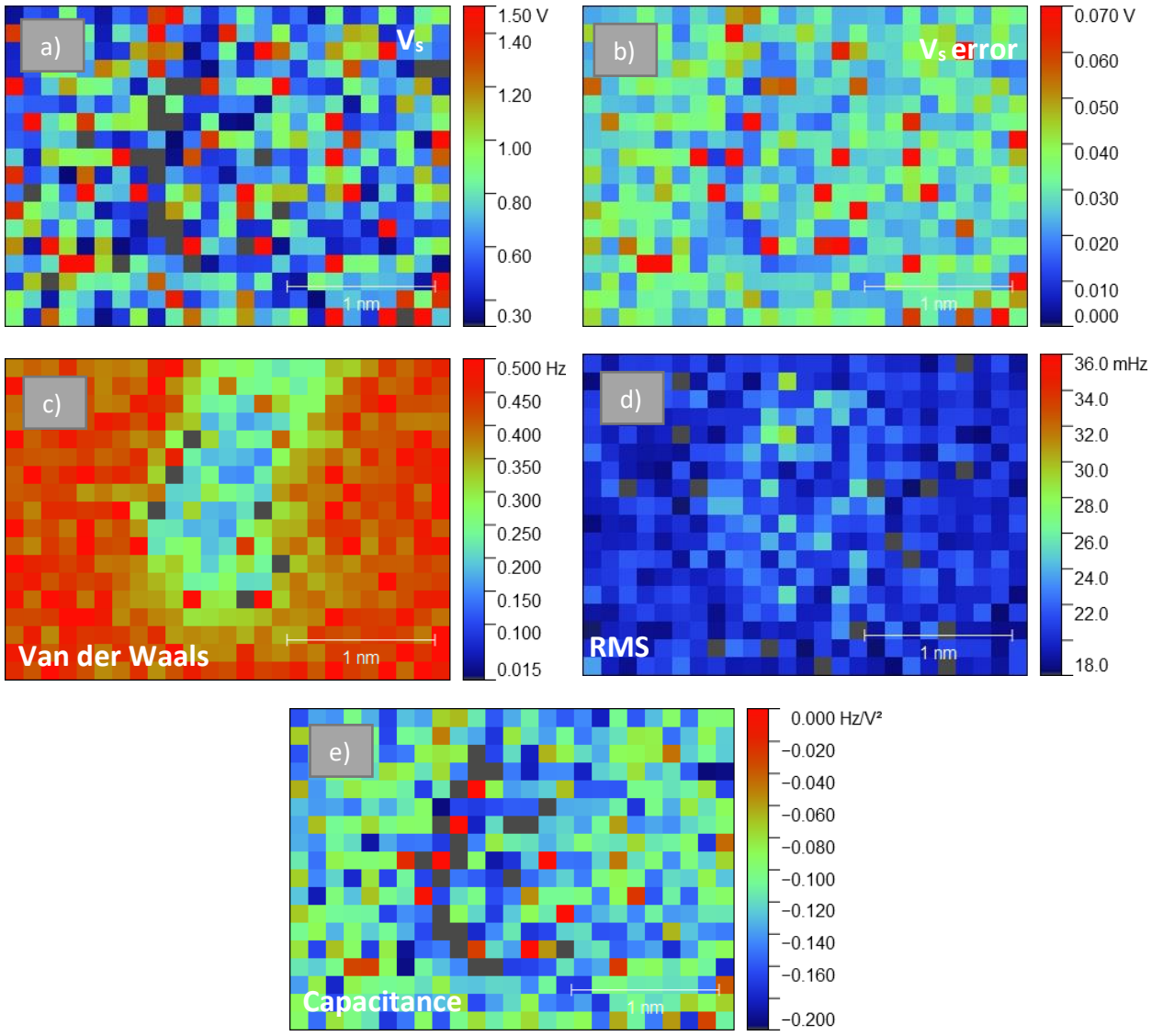

Figure 4. 15 : Zoom of the spectroscopy grid measurement on BDPA molecules using bias range [-0.8 V , 0 V]. Signal maps extracted from Δf(V) spectroscopy of a) surface potential b) incertitude on surface potential c) van der Waals d) fit error (RMS) e) capacitance.

In the Figure 4. 16 a) the surface potential value on the substrate ≈0.8 V is equivalent to the value in the Figure 4. 15 a) for the negative range. A Surface potential of ≈ 1.30 ± 0.015 V is found on the BDPA molecule of the chain and therefore the substrate-molecule potential difference is about ≈0.6 V. The BDPA molecule is charged negatively (ΔV_s positive) and assume that the SUMO molecular orbital is filled (see Figure 4. 5 b)). This emphasizes that the molecule charges when the polarization of the bias is positive. The van der Waals interaction (Figure 4. 16 c)) looks similar as the negative part spectroscopy. The Figure 4. 16 d) is noisier than the RMS map presented in Figure 4. 15 e).

The spectroscopy analysis in negative and then positive part of the polarization, informs us that the property of the molecule is charged for a positive polarization. This property can be related to the part 4.2.4 and the hypothesis that the polarization-dependent charge state of the molecule has a role to play in the chain oscillation of BDPA.

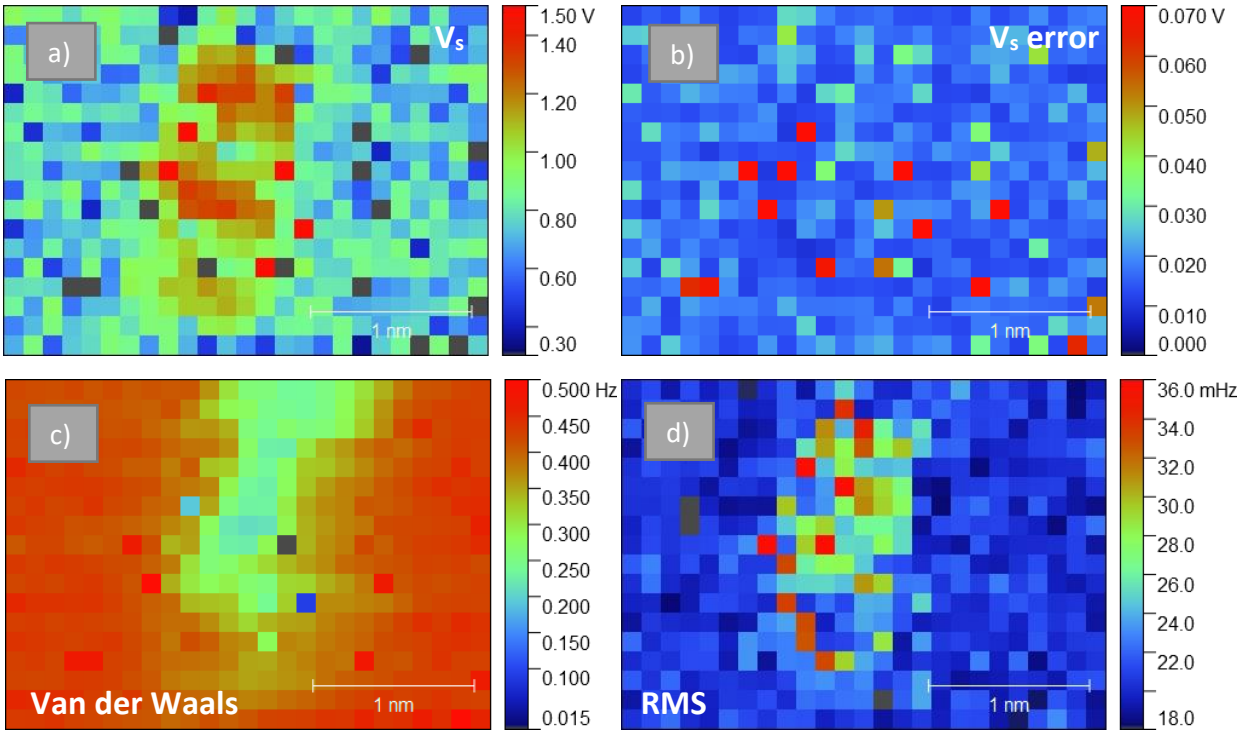

Figure 4. 16 : Zoom of the spectroscopy grid measurement on BDPA molecules using bias range [0 V, 1.8 V]. Signal maps extracted from Δf(V) spectroscopy using the B value of the [-0.8 V, 0 V] range of a) surface potential b) incertitude on surface potential c) van der Waals d) fit error (RMS).

4.4 Conclusions

In conclusion, the BDPA chain assembly has been observed by STM and nc-AFM. The bean shape of the BDPA molecule on the STM image and the high resolution obtained by nc-AFM allowed to determine the position of BDPA molecules when they are organized in a chain. The vibrational character of the BDPA chain has been observed by STM at 32 K and a dependence of this vibration was observed as a function of the polarization used to image in STM. The investigation by KPFM of BDPA chain reveals that the molecule charge state change in function of the polarization of the substrate. Spectroscopy Δf curve over BDPA molecule reveals a raise of the Δf signal at ≈ +0.6 V, this change is associated to a negative charge transfer into the SUMO, however, without any visible change of the tunnel current. This change of charge state is assumed to be related to the change in the vibrational character of the molecule when imaged in STM with a positive or negative bias.

Chapter 5: Self-Assembly and switching properties of azobenzene derivatives deposited on Au(111) substrate

Engineering self-assembly and functional characteristics of adsorbed molecules is essential to pave the way to nanotechnology applications. Azobenzene derivatives consist of a ring with two phenyl rings connected by double bonded nitrogen atoms. Azobenzene have been widely studied, since they are polar molecules[202–204], may be easily functionalized with "spacer leg" groups[205–207], and exhibit specific optical properties[205,208–212]. As an example, azobenzene molecules can switch reversibly by photoisomerization between two isomers: *trans and cis*, leading to optically active device elements[213,214]. The high yield and stability of the switching reaction enables technological applications for light-driven actuators[215], and information storage[216,217]. Other studies also report the electrical activation of the *trans-cis* isomerization of azobenzenes with scanning tunneling microscopy[218–221].

In this chapter, the intramolecular and self-assembly behavior of 3,3',5,5'-tetra-*tert*-butyl-azobenzene (TBA) on Au(111) is studied with STM and non-contact AFM. The introduction of *tert*-butyl "legs" reduces the coupling of the azobenzene core with the substrate[205,219,222]. The isomerization of the molecules was studied under the application of both an electrical field and of ultraviolet irradiation. The effect of the two different stimuli is compared. Scanning probe microscopy experiments (STM and nc-AFM) have been performed under ultrahigh vacuum conditions at 4 K and 77 K temperatures using a Joule-Thomson STM/AFM (SPECS, Berlin) with a base pressure of 10^{-10} mbar (see part 2.5.2 for more details). AFM characterizations were realized using length-extensional resonators equipped with tungsten (W) tips (Kolibri sensors, SPECS, Berlin) of oscillation frequency $f_0 \approx 1$ MHz and quality factor $Q \approx 10^5$ (see part 2.3.2).

The chapter is organized as follows. First, we present the TBA molecule and its properties. In a second part, the organization of TBA molecules is studied from STM experiments. The third part is devoted to the response of the molecule to the application of an electric field. Finally, we describe the effect of UV irradiation on the TBA molecule.

5.1 Properties of the azobenzene molecule

5.1.1 Azobenzene switch mechanism

The azobenzene molecule is composed of two phenyl rings connected together by two nitrogen atoms ($C_6H_5N=NC_6H_5$). The nitrogen atoms form a double bond oriented at 120 ° with respect to the N-C bond. Azobenzene exhibits a bi-stable isomerization illustrated in Figure 5. 1. The two configurations are either nearly planar (*trans* conformation) or non-planar (three-dimensional *cis* conformation)[205,223–225]. The total energy of the *trans* conformation is 0.6 eV lower than the *cis* one[205,226] in the gas phase, and the two configurations are separated by a barrier of about 1.6 eV (isomerization from *trans* to *cis*)[227]. In solution, the photoinduced isomerization of azobenbenzes has been highly studied[228–231]. To switch from *trans* to *cis* the photon energy needs to have an energy of 3.4 eV corresponding to a wavelength of λ = 365 nm. To switch from *cis* to *trans*, the energy needed is 2.95 eV corresponding to a wavelength of λ = 420nm[221,232,233]. The Figure 5. 2 show a schematic representation of energetic diagram of the azobenzene molecule. Theoretical studies have been made to investigate which energy pathway is taken for the photo isomerization[230,231,234]. The rotation mechanism, which is a twisting around the N-N bond, and an in-plane rotation of the C-N-N is known as inversion path[231]. Azobenzene, thanks to its two stable states, has two conduction states that can be exploited as molecular switches[235–237]. However, its application as a switch for electronic / mechanical molecular devices needs its adsorption

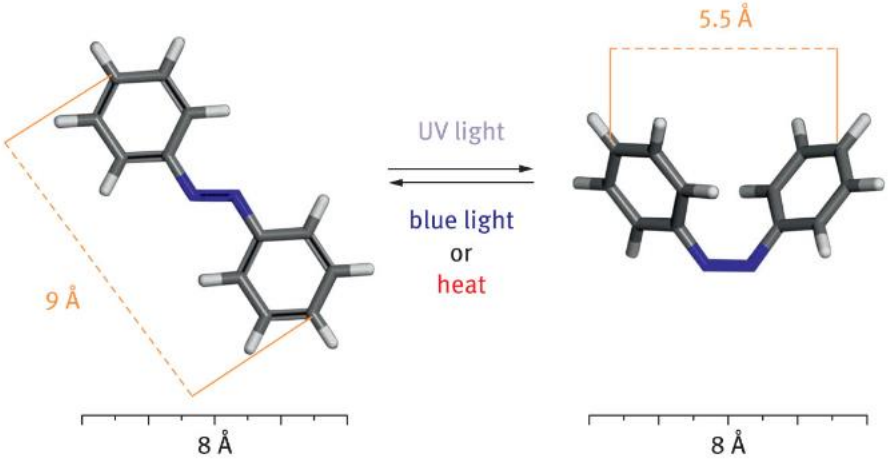

Figure 5. 1 : Trans (left) and cis (right) isomers of azobenzene.

on surfaces. The coupling between the molecule and the metal substrate has an impact on: (i) the energy pathway; (ii) the degrees of freedom in comparison with the gas phase. A molecule adsorbed on the metal has less degrees of freedom and the electronic structure of the two isomers changes with the metal-molecule coupling. Also the absorption spectrum of the molecule can change[238,239]. STM studies of azobenzene on metal surfaces have been reported[219,240,241]. To avoid a high coupling with

the surface, azobenzene derivatives (especially using “spacer legs”) have been developed, in order to improve the performance of the molecular switching on surfaces.

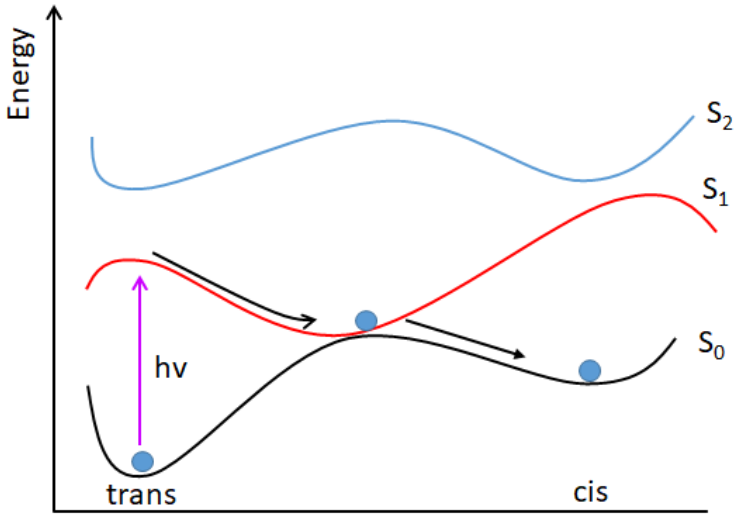

Figure 5. 2 : Schematic diagram of trans -> cis photoisomerizatition of TBA azobenzene molecule. The ground state is noted S_0 , first excited state S_1 and the second excited state S_2. After an irradiation with λ=365 nm an S_0 -> S_1 excitation occur The circle indicate the pathway on potential energy after the photo excitation to switch to the trans -> cis state. Adapted from[234].

5.1.2 TBA molecule

The 3,3’,5,5’’-tetra-tert-butyl-azobenzene (TBA) is an azobenzene molecule with four lateral tert-butyl groups acting as “spacer legs” (Figure 5. 3). TBA was synthesized by D. Guérin from the NCM group at the Institut d’Electronique de Microélectronique et de Nanotechnologie (IEMN) following the procedure described by Alemani et al[219]. The main purposes for this molecule is (i) the increase of the separation between surface and the azobenzene π-system of 0.69 Å[205]; (ii) a lower electronic coupling between molecule and surface; (iii) an increased surface mobility.

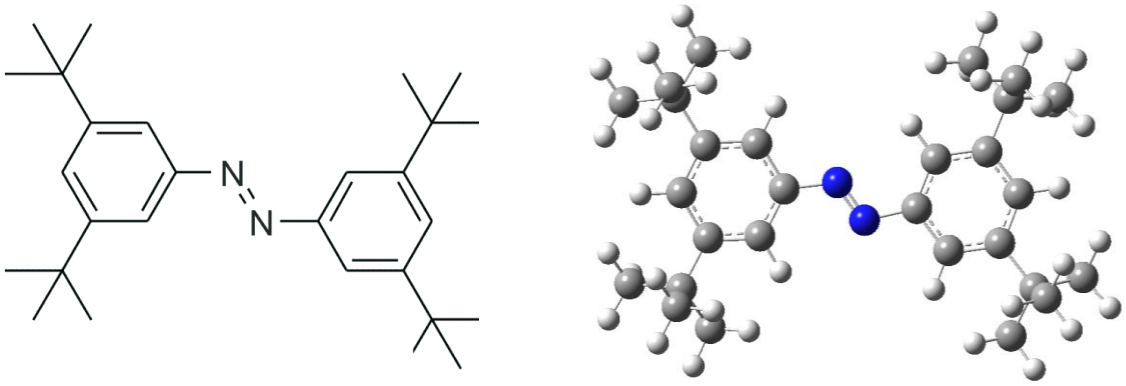

Figure 5. 3 : 3,3’,5,5’-tetra-tert-butyl-azobenzene (TBA) : chemical structure (left) and sphere model (right). The molecule is composed of an azobenzene part with 4 “spacer legs” (the Tert-butyl-groups).

It was reported that the absorption spectroscopy of the TBA in solution exhibits photochemical and thermal isomerization behaviors typical for azobenzene derivatives[219]. Photo-isomerization from *trans* to *cis* and from *cis* to *trans* was reported in cyclohexane using appropriate excitation wavelengths[219] ($\lambda_{trans->cis}$ = 325 mn, $\lambda_{cis->trans}$ = 410 nm). An absorbance spectrum in hexane is performed and shown in the Figure 5. 4. The absorbance peak at 325 nm is consistent with the literature[219,221] and defines the wavelength used for isomerization in the part 5.4.

All molecules after the synthesis are in the *trans*-isomer form, which is the energetically favored state (Figure 5. 2). After deposition, the sample is protected from external light as best as possible during its transfer to the JT analysis chamber where it is in complete darkness.

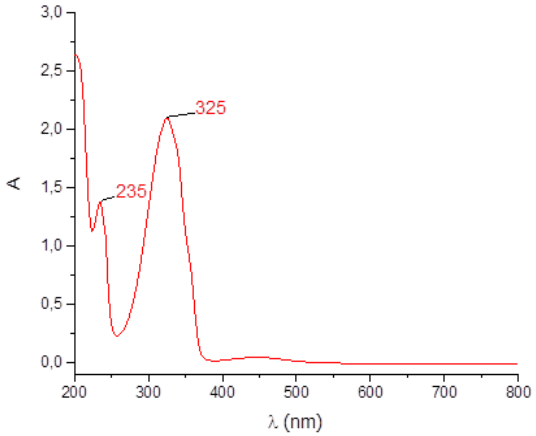

Figure 5. 4 : Absorbance spectra of trans TBA after synthesis in hexane at 25°C. The spectra have the absorbance peak at 325 nm.

5.1.3 Sample preparation

TBA molecules were deposited on Au(111) substrate (from MaTeck, Jülich, Germany) by evaporation from a quartz crucible at about 370 K inside the UHV preparation chamber of the JT-SPM system. During the deposition of the molecules, the sample was kept at room temperature. An STM image measured at 4K of TBA molecules on Au(111) is shown on Figure 5. 5. Before molecule deposition Au(111) was cleaned with the procedure described in part 2.6.3.

5.2 TBA adsorption and organization on Au(111)

The TBA molecule appears on the STM image as four lobes with a height of 2.5 ± 0.1 Å with a parallelogram shape (Figure 5. 5). These measurements are in agreement with the STM measurements already made in the literature[219,221,242].

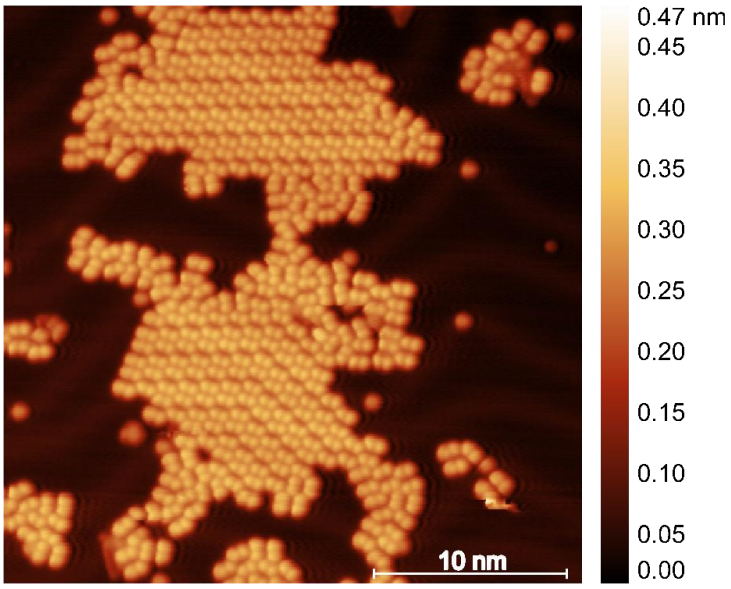

Figure 5. 5 : 4 K STM image of TBA molecules on Au(111). An ordered island of molecules with some disordered part of molecules are visible. The trans-TBA molecules have a STM signature of 4 lobes. STM parameters: -1 V / 5 pA .

The Figure 5. 7 shows isolated TBA molecules on Au(111) terraces. The TBA molecules are always positioned at the elbows of the Au(111) herringbone reconstruction. The elbows act as nucleation sites. The isolated molecule can nearly move under the influence of the tip in normal tunneling conditions (-1V / 5pA). This reveals that molecules have a weak interaction with the substrate. Individual molecules can also be found on step edges (see Figure 5.6).

A unit cell is proposed in Figure 5. 7 b) for this *trans*-TBA island lattice. It has side lengths of 1.06 ± 0.04 nm and 1.42 ± 0.05 nm, and an opening angle of 107 ± 1°. These values are in full accordance with those measured on a similar molecule (TBA with a methoxy group), as measured by AFM on calcite with reported values of 1.04 ± 0.04 nm, 1.56 ± 0.03 nm and 106.9 ± 0.5° respectively[243].

In larger islands TBA molecules can adopt different type of configuration denoted as phases[242,244]. The Figure 5. 6 illustrated STM image of different phases of TBA molecules on Au(111). The different phases vary in their molecule-molecule ordering and orientation with respect to the Au(111) herringbone. All individual molecules have identical appearances before they are exposed to light regardless of the phase, indicating that they are all in the same (*trans)* configuration. As presented by Levy et al.[242], up to three different *trans*-TBA molecules self-assembly phases can be seen after deposition of TBA on Au(111). However only two of them are observed during our experiments presented in Figure 5. 6). The absence of phase 3 is due to a low frequency of occurrence as reported by Levy et al.[242]. Each phases displays a different organization, which has an impact on the photoswitching behavior[242].

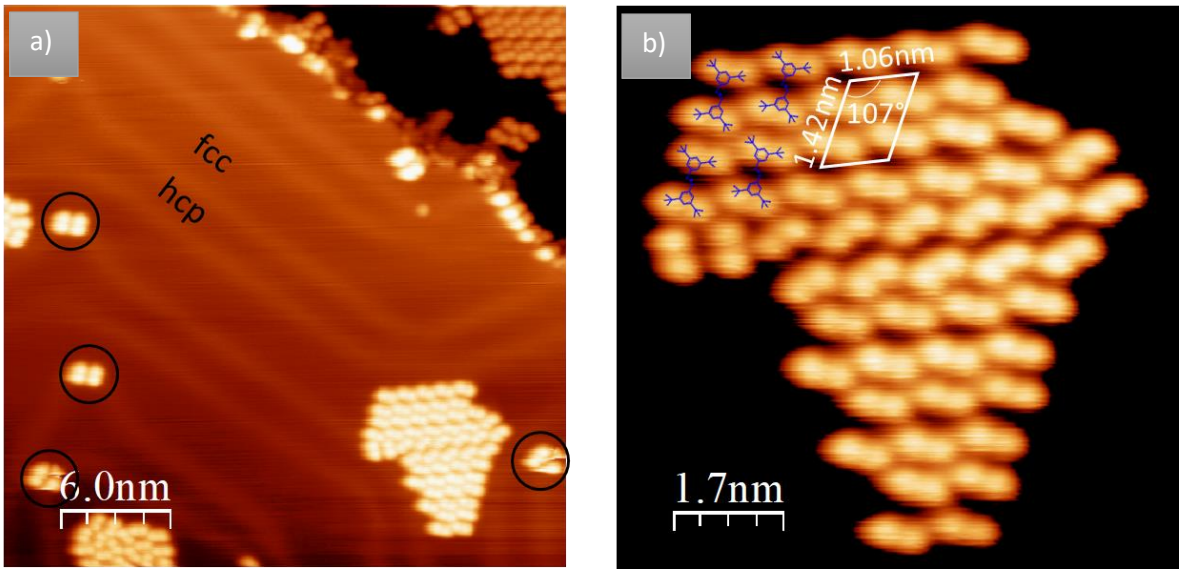

Figure 5. 7 : a) STM image of TBA after deposition on Au(111), 30 nm x 30 nm, I = 10 pA, V = - 1.5 V at 4 K. Circles correspond to single TBA molecules localized at the elbows of the Au(111) herringbone reconstruction. The characteristic Au(111) (22 x √3) "herringbone" b) Focus on an island composed of organized trans-TBA molecules, 8.7 x 8.7 nm², I = 10 pA, V = + 1.5 V.

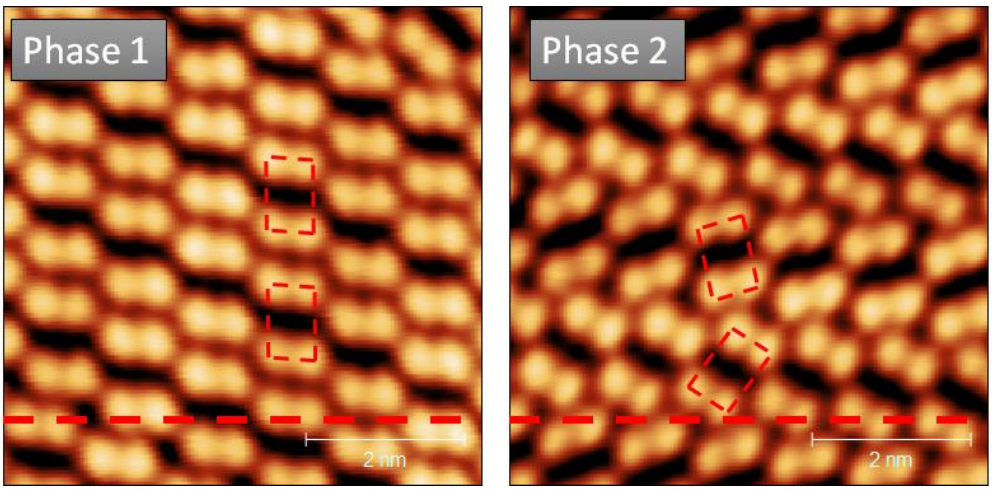

Figure 5. 6 : Current-constant STM topo of phases 1 and 2 of the trans-TBA on Au(111). The red box surrounding a single molecule to indicate different placement between phases. The herringbones are parallel to the red dashed line.

The phase 1 is close-packed and has one molecule per unit of cell and an orientation tilted of 88 ± 4° with herringbone, when the phase 2 has 2 molecules per unit of cell with one molecule an orientation tilted of 52 ± 5° and another at 107 ± 5°. This value is consistent with that of Levy et al.[242]

5.3 TBA isomerization induced by the polarized tip

5.3.1 Model for electro-isomerization to the *cis*-isomer

A model for the conformation of the *cis*-isomer adsorbed on Au(111) was proposed by Erik R et al[205] and is represented in Figure 5. 8.

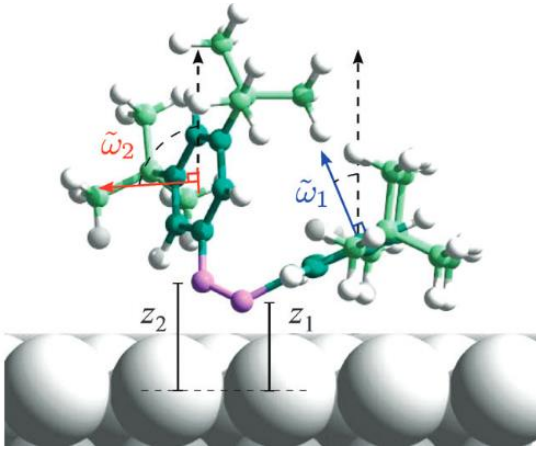

Figure 5. 8 : Side view of adsorbed cis-TBA at Au(111). The parameter z_i is the vertical height of the two diazo-bridge N atoms and w_i the out of horizontal phenyl plane bend angle. Adapted from[205].

Grill et al[219] expose that the isomerization of the TBA molecule on Au(111) driven by the electric field with the STM tip, have these properties: (i) it does not involve tunneling of electrons (ii) it operates at both polarities (iv) it has a large lateral extension (i.e. is not limited to the molecules under the tip).

The first theoretical study on the switching of azobenzene by an electric field was proposed by Füchsel et al.[245]. The principle of the electro-isomerization is based on the following mechanism: in presence of an electric field, the energetic pathway can be deformed and so the energy needed to overcome the barrier is lowered. However, the presence and orientation of an intrinsic dipole moment is needed. The Figure 5. 9 from[245] shows calculations of the energy shifts for the two isomers of TBA. The assumption was made that the molecule in *trans* state lays flat on the surface with the N-N axis and phenyl rings parallel to it, so in this case the electric field is homogeneous perpendicular to the molecule. Two models are shown: the model A (Figure 5. 9 left) considers a permanent molecular dipole and induced dipole perpendicular to the surface. In the model B (Figure 5. 9 right) the permanent dipole is aligned with the surface when the induced dipole is perpendicular to the surface.

One difference between the two models is the asymmetry of the model A to switch the molecule for positive and negative bias. When the electric field is antiparallel to the permanent dipole, the molecule is more able to be destabilized (dashed lines on model A in Figure 5. 9). This means that the orientation of the intrinsic molecular dipole with respect to the electric field leads to variation of the field needed for the isomerization by changing sign of the electric field. For the solid line, model A denotes a lower energy to the *trans*-> *cis* state, while the *cis*->*trans* require more energy than the model B.

The threshold voltage is also determined by the tip height regime, Grill et al.[219] made an experimental investigation of the dependence of the voltage necessary for the isomerization on the tip height for both polarities and isomerization process. For the *trans*->*cis* isomerization the threshold voltage varies with the distance as 0.1 V/Å (V>0) and 0.7 V/Å (V<0), while for the *cis*->*trans* as 0.3 V/Å (V>0) and 0.2 V/Å (V<0). These values are smaller than those calculated by Füchsel et al[245] in gas phase of 1.5 V/Å. The difference between experimental and theoretical values for the threshold voltage is probably due to the fact that molecular calculus are made in the gas phase in the theory approach.

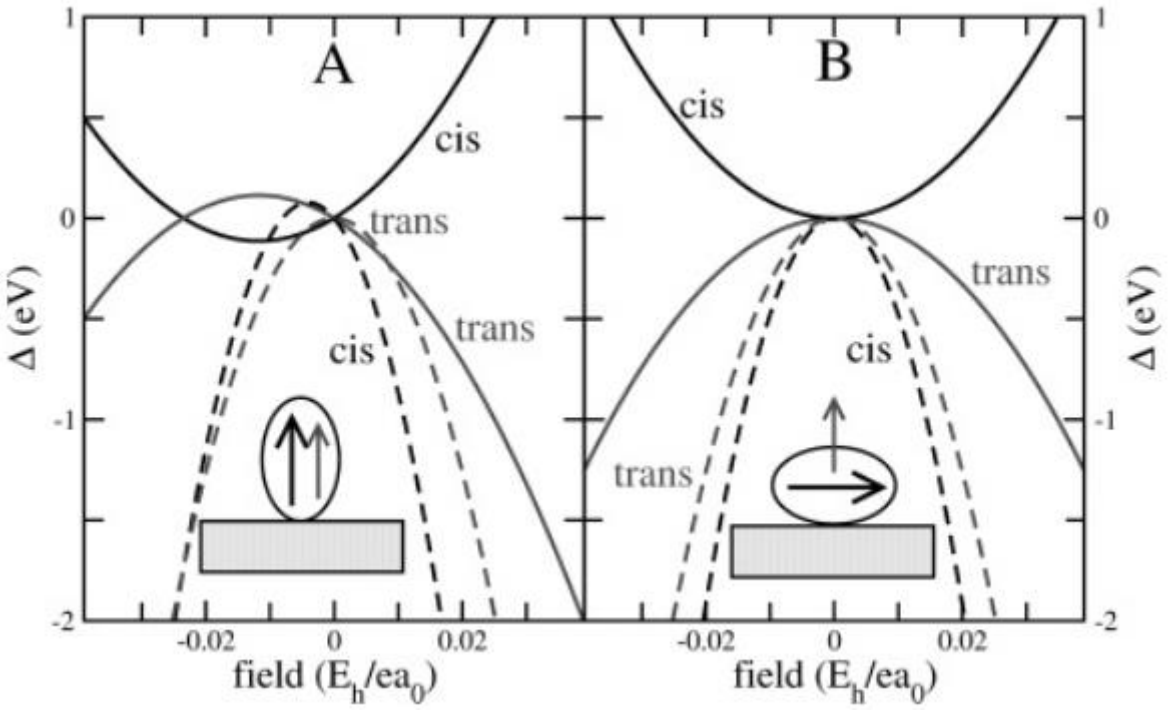

Figure 5. 9 : Calculated energy barrier (solid lines) and shifts of the energy barrier (dashed lines) for the cis and trans isomers. The A model represents the permanent molecular dipole represented by a thick arrow and the induced dipole moment by a thinner arrow. Each dipole is aligned with the electric field. In the model B, the intrinsic dipole moment is perpendicular to the electric field. Adapted from[245].

5.3.2 Electro-isomerization of TBA on Au(111)

TBA molecules can switch under an electric field exposition, a process known as electroisomerization. Scanning probe microscopes are adapted tools to investigate this isomerization process at the

nanoscale. Recently, Alemani *et al.* observed the TBA electroisomerization using the electric field induced by a STM tip[219,221,246]. We performed electroisomerization by imaging at ± 2 V / 5 pA STM condition which is softer condition than Alemani et al.[219] experiment who applied subsequent voltage pulse. The Figure 5. 10 shows successive STM images of a *trans* TBA island freshly deposited on Au(111)

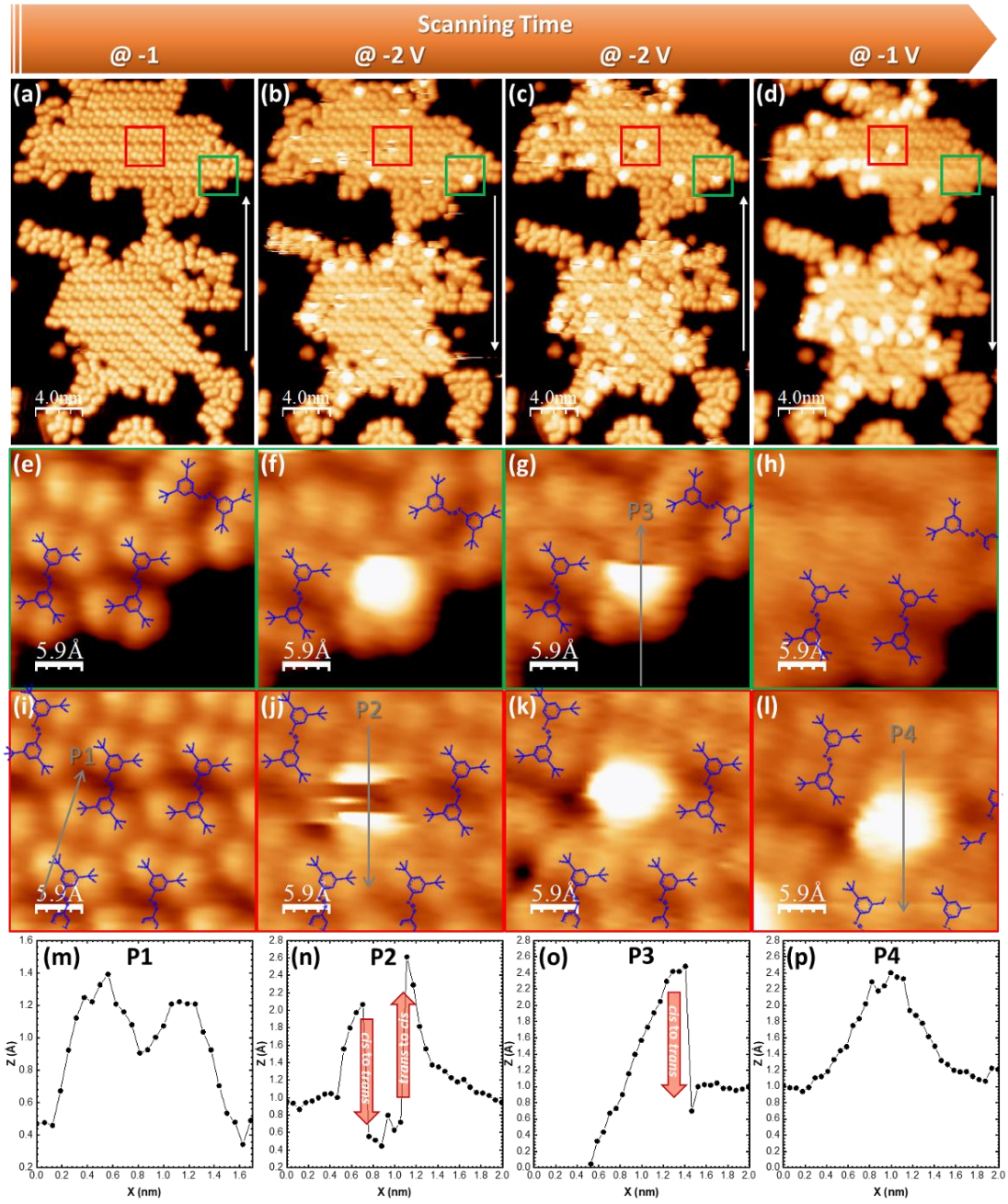

Figure 5. 10 : Four successive 20 x 30 nm² images of a TBA island were acquired by STM at 4 K (I = 5 pA) with respectively V = -1 V in Y-scan upward (a); V = -2V in Y-scan downward (b); V = -2 V in Y-scan upward (c) and V = – 1 V in Y-scan downward (d). White arrows indicate the Y scanning direction. Each image was measured in approximately 6 min 30 s. The two sequences (e), (f), (g), (h) and (i), (j), (k), (l) are zoomed images (size 2.9 x 2.9 nm) of the previous images (a), (b), (c), (d), corresponding to the green and red squares respectively. Four topographic profiles P1, P2, P3 P4 represented by grey arrows in respectively (i), (j), (g), (l) images are plotted in (m), (n), (o), (p) respectively. The direction of the grey arrows indicate the direction of the scan in Y, which also corresponds to the increasing X in the topographic profile graphs.

and composed of approximately 180 molecules, using a bias of -1 V, -2 V, -2 V and -1 V (see Figure 5. 10).

Two zoomed STM images on few molecules (represented by red and green squares in Figure 5. 10 a)) are shown in the Figure 5. 10 e) to Figure 5. 10 l), in order to illustrate the electroisomerization process The two zoomed images acquired at - 1 V after deposition (Figure 5. 10 e) and i)) are similar with those of the Figure 5. 7 with the presence of the 4 lobes corresponding to the molecule in the *trans* configuration and organized in a network. During imaging at - 2 V (Figure 5. 10 b) and c)), we observe the occurrence of bright features for both sets of zooms. But at the end of the voltage sequence, the zoom shown by the green square leaves the molecule on his initial state (Figure 5. 10 h)), while the zoom shown by the red square ends with a bright spot instead of the molecule. In the first case, the molecule returns to the *trans* conformation, while in the second case the molecule stays in the *cis* conformation. The apparition of this bright spot is associated to an increase of the apparent height of 0.23 ± 0.02 nm (profile in Figure 5. 10 p)), which is characteristic of the formation of a *cis*-TBA isomer on the gold surface[219,221,247]. This *trans* to *cis* isomerization was caused by the application of a higher electric field during STM imaging at -2V[219,245]. The same switching behavior was also observed during imaging at +2 V at 77 K (see Figure 5. 12), showing that the isomerization under higher electric field occurs at both polarities. In STM images, all *cis*-isomers have the same appearance. As in Figure 5. 10, the *cis*-TBA state appears with a maximum intensity localized at the center of the molecule and with three lateral lobes around this maximum. The STM images show that the *cis*-conformation is different from the planar *trans*-conformation. In the STM images (see Figure 5. 10 j) k) i)) two lateral lobes with the same intensity are assigned to the legs of the molecule. The maximum intensity is due to the legs pointing upwards. It turns out that *cis*-TBA is not planar like the model presented in the Figure 5. 8 suggest. The tunnel current in our case is only a few pA. For these values, the current cannot participate in the switching mechanism of the molecule as demonstrated in the literature[246,248].

The fraction of TBA molecules that switch from the *trans* to the *cis* states increase at a sample bias of -2 V. The Figure 5. 11 a) represent the total fraction of *cis*-molecule as a function of the successive number of STM scan at -2 V on the island. To plot this graph the total number of *trans*-TBA molecules is taken on the island of the Figure 5. 11 b) c) and as going along successive -2 V scans was made, *cis*-molecules change fraction is counted. The fraction of *cis* molecules increase rapidly to saturate at ~0.25 after 4 scans at -2V.

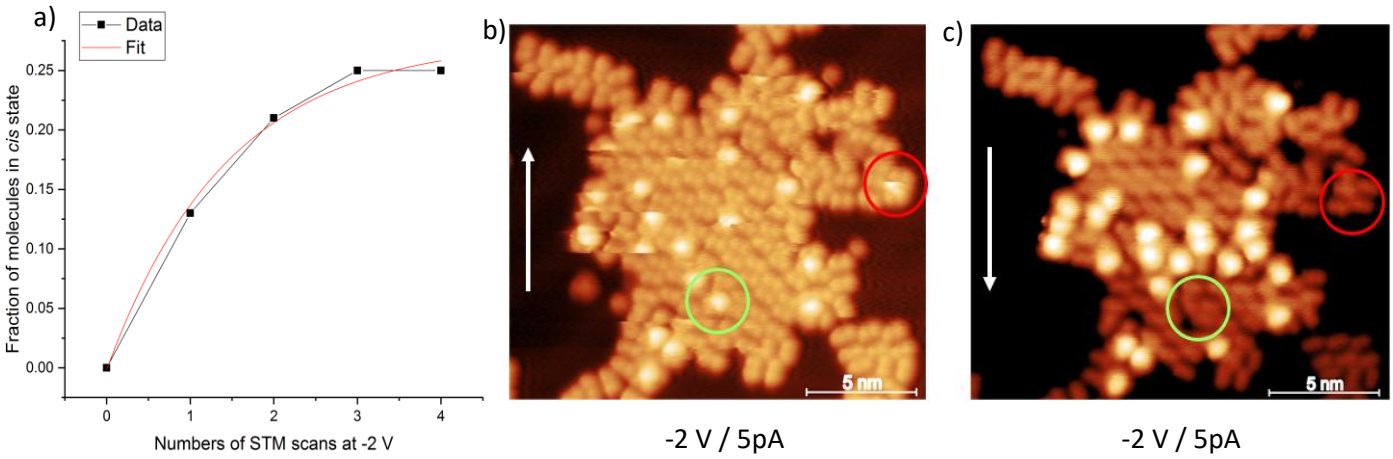

Figure 5. 11 : a) Fraction of cis-TBA molecules on Au(111) on a total of 180 molecules plotted vs numbers of STM scans made at -2 V. Red lines are fits to dates using Monomolecular growth model. b) c) Successive STM image at -2 V/ 5 pA, red and green circle highlight area where the TBA molecules switch from cis state back to trans state.

Successive STM images at 77K of a *trans*-TBA monolayer on gold with +2 V tip polarized are shown on the Figure 5. 12. The red square in the Figure 5. 12 a) highlights a TBA molecule switching from the *trans* to the *cis* state. In the following scan, the TBA in this region returns to the *trans* state (Figure 5. 12 b)). A Zoom is made on this region (Figure 5. 12 c)) shows that the bright spot is not well defined (Figure 5. 12 a) and b)). This phenomenon is similar to the one observed on the island at 4K above. The abrupt change of height on the profile (Figure 5. 12 d)) shows the isomerization process is faster than the time between two lines in the STM scan (≈1 line/sec). The apparent height is equal to 0.24 ± 0.02 nm (profile in Figure 5. 12 d). This value is close to the one measured on TBA island (Figure 5. 10). The raise of temperature up to 77 K, the coverage and the change of polarization to +2 V on the Au(111) does not change the electroisomerization properties of the TBA.

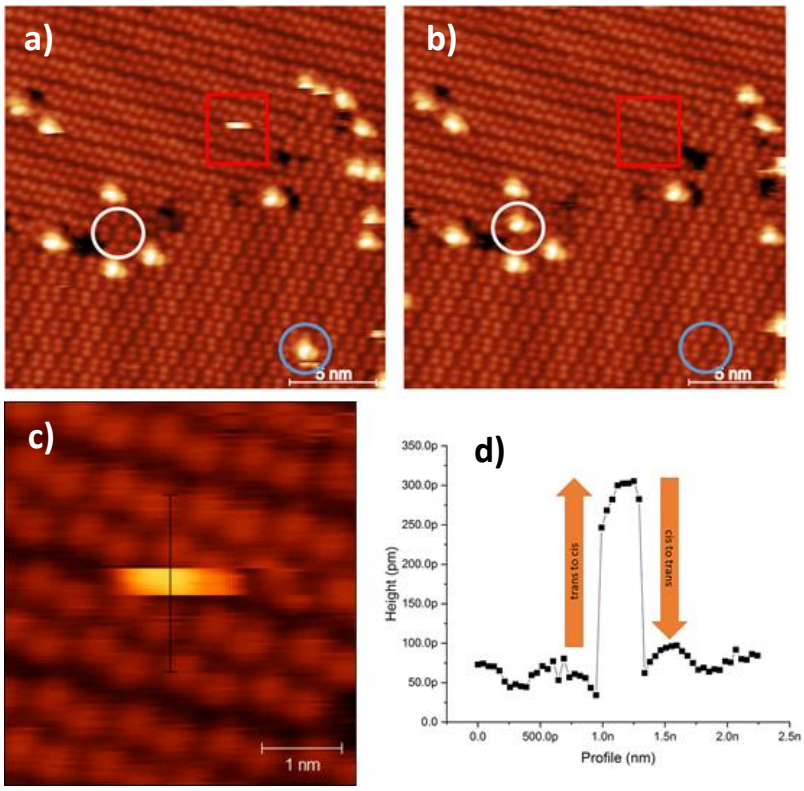

Figure 5. 12 : Two successive 22 x 22 nm² images of a TBA monolayer were acquired by STM at 77 K(I = 2 pA) at respectively V = +2 V in Y-scan upward a); V = +2 V in Y-scan downward b); Each image was measured with a scan speed of 25 nm/sec, image c) is zoomed images (size 5 x 5 nm) of the previous image a), corresponding to the red squares. Topographic profile P1 represented by red lines in c) image is plotted in d).

5.4 Effect of UV irradiation on TBA molecule

5.4.1 Models for *cis*-isomer after photo-isomerization

The photoisomerization of azobenzene in solution was extensively studied[228,233,249]. However, when the molecule is in interaction with a metallic substrate several mechanisms need to be considered during the light irradiation of adsorbed molecules[239]: (i) direct intramolecular excitation, (ii) surface excitation, (iii) thermal excitation. Direct intramolecular excitation occurs when a photon is absorbed by the molecule via a direct optical *trans*ition between the HOMO and the LUMO (see Figure 5. 13 a)). In surface excitation, the photon absorption occurs in the surface. A charge *trans*fer occurs via the photo-excited charge carriers from the substrate to the molecule and an excited state is reached. The Figure 5. 13 presents the excitation *trans*fer process. Martin Wolf et a.l[250] proposed that photoisomerization of TBA on Au(111) is induced by surface charge *trans*fer process. Upon irradiation,

hot holes in the Au(111), relax to the top of Au-d band and make a *trans*fer to the HOMO of the molecule resulting in photoswitching process.

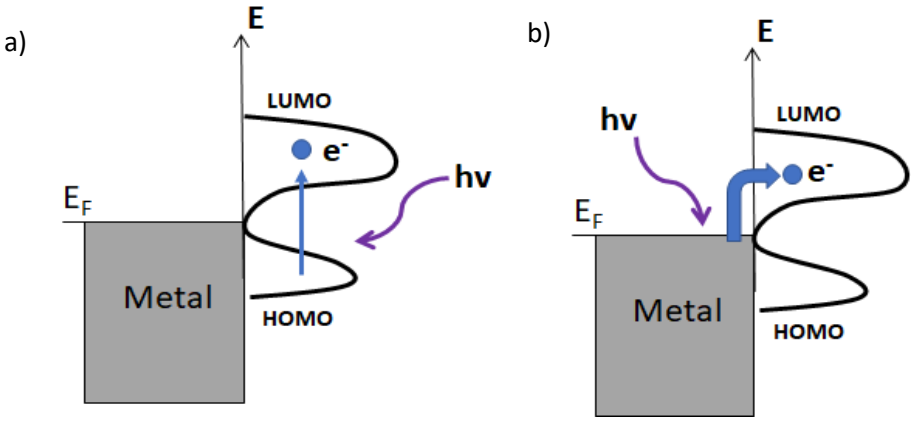

Figure 5. 13 : Energy diagram for surface molecule chemistry. The energy level lies between the HOMO and LUMO of the molecule. a) Direct intramolecular excitation b) Surface excitation leads to photo-excited charge carrier transfer from the surface to the absorbate molecule.

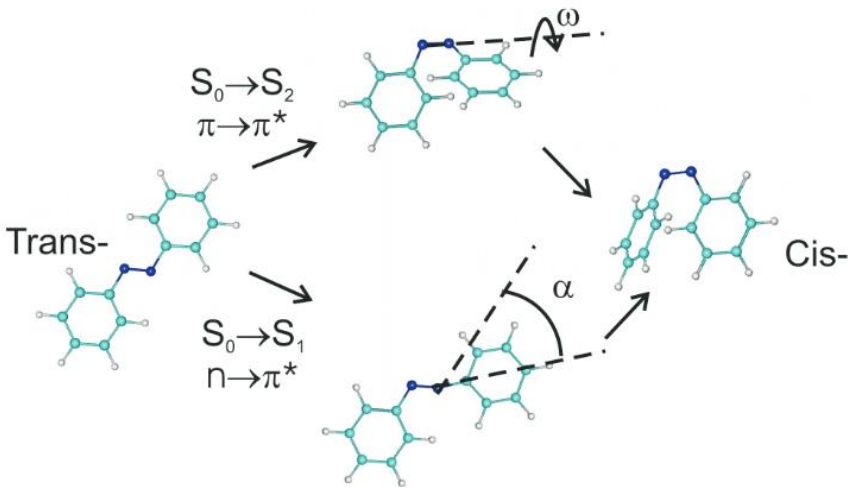

Figure 5. 14 : Schematics of photo-isomerization: inversion and rotation paths are shown. Relevant conformation coordinates are the w angle for the rotation mechanism (rotational axis is the N=N bond), and the angle of the α for the inversion (rotational axis perpendicular to the drawing plane). Adapted from[246].

For the photo-isomerization dynamic process, it is well known that the excitation mechanism occurs on excited states, through an intersection with the ground state potential energy surface[205,228,230,231]. Various pathways are theoretically proposed for the photoisomerization[230,233]: (i) an inversion around the N=N bond; (ii) rotation around the N=N bond combined with some degree of inversion of one NNC angle. The rotation around the N-N bond is associated to a S_0 -> S_2 excitation related to the HOMO-1 -> LUMO excitation, when the inversion of the NNC angle was associated with S_0 -> S_1 excitation that corresponds to the HOMO-> LUMO excitation (see Figure 5. 14).

5.4.2 Photoisomerization of TBA islands deposited on Au(111)

In order to compare the effect of UV irradiation with the electric field, surfaces with freshly deposited TBA islands on Au(111) were illuminated in UHV according to the absorbance spectra (see Figure 5. 4) with UV at 304 nm during 15 hours (with a power density estimated at 0.5 mW/cm^2). After UV illumination, TBA islands present a different morphology compared to STM images after deposition (Figure 5. 15 a) black arrow pointing). We observe after UV irradiation, areas in the islands with a lower apparent height (0.10 ± 0.01 nm) than the lobes (Figure 5. 15 b)). This lower thickness is confirmed by nc-AFM imaging (Figure 5. 15 d)), showing that it is not a purely electronic effect. A zoom on an island with this low thickness area (Figure 5. 15 c)) shows a pattern with parallel linear structures with a spacing of 0.46 ± 0.05 nm. Lobes assigned to *tert*-butyl legs are not associated by 4, as observed after TBA evaporation, which indicates a dissociation or an alteration of the TBA molecule under UV exposure as show the Figure 5. 16 circles. Also despite warming the substrate at 325 K during 12 h, and an irradiation with white light during more than 12 hours, the process did not prove reversible.

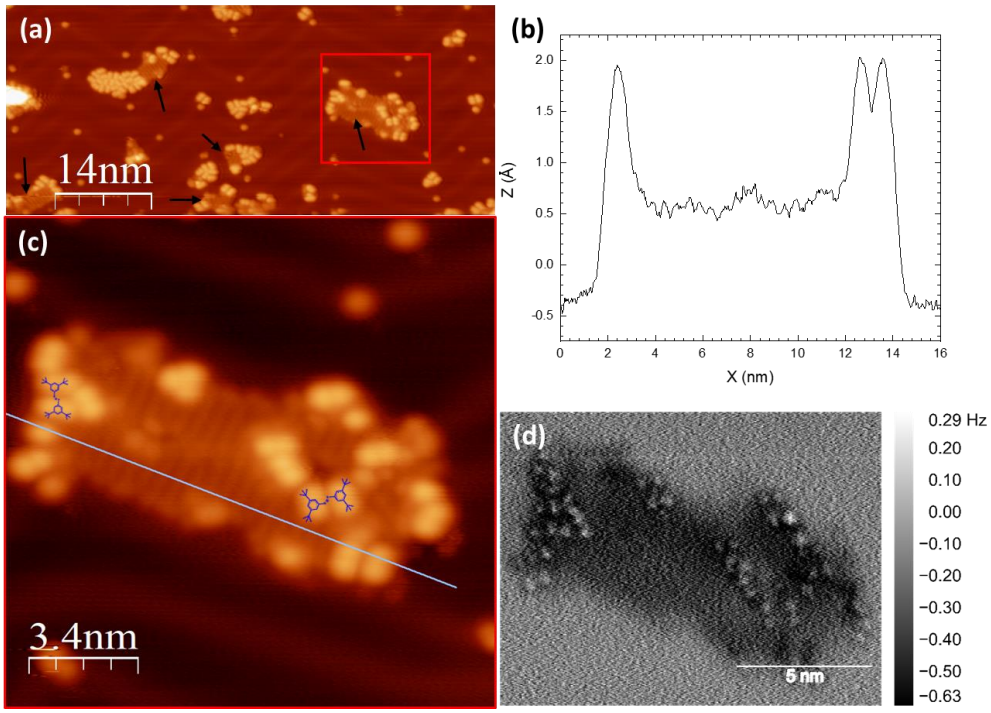

Figure 5. 15 : (a) 70 x 30 nm STM image, I = 5 pA V = - 1,1 V after UV exposition on TBA islands. Black arrows indicate low thickness area of the island not observed without the UV exposition; (b) z-profile corresponding to the grey line in (c); (c) 17 x 17 nm zoom corresponding to the red square in STM image presented in (a); (d) Corresponding nc-AFM acquired on the island presented in (c).

The apparition of linear pattern area on TBA island after UV irradiation has been observed reproducibly. However result is different from the structure observed by Dri and Levy[218,242] and from change observe in the part 5.3 where bright spots appear and were associated to the *cis*-TBA isomers.

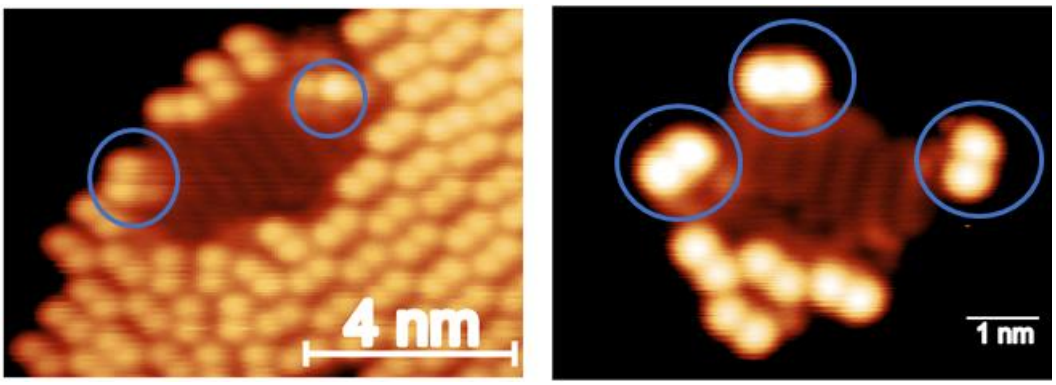

Figure 5. 16 : STM images of TBA after UV irradiation at 304 nm during 12 h. The blue circles indicate incomplete molecule (not associated by 4 as expected for the TBA molecule in trans state). The presence of only 2 lobes suggests the degradation of the TBA molecule under UV irradiation.

The main difference between experiments and the literature[211,240,242], using light irradiation to switch the TBA molecule is the wavelength used here is 304 nm (compare to 375 nm and power density of around 90 mW/cm² during up to 77 h[221,241,242] in the literature). According to the absorption spectrum of the TBA molecule, (see Figure 5. 4) the wavelength at 375 nm is off resonance of the absorbance peak, when in our case the wavelength of 304 nm is near to the center of the absorbance peak. So the energy use for the photoswitching process is higher of 0.8 eV and is in resonance with the absorbance peak of the molecule in our experiment.

To find an explanation of the area apparition after the UV irradiation, we need to look in detail the photoswitch mechanism from the *trans* to the *cis* state. The charge transfer process proposed by Wolf et al[222,250] has been studied. The dependence of the effective cross section for the light-induced *trans*->*cis* isomerization of the TBA adsorbate on Au(111) on the photon energy used was determined by the authors[222,250] (see Figure 5. 17 b)). A stepwise change is present at 2.2 eV, it follows a plateau region over the large photon energy 2.2 and 4.4 eV. Above 4.4 eV an exponential increase and bellow 2.2 eV a pronounced decrease are observed. To determine the excitation mechanism in the *trans*-> *cis*

a)

$E - E_F$ [eV]	Assignment
4.8	LUMO + m
4.45	LUMO + n (*cis*-TBA)
3.85	$n = 1$ (image potential state)
1.85	LUMO (*trans*-TBA)
1.55	LUMO (*cis*-TBA)
−0.48	$n = 0$ (Schockley surface state)
−1.8	HOMO
−2.0	Au *d*-band
−2.85	Au *d*-band
−3.0	HOMO-1

b)

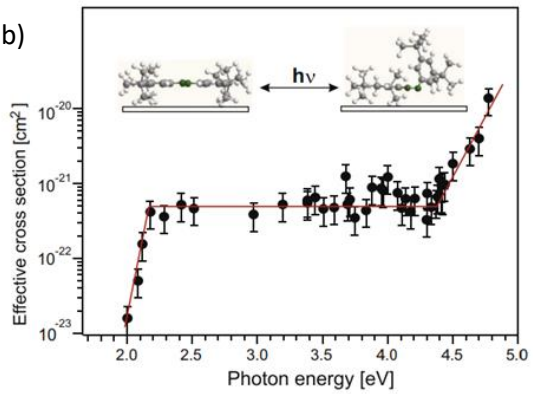

Figure 5. 17 : a) The energies of photoemission spectral feature of 0.9 monolayer TBA adsorbed on Au(111). Au(111) is the reference to the Fermi level. b) Effective cross section for the photoinduced trans/cis-isomerization of TBA adsorbed on Au(11 1) as a function of photon energy. Adapted from[222].

isomerization of the TBA, the electronic structure of the TBA/Au(111) is necessary. The Figure 5. 17 a) summarizes the binding energies of all electronic states[251], using the Fermi level of Au(111) as reference. HOMO and LUMO are separated by a band gap of 3.65 eV for the *trans*-TBA. A direct electro-excitation is incompatible with the photon energy dependence cross section (Figure 5. 17 b)) since no resonance in the cross section is observed in the region of 3.85 eV. So Wolf et al.[222] proposed the scenario where the mechanism is substrate-mediated. The excitation mechanism is shown in Figure 5. 18 with the density of state (DOS) of the Au d-band. The different steps of the mechanism are: (i) a hot hole is created in the Au d-band if the photon energy exceeding 2.2 eV; (ii) the hole relaxes rapidly to the top of the d-band; and (iii) the hole is then transferred to the HOMO level of the TBA molecule which induce the isomerization.

In our experiment, the wavelength of 302 nm corresponds to an energy of 3.78 eV. The energy lies in the plateau between 2.2 and 4.4 eV where the hot-hole of the Au d-band can be created and enable the switch of the molecule. After or during the switching process the literature shown, the azobenzene in cis form can form cation/anion when it interacts with gold[252,253]. The presence of only 2 lobes instead of 4 on STM and AFM image (Figure 5. 16) suggests that the molecules were split apart. The hypothesis proposed here is that hot holes created by the UV irradiation switch the molecule from the *trans* to the *cis* state. During or after the TBA molecule switching to the *cis* state, the molecule interacts and shares electrons with the gold substrate[252–254]. Due to this reaction, the double N=N bond get affected and is susceptible to be broken easier. A N=N bond can be broken with an energy of 4.2 eV[255] and so

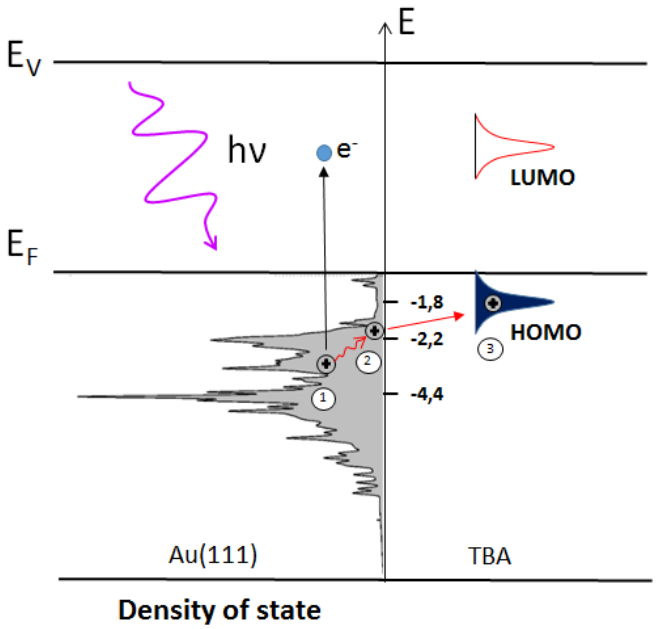

Figure 5. 18 : Excitation mechanism for photoisomerization of TBA molecule on Au(111). The photoexcitation at phonon energies above 2.2 eV leads to electron-hole pair formation (step 1). The holes in the Au d-band relax to the top of the d-band (step 2) and transfer to the HOMO of the TBA (step 3). Adapted from[222].

with a wavelength of 302 nm (≈ 4.0 eV) the chemical bond can be broken and the molecule is split apart leading to the appearance of our lobes not matched by four in our images.

5.5 Conclusion

Our challenge was to understand how the TBA molecules adsorbed on a Au(111) substrate switch from the *trans* to the *cis* state reversibly when subjected to an electric field and/or UV irradiation. After the adsorption on the substrate, all the molecules are in *trans* state with a characteristic 4-lobes planar signature in the STM images. Molecules are either isolated at the elbow of the herringbone reconstruction of the Au(111), or adsorbed in large ordered islands. By scanning with the STM at a voltage of ±2 V, the isomerization of the TBA was induced in a reversible way. The configuration of the *cis*-TBA was observed on Au(111) by the apparition of bright spots on the substrate. The mechanism of the electro-isomerization was discussed. In our case, the electro-isomerization process is only induced by the electric field. The tunnel current is only a few pA and according to the literature cannot participate in the switching mechanism.[246,248]. A theoretical model by Füchsel et al.[245], which explains the isomerization of TBA molecules by electric fields, has been discussed to understand the main mechanism in the electroisomerization of the molecule adsorbed on Au(111).

The isomerization of the molecule with a UV irradiation leads to the observation of striped region, with a thickness lower than the TBA molecule on *trans* state is observed. The nc-AFM analysis confirms the lower topography of the area and excludes some electronic phenomena on the STM image. The analysis of the photo-mechanism was discussed. The creation of a hot hole on the d band follows by a hole transfer into the HOMO of the molecule could explain the switch to the *cis* state. During or after the switching process, the molecule interacts with gold and affects the N=N double bond. In addition, with the UV radiation at 302 nm, this N=N bond can be broken leading to the deterioration of the molecule.

General conclusion and outlook

Near-field microscopy has become an essential tool for observing and characterizing molecules. This thesis work brought together the technique of the near-field microscopy and the molecular system with diverse function in the field of molecular nanoelectronics. We work on a molecular nanocrystal, switching state molecule and chain oscillating molecule. The influence of the substrate on molecules shown how it can be challenging to deposit molecules on metallic substrate and can be a key factor in exploiting the various properties of molecules for applications in molecular electronics.

Chapter 1 resituated the context of the thesis. A quick story of nanotechnology with his different applications were exposed. A focus on molecular nanoelectronics was then made and a non-exhaustive list of molecular electronic functions was presented.

Chapter 2 presented the concept of the scanning probe microscopy with the theory. Different topographic mode uses in this thesis are described. The two different types of probe to make measurement are presented with their different physical properties. The different type of noise source that we may encounter during an experience is described and explained.

In **chapter 3**, we have presented a study of a molecular junction composed of nanocrystal of Prussian Blue analogue CsCoFe with an ambient air AFM. The CsCoFe nanocrystal shows versatile physical and chemical properties that can be tuned by external stimulus such as temperature, light, and electrical and magnetic fields. Different sizes of 15, 30 and 50 nm nanocrystals CsCoFe are studied in the junction. After the deposition on a HOPG substrate, the density and height of nanocrystal were verified with an AFM in ambient air condition. Isolated nanocrystals can be found and by using the tip of the AFM as top electrode electrical measurement was performed. To help us to understand the mechanism of charge transport in such systems, the single orbital energy and Double Schottky barrier model has been used. Electrical measurements in function of the force applied on a CsCoFe nanocrystal of 15 nm permit to estimate the effect of the contact area of the tip-molecule interface on the current. Following this, electrical measurements were performed on different isolated nanocrystals of 15 nm, 30 nm and 50 nm. These measurements revealed a counterintuitive behavior where the recorded current values were higher for 50 nm than for 15 nm nanocrystals. A classical way of treating the current curves is to fit them with the single energy orbital model. Despite a reasonable fit of the curves, the parameters do not explain the current increase. Due to the size of the nanocrystals, the system should be considered as "macroscopic" rather than as a pure molecular junction. In this context, the double Schottky barrier model allowed us to relate the observed increase in current to a lowering of the energy barrier for the tip-nanocrystal junction for 30 nm and 50 nm PBAs. For 15 nm PBAs the tip-

nanocrystal barrier height is 0.31-0.35 eV while for 30 nm and 50 nm PBAs this barrier value drops to about 0.24 eV. The barrier value of the 15 nm, 30 nm and 50 nm PBAs were compared with theoretical values of the molecular orbital literature for a 19 nm CsCoFe nanocrystal. The correspondence between the theoretical values and the barrier heights found with the Schottky model allowed us to favor the hypothesis of transport via the molecular orbital t_{2g} of the Fe^{II} in this type of system.

Chapter 4 was about BDPA molecule deposit on Au(111). Near-field microscopy measurement was performed with a JT-SPM under UHV at 4 K and 32 K. The first part was about the auto assembling properties of the BDPA molecule. Once the molecule is deposited on Au(111) it will organize itself into different clusters of 1, 2 or 3 BDPA molecules or chains form. The first STM image shows the molecule in bean shape and allowed us to assume a first orientation of the molecule when it is assembled in a chain. To obtain additional information the nc-AFM has been done. A high resolution was obtained and the phenyl unit due to is lower height inside the molecule was recognized. The second part of the chapter was about the vibrational properties of BDPA chain on Au(111) when the temperature is above 25 K. Indeed, above this temperature the BDPA chain behaves like a one-dimensional harmonic oscillator. The literature reports that phonon-molecule coupling is responsible for the oscillations of BDPA chains. We performed STM analysis of BDPA chain at 32 K where the outline of the vibration is clearly visible for +1V polarization. Similarly to a harmonic oscillator, different types of vibration modes are observed. We report a first and a second eigenmode of the BDPA chain with $L = \lambda/4$ and $L = 3\lambda/4$ respectively. When we switch to -1V polarization, the outline of the vibration disappears. This indicates that the vibration of the BDPA chain is highly reduced or stopped. A KPFM grid spectroscopy was performed to study the charge state of the molecule as a function of the polarization of the substrate. The spectroscopy shows in negative bias (negative polarization applied on the substrate) no net charge on the molecule, however for positive bias (positive polarization applied on the substrate) the molecule show a substrate-molecule negative charge of ≈ -0.6 V and assume that the SUMO molecular orbital is filled.

To conclude on **chapter 5**, we analyze by STM and nc-AFM in UHV at low temperature, a derivative azobenzene TBA on Au(111) as a switch molecule with a *trans* and *cis* state. The molecule in *trans* state after the deposition was recognized as 4 lobes shape in STM images. Different types of organization were observed denoted as phase. A first phase is the close-packed with 1 molecule per unit cell and an orientation tilted of 88 ± 4° with the herringbone, the second phase has 2 molecules per unit cell with one molecule an orientation tilted of 52 ± 5° and another at 107 ± 5°. Two stimuli were employed to change the *trans* state of the molecule to the *cis* state. The first stimulus used is an electric field produced by the tip during the STM experiment. By scanning at a bias of ±2 V, we observed the apparition of bright spots associated to the TBA molecule in *cis* state. The evolution of the fraction of

molecule in cis state with the number of scan shown an exponential shape to finally saturate rapidly (after 4 images) at 25% of the total number of molecule present in the image. A fresh deposit of molecules has been prepared to use UV illumination as stimulus. The result found was different as the electrical field stimulus. Instead of the apparition of a bright spot, STM images reveal regions with height lower than the molecule in *trans* state. Region was analyse with nc-AFM which confirmed the region physically got a lower topography than *trans* TBA molecule. The presence of 2 lobes instead of 4 on STM and nc-AFM image suggests that the TBA molecule has been split. An analysis of the switch mechanism with the various energy contributions was made and we conclude that the switching of the molecule is substrate mediated with hot hole transferred inside the HOMO, and during or after this process the molecule is split.

Outlook

The electrical measurement on the CsCoFe was made. The new goal would be now to exploit the spin properties of the molecule. To accomplish this, ultra-high vacuum and low temperature are necessary. Illuminate in the 600 nm range at low temperature will change the low spin state of the molecule to high spin state resulting in an expecting change of resistivity and so two distinct states. The relaxation from high spin state to low spin state with the increase of the temperature in function of the size of the nanocrystals can also be studied. To finish spin polarized scanning tunneling microscopy experiment is also a possibility to exploit a possible effect of tunnel magnetoresistance in magnetic tip-PBA-substrate system.

The measurement of the BDPA chain reveals that the harmonic oscillator properties are not only due to molecule-phonon coupling and are still not well understood. Further experiments to see the oscillation in function of polarization in nc-AFM can be considered, but a special care must be taken to not disturb the system with the tip.

Concerning experiments with AZBT molecule, this study shows at which point understanding the substrate-molecule interaction is a key point for potential applications in molecular nanoelectronics. More experiments to confirm the alteration of the molecule due to UV irradiation should be done.

Publications & Oral communications

Publications

- Electronic transport probed by conducting AFM through single Prussian blue analog nanocrystals : a double Schottky model (*in progess*)

Hugo Therssen, Talal Mallah, Dominique Vuillaume, Thierry Mélin, Stéphane Lenfant

- **Comparison Between the Effect of Ultraviolet Exposure and Electric Field on an Azobenzene Derivative Molecule Deposited on Au(111) (*in progess*)**

Hugo Therssen, Sylvie Godey, David Guérin, Thierry Mélin, Stéphane Lenfant

Oral communications

- Comparison of the effect of ultraviolet light or electric field on an azobenzene derivative deposited on Au(111)

Hugo Therssen, Sylvie Godey, David Guérin, Thierry Mélin, Stéphane Lenfant

Forum des microscopies à sondes locales – Saint-Valéry-sur-Somme, France (2022)

-**Behavior of an azobenzene derivative on gold exposed to electric field and ultraviolet light**

Hugo Therssen, Sylvie Godey, David Guérin, Thierry Mélin, Stéphane Lenfant

GDR nanoscience en champ proche sous ultra vide – Toulouse, France (2021)

- Imaging BDPA molecule chain with STM and non-contact AFM

Hugo Therssen, Sylvie Godey, David Guérin, Thierry Mélin, Stéphane Lenfant

European school on molecular nanoscience (EsMolNa) – Benidorm, Spain (2021)

Bibliography

(1) Kulkarni, S. K. *Nanotechnology: Principles and Practices*; Springer International Publishing: Cham, 2015. https://doi.org/10.1007/978-3-319-09171-6.

(2) Loos, M. Nanoscience and Nanotechnology; 2015. https://doi.org/10.1016/B978-1-4557-3195-4.00001-1.

(3) Mei, L.; Zhang, Z.; Zhao, L.; Huang, L.; Yang, X.-L.; Tang, J.; Feng, S.-S. Pharmaceutical Nanotechnology for Oral Delivery of Anticancer Drugs. *Adv. Drug Deliv. Rev.* **2013**, *65* (6), 880–890. https://doi.org/10.1016/j.addr.2012.11.005.

(4) Jabir, N. R.; Tabrez, S.; Ashraf, G. M.; Shakil, S.; Damanhouri, G. A.; Kamal, M. A. Nanotechnology-Based Approaches in Anticancer Research. *Int. J. Nanomed.* **2012**, *7*, 4391–4408. https://doi.org/10.2147/IJN.S33838.

(5) Lu, J.; Chen, Z.; Ma, Z.; Pan, F.; Curtiss, L. A.; Amine, K. The Role of Nanotechnology in the Development of Battery Materials for Electric Vehicles. *Nat. Nanotechnol.* **2016**, *11* (12), 1031–1038. https://doi.org/10.1038/nnano.2016.207.

(6) Gnach, A.; Lipinski, T.; Bednarkiewicz, A.; Rybka, J.; Capobianco, J. A. Upconverting Nanoparticles: Assessing the Toxicity. *Chem Soc Rev* **2015**, *44* (6), 1561–1584. https://doi.org/10.1039/c4cs00177j.

(7) Feynman, R. P. There's Plenty of Room at the Bottom. *Engineering and Science* **1960**, *23* (5), 22–36.

(8) Pierret, A.; Hocevar, M.; Diedenhofen, S. L.; Algra, R. E.; Vlieg, E.; Timmering, E. C.; Verschuuren, M. A.; Immink, G. W. G.; Verheijen, M. A.; Bakkers, E. P. A. M. Generic Nano-Imprint Process for Fabrication of Nanowire Arrays. *Nanotechnology* **2010**, *21* (6), 065305. https://doi.org/10.1088/0957-4484/21/6/065305.

(9) Binnig, G. Tunneling through a Controllable Vacuum Gap. *Applied Physics Letters* **1982**, *40* (2), 178. https://doi.org/10.1063/1.92999.

(10) Binnig, G.; Rohrer, H.; Gerber, C.; Weibel, E. Surface Studies by Scanning Tunneling Microscopy. *Physical Review Letters* **1982**, *49* (1), 57–61. https://doi.org/10.1103/PhysRevLett.49.57.

(11) Binnig, G.; Quate, C. F.; Gerber, C. Atomic Force Microscope. *Physical review letters* **1986**, *56* (9), 930–933. https://doi.org/10.1103/PhysRevLett.56.930.

(12) Kislyuk, V. V.; Dimitriev, O. P. Nanorods and Nanotubes for Solar Cells. *Journal of Nanoscience and Nanotechnology* **2008**, *8* (1), 131–148. https://doi.org/10.1166/jnn.2008.N16.

(13) O'Farrell, N.; Houlton, A.; Horrocks, B. R. Silicon Nanoparticles: Applications in Cell Biology and Medicine. *Int. J. Nanomed.* **2006**, *1* (4), 451–472. https://doi.org/10.2147/nano.2006.1.4.451.

(14) Holzinger, M.; Le Goff, A.; Cosnier, S. Nanomaterials for Biosensing Applications: A Review. *Front. Chem.* **2014**, *2*, 63. https://doi.org/10.3389/fchem.2014.00063.

(15) Sothmann, B.; Sanchez, R.; Jordan, A. N. Thermoelectric Energy Harvesting with Quantum Dots. *Nanotechnology* **2015**, *26* (3), 032001. https://doi.org/10.1088/0957-4484/26/3/032001.

(16) Berthoumieu, O.; Patil, A. V.; Xi, W.; Aslimovska, L.; Davis, J. J.; Watts, A. Molecular Scale Conductance Photoswitching in Engineered Bacteriorhodopsin. *Nano Letters* **2012**, *12* (2), 899–903. https://doi.org/10.1021/nl203965w.

(17) Bleger, D.; Hecht, S. Visible-Light-Activated Molecular Switches. *Angew. Chem.-Int. Edit.* **2015**, *54* (39), 11338–11349. https://doi.org/10.1002/anie.201500628.

(18) Smaali, K.; Lenfant, S.; Karpe, S.; Oçafrain, M.; Blanchard, P.; Deresmes, D.; Godey, S.; Rochefort, A.; Roncali, J.; Vuillaume, D. High On−Off Conductance Switching Ratio in Optically-Driven Self-Assembled Conjugated Molecular Systems. *ACS Nano* **2010**, *4* (4), 2411–2421. https://doi.org/10.1021/nn100295x.

(19) Aravena, D.; Ruiz, E. Spin Dynamics in Single-Molecule Magnets and Molecular Qubits. *Dalton Trans.* **2020**, *49* (29), 9916–9928. https://doi.org/10.1039/D0DT01414A.

(20) Coronado, E. Molecular Magnetism: From Chemical Design to Spin Control in Molecules, Materials and Devices. *Nat Rev Mater* **2020**, *5* (2), 87–104. https://doi.org/10.1038/s41578-019-0146-8.
(21) Goodwin, C. A. P.; Ortu, F.; Reta, D.; Chilton, N. F.; Mills, D. P. Molecular Magnetic Hysteresis at 60 Kelvin in Dysprosocenium. *Nature* **2017**, *548* (7668), 439–442. https://doi.org/10.1038/nature23447.
(22) Clemente-Juan, J. M.; Coronado, E.; Gaita-Ariño, A. Magnetic Polyoxometalates: From Molecular Magnetism to Molecular Spintronics and Quantum Computing. *Chemical Society Reviews* **2012**, *41* (22), 7464. https://doi.org/10.1039/c2cs35205b.
(23) van der Molen, S.; Liljeroth, P. Charge Transport through Molecular Switches. *Journal of Physics: Condensed Matter* **2010**, *22* (13), 133001. https://doi.org/10.1088/0953-8984/22/13/133001.
(24) Fert, A.; Campbell, I. A. TRANSPORT PROPERTIES OF FERROMAGNETIC TRANSITION METALS. *J. Phys. Colloques* **1971**, *32* (C1), C1-50. https://doi.org/10.1051/jphyscol:1971109.
(25) Ghayesh, M. H.; Farajpour, A. A Review on the Mechanics of Functionally Graded Nanoscale and Microscale Structures. *Int. J. Eng. Sci.* **2019**, *137*, 8–36. https://doi.org/10.1016/j.ijengsci.2018.12.001.
(26) DeLuca, M.; Shi, Z.; Castro, C. E.; Arya, G. Dynamic DNA Nanotechnology: Toward Functional Nanoscale Devices. *Nanoscale Horiz.* **2020**, *5* (2), 182–201. https://doi.org/10.1039/c9nh00529c.
(27) Wang, L.; Zheng, M.; Xie, Z. Nanoscale Metal-Organic Frameworks for Drug Delivery: A Conventional Platform with New Promise. *J. Mat. Chem. B* **2018**, *6* (5), 707–717. https://doi.org/10.1039/c7tb02970e.
(28) Patel, N. R.; Pattni, B. S.; Abouzeid, A. H.; Torchilin, V. P. Nanopreparations to Overcome Multidrug Resistance in Cancer. *Advanced Drug Delivery Reviews* **2013**, *65* (13), 1748–1762. https://doi.org/10.1016/j.addr.2013.08.004.
(29) Wang, P.; Meyer, T. A.; Pan, V.; Dutta, P. K.; Ke, Y. The Beauty and Utility of DNA Origami. *Chem* **2017**, *2* (3), 359–382. https://doi.org/10.1016/j.chempr.2017.02.009.
(30) Lundstrom, M. Applied Physics. Moore's Law Forever? *Science* **2003**, *299* (5604), 210–211. https://doi.org/10.1126/science.1079567.
(31) Aviram, A.; Joachim, C.; Pomerantz, M. Evidence of Switching and Rectification by a Single Molecule Effected with a Scanning Tunneling Microscope. *Chemical Physics Letters* **1988**, *146* (6), 490–495. https://doi.org/10.1016/0009-2614(88)87486-4.
(32) Aguilà, D.; Prado, Y.; Koumousi, E. S.; Mathonière, C.; Clérac, R. Switchable Fe/Co Prussian Blue Networks and Molecular Analogues. *Chem. Soc. Rev.* **2016**, *45* (1), 203–224. https://doi.org/10.1039/C5CS00321K.
(33) Alemani, M.; Selvanathan, S.; Ample, F.; Peters, M. V.; Rieder, K.-H.; Moresco, F.; Joachim, C.; Hecht, S.; Grill, L. Adsorption and Switching Properties of Azobenzene Derivatives on Different Noble Metal Surfaces: Au(111), Cu(111), and Au(100). *J. Phys. Chem. C* **2008**, *112* (28), 10509–10514. https://doi.org/10.1021/jp711134p.
(34) Roth, K. M.; Dontha, N.; Dabke, R. B.; Gryko, D. T.; Clausen, C.; Lindsey, J. S.; Bocian, D. F.; Kuhr, W. G. Molecular Approach toward Information Storage Based on the Redox Properties of Porphyrins in Self-Assembled Monolayers. *Journal of Vacuum Science & Technology B: Microelectronics and Nanometer Structures* **2000**, *18* (5), 2359. https://doi.org/10.1116/1.1310657.
(35) Yi, H.; Qin, R.; Ding, S.; Wang, Y.; Li, S.; Zhao, Q.; Pan, F. Structure and Properties of Prussian Blue Analogues in Energy Storage and Conversion Applications. *Advanced Functional Materials* **2021**, *31* (6), 2006970. https://doi.org/10.1002/adfm.202006970.
(36) Chen, H.-W.; Lee, J.-H.; Lin, B.-Y.; Chen, S.; Wu, S.-T. Liquid Crystal Display and Organic Light-Emitting Diode Display: Present Status and Future Perspectives. *Light-Sci. Appl.* **2018**, *7*, 17168. https://doi.org/10.1038/lsa.2017.168.
(37) Friedlein, J. T.; McLeod, R. R.; Rivnay, J. Device Physics of Organic Electrochemical Transistors. *Org. Electron.* **2018**, *63*, 398–414. https://doi.org/10.1016/j.orgel.2018.09.010.

(38) Lu, Q.; Yang, Z.; Meng, X.; Yue, Y.; Ahmad, M. A.; Zhang, W.; Zhang, S.; Zhang, Y.; Liu, Z.; Chen, W. A Review on Encapsulation Technology from Organic Light Emitting Diodes to Organic and Perovskite Solar Cells. *Adv. Funct. Mater.* **2021**, *31* (23), 2100151. https://doi.org/10.1002/adfm.202100151.
(39) Tiwari, S.; Singh, M.; Mishra, S. K.; Shrivastava, A. K. Recent Progress in Organic Light-Emitting Diodes. *J. Nanoelectron. Optoelectron.* **2019**, *14* (9), 1215–1224. https://doi.org/10.1166/jno.2019.2632.
(40) Sun, X.; Sun, H.; Li, H.; Peng, H. Developing Polymer Composite Materials: Carbon Nanotubes or Graphene? *Adv. Mater.* **2013**, *25* (37), 5153–5176. https://doi.org/10.1002/adma.201301926.
(41) Ginley, T. P.; Wang, Y.; Law, S. Topological Insulator Film Growth by Molecular Beam Epitaxy: A Review. *Crystals* **2016**, *6* (11), 154. https://doi.org/10.3390/cryst6110154.
(42) Cheng, Y.; Wang, K.; Qi, Y.; Liu, Z. Chemical Vapor Deposition Method for Graphene Fiber Materials. *Acta Phys.-Chim. Sin.* **2022**, *38* (2), 2006046. https://doi.org/10.3866/PKU.WHXB202006046.
(43) Chovan, T.; Guttman, A. Microfabricated Devices in Biotechnology and Biochemical Processing. *Trends Biotechnol.* **2002**, *20* (3), 116–122. https://doi.org/10.1016/S0167-7799(02)01905-4.
(44) Bellizzi, G.; Bucci, O. M.; Catapano, I. Microwave Cancer Imaging Exploiting Magnetic Nanoparticles as Contrast Agent. *IEEE Trans. Biomed. Eng.* **2011**, *58* (9), 2528–2536. https://doi.org/10.1109/TBME.2011.2158544.
(45) Farokhzad, O. C.; Langer, R. Impact of Nanotechnology on Drug Delivery. *ACS Nano* **2009**, *3* (1), 16–20. https://doi.org/10.1021/nn900002m.
(46) Zang, X.; Zhou, Q.; Chang, J.; Liu, Y.; Lin, L. Graphene and Carbon Nanotube (CNT) in MEMS/NEMS Applications. *Microelectron. Eng.* **2015**, *132*, 192–206. https://doi.org/10.1016/j.mee.2014.10.023.
(47) Guo, L.; Jackman, J. A.; Yang, H.-H.; Chen, P.; Cho, N.-J.; Kim, D.-H. Strategies for Enhancing the Sensitivity of Plasmonic Nanosensors. *Nano Today* **2015**, *10* (2), 213–239. https://doi.org/10.1016/j.nantod.2015.02.007.
(48) Li, Z.; Sheng, C. Nanosensors for Food Safety. *J. Nanosci. Nanotechnol.* **2014**, *14* (1), 905–912. https://doi.org/10.1166/jnn.2014.8743.
(49) Mann, B.; Kuhn, H.; Szentpály, L. v. Tunnelling through Fatty Acid Monolayers and Its Relevance to Photographic Sensitization. *Chemical Physics Letters* **1971**, *8* (1), 82–84. https://doi.org/10.1016/0009-2614(71)80582-1.
(50) Aviram, A.; Ratner, M. A. Molecular Rectifiers. *Chemical Physics Letters* **1974**, *29* (2). https://doi.org/10.1016/0009-2614(74)85031-1.
(51) Chau, R.; Doyle, B.; Datta, S.; Kavalieros, J.; Zhang, K. Integrated Nanoelectronics for the Future. *Nature Mater* **2007**, *6* (11), 810–812. https://doi.org/10.1038/nmat2014.
(52) Vuillaume, D. Molecular Electronics: Electron, Spin and Thermal Transport through Molecules. arXiv November 20, 2021. https://doi.org/10.48550/arXiv.2111.10616.
(53) Huang, C.; Rudnev, A. V.; Hong, W.; Wandlowski, T. Break Junction under Electrochemical Gating: Testbed for Single-Molecule Electronics. *Chem. Soc. Rev.* **2015**, *44* (4), 889–901. https://doi.org/10.1039/C4CS00242C.
(54) Kim, Y.; Ang, C. H.; Ang, K.; Chang, S. W. Electromigrated Nanogaps: A Review on the Fabrications and Applications. *J. Vac. Sci. Technol. B* **2021**, *39* (1), 010802. https://doi.org/10.1116/6.0000866.
(55) Avila, A.; Bhushan, B. Electrical Measurement Techniques in Atomic Force Microscopy. *Crit. Rev. Solid State Mat. Sci.* **2010**, *35* (1), 38–51. https://doi.org/10.1080/10408430903362230.
(56) Front Matter. In *An Introduction to Ultrathin Organic Films*; Ulman, A., Ed.; Academic Press: San Diego, 1991; p iii. https://doi.org/10.1016/B978-0-08-092631-5.50001-4.
(57) Aswal, D. K.; Lenfant, S.; Guerin, D.; Yakhmi, J. V.; Vuillaume, D. Self Assembled Monolayers on Silicon for Molecular Electronics. *Analytica Chimica Acta* **2006**, *568* (1–2), 84–108. https://doi.org/10.1016/j.aca.2005.10.027.

(58) Bain, C. D.; Whitesides, G. M. Molecular-Level Control over Surface Order in Self-Assembled Monolayer Films of Thiols on Gold. *Science* **1988**, *240* (4848), 62–63. https://doi.org/10.1126/science.240.4848.62.
(59) Agraït, N. Quantum Properties of Atomic-Sized Conductors. *Physics Reports* **2003**, *377* (2–3), 81–279. https://doi.org/10.1016/S0370-1573(02)00633-6.
(60) Frontmatter. In *Electronic Materials: The Oligomer Approach*; John Wiley & Sons, Ltd, 1998; p I–XXII. https://doi.org/10.1002/9783527603220.fmatter.
(61) Kuhn, R. Synthesis of Polyenes. *J. Chem. Soc.* **1938**, No. 0, 605–614. https://doi.org/10.1039/JR9380000605.
(62) Yousef, R. I.; Mahmoud, N. F. H.; El-Hosiny, F. I.; Kühn, F. E.; Bassioni, G. Electric and Magnetic Properties of Cobalt, Copper and Nickel Organometallic Complexes for Molecular Wires. *Ain Shams Engineering Journal* **2021**, *12* (2), 2135–2144. https://doi.org/10.1016/j.asej.2020.12.002.
(63) Metzger, R. M.; Chen, B.; Höpfner, U.; Lakshmikantham, M. V.; Vuillaume, D.; Kawai, T.; Wu, X.; Tachibana, H.; Hughes, T. V.; Sakurai, H.; Baldwin, J. W.; Hosch, C.; Cava, M. P.; Brehmer, L.; Ashwell, G. J. Unimolecular Electrical Rectification in Hexadecylquinolinium Tricyanoquinodimethanide. *Journal of the American Chemical Society* **1997**, *119* (43), 10455–10466. https://doi.org/10.1021/ja971811e.
(64) Seo, K.; Konchenko, A. V.; Lee, J.; Bang, G. S.; Lee, H. Molecular Conductance Switch-On of Single Ruthenium Complex Molecules. *Journal of the American Chemical Society* **2008**, *130* (8), 2553–2559. https://doi.org/10.1021/ja077089u.
(65) Ahonen, P.; Laaksonen, T.; Schiffrin, D. J.; Kontturi, K. Photoswitching Electron Transport Properties of an Azobenzene Containing Thiol-SAM. *Physical Chemistry Chemical Physics* **2007**, *9* (35), 4898. https://doi.org/10.1039/b709025k.
(66) Aragonès, A. C.; Aravena, D.; Cerdá, J. I.; Acís-Castillo, Z.; Li, H.; Real, J. A.; Sanz, F.; Hihath, J.; Ruiz, E.; Díez-Pérez, I. Large Conductance Switching in a Single-Molecule Device through Room Temperature Spin-Dependent Transport. *Nano Letters* **2016**, *16* (1), 218–226. https://doi.org/10.1021/acs.nanolett.5b03571.
(67) McNellis, E. R.; Bronner, C.; Meyer, J.; Weinelt, M.; Tegeder, P.; Reuter, K. Azobenzene versus 3,3′,5,5′-Tetra-Tert-Butyl-Azobenzene (TBA) at Au(111): Characterizing the Role of Spacer Groups. *Phys. Chem. Chem. Phys.* **2010**, *12* (24), 6404. https://doi.org/10.1039/c001978j.
(68) Wu, S. W.; Ogawa, N.; Nazin, G. V.; Ho, W. Conductance Hysteresis and Switching in a Single-Molecule Junction. *The Journal of Physical Chemistry C* **2008**, *112* (14), 5241–5244. https://doi.org/10.1021/jp7114548.
(69) Ahonen, P.; Laaksonen, T.; Schiffrin, D. J.; Kontturi, K. Photoswitching Electron Transport Properties of an Azobenzene Containing Thiol-SAM. *Physical Chemistry Chemical Physics* **2007**, *9* (35), 4898. https://doi.org/10.1039/b709025k.
(70) Liao, J.; Agustsson, J. S.; Wu, S.; Schönenberger, C.; Calame, M.; Leroux, Y.; Mayor, M.; Jeannin, O.; Ran, Y. F.; Liu, S. X.; Decurtins, S. Cyclic Conductance Switching in Networks of Redox-Active Molecular Junctions. *Nano Letters* **2010**, *10* (3), 759–764. https://doi.org/10.1021/nl902000e.
(71) Jia, C.; Migliore, A.; Xin, N.; Huang, S.; Wang, J.; Yang, Q.; Wang, S.; Chen, H.; Wang, D.; Feng, B.; Liu, Z.; Zhang, G.; Qu, D. H.; Tian, H.; Ratner, M. A.; Xu, H. Q.; Nitzan, A.; Guo, X. Covalently Bonded Single-Molecule Junctions with Stable and Reversible Photoswitched Conductivity. *Science* **2016**, *352* (6292), 1443–1445. https://doi.org/10.1126/science.aaf6298.
(72) Tian, H.; Yang, S. Recent Progresses on Diarylethene Based Photochromic Switches. *Chemical Society Reviews* **2004**, *33* (2), 85. https://doi.org/10.1039/b302356g.
(73) Bandara, H. M. D.; Burdette, S. C. Photoisomerization in Different Classes of Azobenzene. *Chem. Soc. Rev.* **2012**, *41* (5), 1809–1825. https://doi.org/10.1039/C1CS15179G.
(74) Caillol, N.; Pijolat, M.; Siebert, E. Investigation of Chemisorbed Oxygen, Surface Segregation and Effect of Post-Treatments on La0.8Sr0.2MnO3 Powder and Screen-Printed Layers for Solid Oxide Fuel Cell Cathodes. *Applied Surface Science* **2007**, *253* (10), 4641–4648. https://doi.org/10.1016/j.apsusc.2006.10.019.

(75) Fabre, B. Functionalization of Oxide-Free Silicon Surfaces with Redox-Active Assemblies. *Chem. Rev.* **2016**, *116* (8), 4808–4849. https://doi.org/10.1021/acs.chemrev.5b00595.
(76) Bradley, K.; Gabriel, J.-C. P.; Briman, M.; Star, A.; Grüner, G. Charge Transfer from Ammonia Physisorbed on Nanotubes. *Phys. Rev. Lett.* **2003**, *91* (21), 218301. https://doi.org/10.1103/PhysRevLett.91.218301.
(77) Ishii, H.; Sugiyama, K.; Ito, E.; Seki, K. Energy Level Alignment and Interfacial Electronic Structures at Organic/Metal and Organic/Organic Interfaces. *Advanced Materials* **1999**, *11* (8), 605–625. https://doi.org/10.1002/(SICI)1521-4095(199906)11:8<605::AID-ADMA605>3.0.CO;2-Q.
(78) Crispin, X.; Geskin, V.; Crispin, A.; Cornil, J.; Lazzaroni, R.; Salaneck, W. R.; Brédas, J.-L. Characterization of the Interface Dipole at Organic/ Metal Interfaces. *J. Am. Chem. Soc.* **2002**, *124* (27), 8131–8141. https://doi.org/10.1021/ja025673r.
(79) Kahn, A.; Koch, N.; Gao, W. Electronic Structure and Electrical Properties of Interfaces between Metals and π-Conjugated Molecular Films. *Journal of Polymer Science Part B: Polymer Physics* **2003**, *41* (21), 2529–2548. https://doi.org/10.1002/polb.10642.
(80) Lennartz, M. C.; Caciuc, V.; Atodiresei, N.; Karthäuser, S.; Blügel, S. Electronic Mapping of Molecular Orbitals at the Molecule-Metal Interface. *Phys. Rev. Lett.* **2010**, *105* (6), 066801. https://doi.org/10.1103/PhysRevLett.105.066801.
(81) Casu, M. B.; Schuster, B.-E.; Biswas, I.; Raisch, C.; Marchetto, H.; Schmidt, T.; Chassé, T. Locally Resolved Core-Hole Screening, Molecular Orientation, and Morphology in Thin Films of Diindenoperylene Deposited on Au(111) Single Crystals. *Advanced Materials* **2010**, *22* (33), 3740–3744. https://doi.org/10.1002/adma.201001265.
(82) Kera, S.; Yabuuchi, Y.; Yamane, H.; Setoyama, H.; Okudaira, K. K.; Kahn, A.; Ueno, N. Impact of an Interface Dipole Layer on Molecular Level Alignment at an Organic-Conductor Interface Studied by Ultraviolet Photoemission Spectroscopy. *Phys. Rev. B* **2004**, *70* (8), 085304. https://doi.org/10.1103/PhysRevB.70.085304.
(83) Knupfer, M.; Paasch, G. Origin of the Interface Dipole at Interfaces between Undoped Organic Semiconductors and Metals. *Journal of Vacuum Science & Technology A* **2005**, *23* (4), 1072–1077. https://doi.org/10.1116/1.1885021.
(84) Dreyer, M.; Löhndorf, M.; Wadas, A.; Wiesendanger, R. Ultra-High-Vacuum Magnetic Force Microscopy of the Domain Structure of Ultra-Thin Co Films. *Applied Physics A: Materials Science & Processing* **1998**, *66*, 1209–1212. https://doi.org/10.1007/s003390051328.
(85) Glatzel, T.; Sadewasser, S.; Lux-Steiner, M. C. Amplitude or Frequency Modulation-Detection in Kelvin Probe Force Microscopy. *Applied Surface Science* **2003**, *210* (1–2), 84–89. https://doi.org/10.1016/S0169-4332(02)01484-8.
(86) Binnig, G.; Rohrer, H.; Gerber, Ch.; Weibel, E. 7x7 Reconstruction on Si(111) Resolved in Real Space. *Phys. Rev. Lett.* **1983**, *50* (2), 120–123. https://doi.org/10.1103/PhysRevLett.50.120.
(87) Takayanagi, K.; Tanishiro, Y.; Takahashi, M.; Takahashi, S. Structural Analysis of Si(111)-7×7 by UHV-transmission Electron Diffraction and Microscopy. *Journal of Vacuum Science & Technology A* **1985**, *3* (3), 1502–1506. https://doi.org/10.1116/1.573160.
(88) Main, K. H. S.; Provan, J. I.; Haynes, P. J.; Wells, G.; Hartley, J. A.; Pyne, A. L. B. Atomic Force Microscopy—A Tool for Structural and Translational DNA Research. *APL Bioengineering* **2021**, *5* (3), 031504. https://doi.org/10.1063/5.0054294.
(89) Giessibl, F. J. Atomic Resolution of the Silicon (111)-(7×7) Surface by Atomic Force Microscopy. *Science* **1995**, *267* (5194), 68–71. https://doi.org/10.1126/science.267.5194.68.
(90) Gross, L.; Mohn, F.; Moll, N.; Liljeroth, P.; Meyer, G. The Chemical Structure of a Molecule Resolved by Atomic Force Microscopy. *Science* **2009**, *325* (5944), 1110–1114. https://doi.org/10.1126/science.1176210.
(91) Esaki, L. New Phenomenon in Narrow Germanium p − n Junctions. *Phys. Rev.* **1958**, *109* (2), 603–604. https://doi.org/10.1103/PhysRev.109.603.
(92) Binnig, G.; Rohrer, H. Scanning Tunneling Microscopy—from Birth to Adolescence. *Rev. Mod. Phys.* **1987**, *59* (3), 615–625. https://doi.org/10.1103/RevModPhys.59.615.

(93) Spadafora, E. Etude par microscopie à force atomique en mode non contact et microscopie à sonde de Kelvin, de matériaux modèles pour le photovoltaïque organique. phdthesis, Université de Grenoble, 2011. https://tel.archives-ouvertes.fr/tel-00647312 (accessed 2022-10-24).
(94) Vergel, N. A. F. Dirac Antidot Superlattices for Electrons in III-V Semiconductors. phdthesis, Université de Lille, 2020. https://tel.archives-ouvertes.fr/tel-03623316 (accessed 2022-10-24).
(95) Nonot, V. Propriétés Électroniques et de Transport Des Super-Réseaux de Boites Quantiques Épitaxiallement Connectées, 2021.
(96) Israelachvili, J. N. *Intermolecular and Surface Forces*; Academic Press, 2011.
(97) Hudlet, S.; Saint Jean, M.; Guthmann, C.; Berger, J. Evaluation of the Capacitive Force between an Atomic Force Microscopy Tip and a Metallic Surface. *Eur. Phys. J. B* **1998**, *2* (1), 5–10. https://doi.org/10.1007/s100510050219.
(98) Barth, C.; Foster, A. S.; Henry, C. R.; Shluger, A. L. Recent Trends in Surface Characterization and Chemistry with High-Resolution Scanning Force Methods. *Adv. Mater.* **2011**, *23* (4), 477–501. https://doi.org/10.1002/adma.201002270.
(99) Hynninen, T.; Foster, A. S.; Barth, C. Polarized Tips or Surfaces: Consequences in Kelvin Probe Force Microscopy. *e-J. Surf. Sci. Nanotechnol.* **2011**, *9*, 6–14. https://doi.org/10.1380/ejssnt.2011.6.
(100) Giessibl, F. J. Advances in Atomic Force Microscopy. *Rev. Mod. Phys.* **2003**, *75* (3), 35.
(101) García, R. Dynamic Atomic Force Microscopy Methods. *Surface Science Reports* **2002**, *47* (6–8), 197–301. https://doi.org/10.1016/S0167-5729(02)00077-8.
(102) French, A. P. *Vibrations and Waves*; CRC Press: London, 2017. https://doi.org/10.1201/9781315273372.
(103) Albrecht, T. R.; Grütter, P.; Horne, D.; Rugar, D. Frequency Modulation Detection Using High- *Q* Cantilevers for Enhanced Force Microscope Sensitivity. *Journal of Applied Physics* **1991**, *69* (2), 668–673. https://doi.org/10.1063/1.347347.
(104) Hölscher, H.; Schwarz, U. D.; Wiesendanger, R. Calculation of the Frequency Shift in Dynamic Force Microscopy. *Applied Surface Science* **1999**, *140* (3–4), 344–351. https://doi.org/10.1016/S0169-4332(98)00552-2.
(105) Giessibl, F. J. Forces and Frequency Shifts in Atomic-Resolution Dynamic-Force Microscopy. *Phys. Rev. B* **1997**, *56* (24), 16010–16015. https://doi.org/10.1103/PhysRevB.56.16010.
(106) Gotsmann, B.; Anczykowski, B.; Seidel, C.; Fuchs, H. Determination of Tip–Sample Interaction Forces from Measured Dynamic Force Spectroscopy Curves. *Applied Surface Science* **1999**, *140* (3–4), 314–319. https://doi.org/10.1016/S0169-4332(98)00547-9.
(107) Giessibl, F. J.; Bielefeldt, H. Physical Interpretation of Frequency-Modulation Atomic Force Microscopy. *Phys. Rev. B* **2000**, *61* (15), 9968–9971. https://doi.org/10.1103/PhysRevB.61.9968.
(108) Dürig, U. Extracting Interaction Forces and Complementary Observables in Dynamic Probe Microscopy. *Appl. Phys. Lett.* **2000**, *76* (9), 1203–1205. https://doi.org/10.1063/1.125983.
(109) Torbrügge, S.; Schaff, O.; Rychen, J. Application of the KolibriSensor® to Combined Atomic-Resolution Scanning Tunneling Microscopy and Noncontact Atomic-Force Microscopy Imaging. *Journal of Vacuum Science & Technology B* **2010**, *28* (3), C4E12-C4E20. https://doi.org/10.1116/1.3430544.
(110) Sadewasser, S.; Glatzel, T. *Kelvin Probe Force Microscopy From Single Charge Detection to Device Characterization: From Single Charge Detection to Device Characterization*; 2018. https://doi.org/10.1007/978-3-319-75687-5.
(111) *Noncontact Atomic Force Microscopy*; Morita, S., Giessibl, F. J., Meyer, E., Wiesendanger, R., Eds.; NanoScience and Technology; Springer International Publishing: Cham, 2015. https://doi.org/10.1007/978-3-319-15588-3.
(112) Giessibl, F. J. The QPlus Sensor, a Powerful Core for the Atomic Force Microscope. *Review of Scientific Instruments* **2019**, *90* (1), 011101. https://doi.org/10.1063/1.5052264.
(113) Giessibl, F. J.; Pielmeier, F.; Eguchi, T.; An, T.; Hasegawa, Y. Comparison of Force Sensors for Atomic Force Microscopy Based on Quartz Tuning Forks and Length-Extensional Resonators. *Phys. Rev. B* **2011**, *84* (12), 125409. https://doi.org/10.1103/PhysRevB.84.125409.

(114) Gysin, U.; Rast, S.; Ruff, P.; Meyer, E.; Lee, D. W.; Vettiger, P.; Gerber, C. Temperature Dependence of the Force Sensitivity of Silicon Cantilevers. *Phys. Rev. B* **2004**, *69* (4), 045403. https://doi.org/10.1103/PhysRevB.69.045403.
(115) Lübbe, J.; Temmen, M.; Rode, S.; Rahe, P.; Kühnle, A.; Reichling, M. Thermal Noise Limit for Ultra-High Vacuum Noncontact Atomic Force Microscopy. *Beilstein J. Nanotechnol.* **2013**, *4*, 32–44. https://doi.org/10.3762/bjnano.4.4.
(116) Kobayashi, K.; Yamada, H.; Matsushige, K. Frequency Noise in Frequency Modulation Atomic Force Microscopy. *Review of Scientific Instruments* **2009**, *80* (4), 043708. https://doi.org/10.1063/1.3120913.
(117) Hasegawa, Y.; Eguchi, T.; An, T.; Ono, M.; Akiyama, K.; Sakurai, T. Calculation of Noise Intensity in the Frequency Demodulation for Atomic Force Microscopy. *Jpn. J. Appl. Phys.* **2004**, *43* (No. 2B), L303–L305. https://doi.org/10.1143/JJAP.43.L303.
(118) Pielmeier, F.; Meuer, D.; Schmid, D.; Strunk, C.; Giessibl, F. J. Impact of Thermal Frequency Drift on Highest Precision Force Microscopy Using Quartz-Based Force Sensors at Low Temperatures. *Beilstein J. Nanotechnol.* **2014**, *5*, 407–412. https://doi.org/10.3762/bjnano.5.48.
(119) Hutter, J. L.; Bechhoefer, J. Calibration of Atomic-force Microscope Tips. *Review of Scientific Instruments* **1993**, *64* (7), 1868–1873. https://doi.org/10.1063/1.1143970.
(120) El-Batanouny, M.; Burdick, S.; Martini, K. M.; Stancioff, P. Double-Sine-Gordon Solitons: A Model for Misfit Dislocations on the Au(111) Reconstructed Surface. *Phys. Rev. Lett.* **1987**, *58* (26), 2762–2765. https://doi.org/10.1103/PhysRevLett.58.2762.
(121) Takeuchi, N.; Chan, C. T.; Ho, K. M. Au(111): A Theoretical Study of the Surface Reconstruction and the Surface Electronic Structure. *Phys. Rev. B* **1991**, *43* (17), 13899–13906. https://doi.org/10.1103/PhysRevB.43.13899.
(122) Tanaka, K. Surface Nano-Structuring by Adsorption and Chemical Reactions. *Materials* **2010**, *3* (9), 4518–4549. https://doi.org/10.3390/ma3094518.
(123) Xu, J.; Wu, Y.; Li, W.; Xu, J. Surface Potential Modeling and Reconstruction in Kelvin Probe Force Microscopy. *Nanotechnology* **2017**, *28* (36), 365705. https://doi.org/10.1088/1361-6528/aa7cbc.
(124) Mélin, T.; Diesinger, H.; Deresmes, D.; Stiévenard, D. Probing Nanoscale Dipole-Dipole Interactions by Electric Force Microscopy. *Phys. Rev. Lett.* **2004**, *92* (16), 166101. https://doi.org/10.1103/PhysRevLett.92.166101.
(125) Glatzel, Th. Measuring Atomic-Scale Variations of the Electrostatic Force. In *Kelvin Probe Force Microscopy: Measuring and Compensating Electrostatic Forces*; Sadewasser, S., Glatzel, T., Eds.; Springer Series in Surface Sciences; Springer: Berlin, Heidelberg, 2012; pp 289–327. https://doi.org/10.1007/978-3-642-22566-6_13.
(126) Bocquet, F.; Nony, L.; Loppacher, C. Polarization Effects in Noncontact Atomic Force Microscopy: A Key to Model the Tip-Sample Interaction above Charged Adatoms. *Phys. Rev. B* **2011**, *83* (3), 035411. https://doi.org/10.1103/PhysRevB.83.035411.
(127) Burke, S. A.; LeDue, J. M.; Miyahara, Y.; Topple, J. M.; Fostner, S.; Grütter, P. Determination of the Local Contact Potential Difference of PTCDA on NaCl: A Comparison of Techniques. *Nanotechnology* **2009**, *20* (26), 264012. https://doi.org/10.1088/0957-4484/20/26/264012.
(128) Wandelt, K. The Local Work Function: Concept and Implications. *Applied Surface Science* **1997**, *111*, 1–10. https://doi.org/10.1016/S0169-4332(96)00692-7.
(129) Turek, N.; Godey, S.; Deresmes, D.; Mélin, T. Ring Charging of a Single Silicon Dangling Bond Imaged by Noncontact Atomic Force Microscopy. *Phys. Rev. B* **2020**, *102* (23), 235433. https://doi.org/10.1103/PhysRevB.102.235433.
(130) Huang, Y.; Ren, S. Multifunctional Prussian Blue Analogue Magnets: Emerging Opportunities. *Applied Materials Today* **2021**, *22*, 100886. https://doi.org/10.1016/j.apmt.2020.100886.
(131) Reguera, L.; Krap, C. P.; Balmaseda, J.; Reguera, E. Hydrogen Storage in Copper Prussian Blue Analogues: Evidence of H2 Coordination to the Copper Atom. *J. Phys. Chem. C* **2008**, *112* (40), 15893–15899. https://doi.org/10.1021/jp803714j.

(132) Kaye, S. S.; Long, J. R. Hydrogen Storage in the Dehydrated Prussian Blue Analogues M3[Co(CN)6]2 (M = Mn, Fe, Co, Ni, Cu, Zn). *J. Am. Chem. Soc.* **2005**, *127* (18), 6506–6507. https://doi.org/10.1021/ja051168t.
(133) Chapman, K. W.; Southon, P. D.; Weeks, C. L.; Kepert, C. J. Reversible Hydrogen Gas Uptake in Nanoporous Prussian Blue Analogues. *Chem. Commun.* **2005**, No. 26, 3322–3324. https://doi.org/10.1039/B502850G.
(134) Kamachi, Y.; Zakaria, M. B.; Torad, N. L.; Nakato, T.; Ahamad, T.; Alshehri, S. M.; Malgras, V.; Yamauchi, Y. Hydrogels Containing Prussian Blue Nanoparticles Toward Removal of Radioactive Cesium Ions. *j nanosci nanotechnol* **2016**, *16* (4), 4200–4204. https://doi.org/10.1166/jnn.2016.12607.
(135) Lee, K.-M.; Kawamoto, T.; Minami, K.; Takahashi, A.; Parajuli, D.; Kido, G.; Yoshino, K.; Tanaka, H. Improved Adsorption Properties of Granulated Copper Hexacyanoferrate with Multi-Scale Porous Networks. *RSC Adv.* **2016**, *6* (20), 16234–16238. https://doi.org/10.1039/C5RA25388H.
(136) Yi, H.; Qin, R.; Ding, S.; Wang, Y.; Li, S.; Zhao, Q.; Pan, F. Structure and Properties of Prussian Blue Analogues in Energy Storage and Conversion Applications. *Adv. Funct. Mater.* **2021**, *31* (6), 2006970. https://doi.org/10.1002/adfm.202006970.
(137) Qian, J.; Wu, C.; Cao, Y.; Ma, Z.; Huang, Y.; Ai, X.; Yang, H. Prussian Blue Cathode Materials for Sodium-Ion Batteries and Other Ion Batteries. *Advanced Energy Materials* **2018**, *8* (17), 1702619. https://doi.org/10.1002/aenm.201702619.
(138) Xu, Y.; Zheng, S.; Tang, H.; Guo, X.; Xue, H.; Pang, H. Prussian Blue and Its Derivatives as Electrode Materials for Electrochemical Energy Storage. *Energy Storage Materials* **2017**, *9*, 11–30. https://doi.org/10.1016/j.ensm.2017.06.002.
(139) Tannous, C.; Comstock, R. L. Magnetic Information-Storage Materials. In *Springer Handbook of Electronic and Photonic Materials*; Kasap, S., Capper, P., Eds.; Springer Handbooks; Springer International Publishing: Cham, 2017; pp 1–1. https://doi.org/10.1007/978-3-319-48933-9_49.
(140) Keggin, J. F.; Miles, F. D. Structures and Formulæ of the Prussian Blues and Related Compounds. *Nature* **1936**, *137* (3466), 577–578. https://doi.org/10.1038/137577a0.
(141) Shriver, D. F.; Brown, D. B. Environment of Interstitial Ions in a Prussian Blue Analog, Co3[Co(CN)6]2. *Inorg. Chem.* **1969**, *8* (1), 42–46. https://doi.org/10.1021/ic50071a010.
(142) Brown, D. B.; Shriver, D. F. Structures and Solid-State Reactions of Prussian Blue Analogs Containing Chromium, Manganese, Iron, and Cobalt. *Inorg. Chem.* **1969**, *8* (1), 37–42. https://doi.org/10.1021/ic50071a009.
(143) Aguilà, D.; Prado, Y.; Koumousi, E. S.; Mathonière, C.; Clérac, R. Switchable Fe/Co Prussian Blue Networks and Molecular Analogues. *Chem. Soc. Rev.* **2016**, *45* (1), 203–224. https://doi.org/10.1039/C5CS00321K.
(144) Trinh, L.; Zerdane, S.; Mazérat, S.; Dia, N.; Dragoe, D.; Herrero, C.; Rivière, E.; Catala, L.; Cammarata, M.; Collet, E.; Mallah, T. Photoswitchable 11 Nm CsCoFe Prussian Blue Analogue Nanocrystals with High Relaxation Temperature. *Inorg. Chem.* **2020**, *59* (18), 13153–13161. https://doi.org/10.1021/acs.inorgchem.0c01432.
(145) Dunbar, K. R.; Heintz, R. A. Chemistry of Transition Metal Cyanide Compounds: Modern Perspectives. In *Progress in Inorganic Chemistry*; Karlin, K. D., Ed.; John Wiley & Sons, Inc.: Hoboken, NJ, USA, 2007; pp 283–391. https://doi.org/10.1002/9780470166468.ch4.
(146) Prado, Y.; Arrio, M.-A.; Volatron, F.; Otero, E.; Cartier dit Moulin, C.; Sainctavit, P.; Catala, L.; Mallah, T. Magnetic Anisotropy of Cyanide-Bridged Core and Core-Shell Coordination Nanoparticles Probed by X-Ray Magnetic Circular Dichroism. *Chem. Eur. J.* **2013**, *19* (21), 6685–6694. https://doi.org/10.1002/chem.201203609.
(147) Wheeler, S. Prussian Blue Analogue Materials for Energy Storage Applications. http://purl.org/dc/dcmitype/Text, University of Oxford, 2022. https://ora.ox.ac.uk/objects/uuid:74850228-7f91-4d3d-bc2c-8f743b1feb99 (accessed 2022-10-07).

(148) Azhar, A.; Li, Y.; Cai, Z.; Zakaria, M. B.; Masud, M. K.; Hossain, Md. S. A.; Kim, J.; Zhang, W.; Na, J.; Yamauchi, Y.; Hu, M. Nanoarchitectonics: A New Materials Horizon for Prussian Blue and Its Analogues. *BCSJ* **2019**, *92* (4), 875–904. https://doi.org/10.1246/bcsj.20180368.
(149) Hurlbutt, K.; Wheeler, S.; Capone, I.; Pasta, M. Prussian Blue Analogs as Battery Materials. *Joule* **2018**, *2* (10), 1950–1960. https://doi.org/10.1016/j.joule.2018.07.017.
(150) *25.5: Bonding in Coordinate Compounds*. Chemistry LibreTexts. https://chem.libretexts.org/Bookshelves/General_Chemistry/Map%3A_A_Molecular_Approach_(Tro)/25%3A_Transition_Metals_and_Coordination_Compounds/25.05%3A_Bonding_in_Coordinate_Compounds (accessed 2022-05-20).
(151) Brinzei, D.; Catala, L.; Louvain, N.; Rogez, G.; Stéphan, O.; Gloter, A.; Mallah, T. Spontaneous Stabilization and Isolation of Dispersible Bimetallic Coordination Nanoparticles of CsxNi[Cr(CN)6]y. *J. Mater. Chem.* **2006**, *16* (26), 2593–2599. https://doi.org/10.1039/B605221E.
(152) Sato, O.; Iyoda, T.; Fujishima, A.; Hashimoto, K. Photoinduced Magnetization of a Cobalt-Iron Cyanide. *Science* **1996**, *272* (5262), 704–705. https://doi.org/10.1126/science.272.5262.704.
(153) Cammarata, M.; Zerdane, S.; Balducci, L.; Azzolina, G.; Mazerat, S.; Exertier, C.; Trabuco, M.; Levantino, M.; Alonso-Mori, R.; Glownia, J. M.; Song, S.; Catala, L.; Mallah, T.; Matar, S. F.; Collet, E. Charge Transfer Driven by Ultrafast Spin Transition in a CoFe Prussian Blue Analogue. *Nat. Chem.* **2021**, *13* (1), 10–14. https://doi.org/10.1038/s41557-020-00597-8.
(154) Zerdane, S.; Cammarata, M.; Balducci, L.; Bertoni, R.; Catala, L.; Mazerat, S.; Mallah, T.; Pedersen, M. N.; Wulff, M.; Nakagawa, K.; Tokoro, H.; Ohkoshi, S.; Collet, E. Probing Transient Photoinduced Charge Transfer in Prussian Blue Analogues with Time-Resolved XANES and Optical Spectroscopy. *European Journal of Inorganic Chemistry* **2018**, *2018* (3–4), 272–277. https://doi.org/10.1002/ejic.201700657.
(155) Sato, O. Optically Switchable Molecular Solids: Photoinduced Spin-Crossover, Photochromism, and Photoinduced Magnetization. *Acc. Chem. Res.* **2003**, *36* (9), 692–700. https://doi.org/10.1021/ar020242z.
(156) Verdaguer, M. Molecular Electronics Emerges from Molecular Magnetism. *Science* **1996**, *272* (5262), 698–699. https://doi.org/10.1126/science.272.5262.698.
(157) Ohkoshi, S.; Hashimoto, K. Photo-Magnetic and Magneto-Optical Effects of Functionalized Metal Polycyanides. *Journal of Photochemistry and Photobiology C: Photochemistry Reviews* **2001**, *2* (1), 71–88. https://doi.org/10.1016/S1389-5567(01)00011-9.
(158) Pejaković, D. A.; Manson, J. L.; Miller, J. S.; Epstein, A. J. Photoinduced Magnetism, Dynamics, and Cluster Glass Behavior of a Molecule-Based Magnet. *Phys. Rev. Lett.* **2000**, *85* (9), 1994–1997. https://doi.org/10.1103/PhysRevLett.85.1994.
(159) Shimamoto, N.; Ohkoshi, S.; Sato, O.; Hashimoto, K. One-Shot-Laser-Pulse-Induced Cooperative Charge Transfer Accompanied by Spin Transition in a Co-Fe Prussian Blue Analog at Room Temperature. *Chem. Lett.* **2002**, *31* (4), 486–487. https://doi.org/10.1246/cl.2002.486.
(160) Zimbovskaya, N. A.; Pederson, M. R. Electron Transport through Molecular Junctions. *Physics Reports* **2011**, *509* (1), 1–87. https://doi.org/10.1016/j.physrep.2011.08.002.
(161) Cuevas, J. C.; Scheer, E. *Molecular Electronics: An Introduction to Theory and Experiment*; WORLD SCIENTIFIC, 2010. https://doi.org/10.1142/7434.
(162) Galperin, M.; Nitzan, A.; Ratner, M. A. Molecular Transport Junctions: Current from Electronic Excitations in the Leads. *Phys. Rev. Lett.* **2006**, *96* (16), 166803. https://doi.org/10.1103/PhysRevLett.96.166803.
(163) Araidai, M.; Tsukada, M. Theoretical Calculations of Electron Transport in Molecular Junctions: Inflection Behavior in Fowler-Nordheim Plot and Its Origin. *Physical Review B* **2010**, *81* (23), 235114. https://doi.org/10.1103/PhysRevB.81.235114.
(164) Nitzan, A. Electron Transmission through Molecules and Molecular Interfaces. *Annu. Rev. Phys. Chem.* **2001**, *52* (1), 681–750. https://doi.org/10.1146/annurev.physchem.52.1.681.
(165) Chen, X.; Roemer, M.; Yuan, L.; Du, W.; Thompson, D.; del Barco, E.; Nijhuis, C. A. Molecular Diodes with Rectification Ratios Exceeding 105 Driven by Electrostatic Interactions. *Nature Nanotech* **2017**, *12* (8), 797–803. https://doi.org/10.1038/nnano.2017.110.

(166) Brunner, J. G. Gaining Microscopic Insight into Molecular Junctions by Transport Experiments. Thesis, University_of_Basel, 2013. https://doi.org/10.5451/unibas-006119305.
(167) Shah, M.; Sayyad, M. H.; Karimov, Kh. S.; Maroof-Tahir, M. Investigation of the Electrical Properties of a Surface-Type Al/NiPc/Ag Schottky Diode Using I–V and C–V Characteristics. *Physica B: Condensed Matter* **2010**, *405* (4), 1188–1192. https://doi.org/10.1016/j.physb.2009.11.034.
(168) Yahia, I. S.; Zahran, H. Y.; Alamri, F. H.; Aslam Manthrammel, M.; AlFaify, S.; Ali, A. M. Microelectronic Properties of the Organic Schottky Diode with Pyronin-Y: Admittance Spectroscopy, and Negative Capacitance. *Physica B: Condensed Matter* **2018**, *543*, 46–53. https://doi.org/10.1016/j.physb.2018.05.011.
(169) Song, Y.; Li, X.; Mackin, C.; Zhang, X.; Fang, W.; Palacios, T.; Zhu, H.; Kong, J. Role of Interfacial Oxide in High-Efficiency Graphene–Silicon Schottky Barrier Solar Cells. *Nano Lett.* **2015**, *15* (3), 2104–2110. https://doi.org/10.1021/nl505011f.
(170) Bartolomeo, A. D.; Giubileo, F.; Luongo, G.; Iemmo, L.; Martucciello, N.; Niu, G.; Fraschke, M.; Skibitzki, O.; Schroeder, T.; Lupina, G. Tunable Schottky Barrier and High Responsivity in Graphene/Si-Nanotip Optoelectronic Device. *2D Mater.* **2016**, *4* (1), 015024. https://doi.org/10.1088/2053-1583/4/1/015024.
(171) Grillo, A.; Di Bartolomeo, A. A Current–Voltage Model for Double Schottky Barrier Devices. *Adv. Electron. Mater.* **2021**, *7* (2), 2000979. https://doi.org/10.1002/aelm.202000979.
(172) Bonnet, R.; Lenfant, S.; Mazérat, S.; Mallah, T.; Vuillaume, D. Long-Range Electron Transport in Prussian Blue Analog Nanocrystals. *Nanoscale* **2020**, *12* (39), 20374–20385. https://doi.org/10.1039/D0NR06971J.
(173) Johnson, K. L. *Contact Mechanics*; Cambridge University Press: Cambridge, 1985. https://doi.org/10.1017/CBO9781139171731.
(174) Félix, G.; Mikolasek, M.; Shepherd, H. J.; Long, J.; Larionova, J.; Guari, Y.; Itié, J.-P.; Chumakov, A. I.; Nicolazzi, W.; Molnár, G.; Bousseksou, A. Elasticity of Prussian-Blue-Analogue Nanoparticles. *European Journal of Inorganic Chemistry* **2018**, *2018* (3–4), 443–448. https://doi.org/10.1002/ejic.201700796.
(175) Watanabe, S.; Sawada, Y.; Nakaya, M.; Yoshino, M.; Nagasaki, T.; Kameyama, T.; Torimoto, T.; Inaba, Y.; Takahashi, H.; Takeshita, K.; Onoe, J. Intra- and Inter-Atomic Optical Transitions of Fe, Co, and Ni Ferrocyanides Studied Using First-Principles Many-Electron Calculations. *Journal of Applied Physics* **2016**, *119* (23), 235102. https://doi.org/10.1063/1.4954070.
(176) Shen, S.; Bottomley, L. A. Microcantilever Sensing of Particles in Liquid Streams: Thin-Film Coating Impacts Sensor Performance. In *Thin Films: Preparation, Characterization, Applications*; Soriaga, M. P., Stickney, J., Bottomley, L. A., Kim, Y.-G., Eds.; Springer US: Boston, MA, 2002; pp 349–359. https://doi.org/10.1007/978-1-4615-0775-8_27.
(177) Müllegger, S.; Rashidi, M.; Mayr, K.; Fattinger, M.; Ney, A.; Koch, R. Radio-Wave Oscillations of Molecular-Chain Resonators. *Phys. Rev. Lett.* **2014**, *112* (11), 117201. https://doi.org/10.1103/PhysRevLett.112.117201.
(178) Costello, B. J.; Wenzel, S. W.; White, R. M. Acoustic Chemical Sensors. *Science* **1991**, *251* (4999), 1372. https://doi.org/10.1126/science.251.4999.1372.
(179) Gupta, A.; Akin, D.; Bashir, R. Single Virus Particle Mass Detection Using Microresonators with Nanoscale Thickness. *Appl. Phys. Lett.* **2004**, *84* (11), 1976–1978. https://doi.org/10.1063/1.1667011.
(180) Yang, Y. T.; Callegari, C.; Feng, X. L.; Ekinci, K. L.; Roukes, M. L. Zeptogram-Scale Nanomechanical Mass Sensing. *Nano Lett.* **2006**, *6* (4), 583–586. https://doi.org/10.1021/nl052134m.
(181) Sáenz, J. J.; García, N.; Grütter, P.; Meyer, E.; Heinzelmann, H.; Wiesendanger, R.; Rosenthaler, L.; Hidber, H. R.; Güntherodt, H. -J. Observation of Magnetic Forces by the Atomic Force Microscope. *Journal of Applied Physics* **1987**, *62* (10), 4293–4295. https://doi.org/10.1063/1.339105.

(182) Bocko, M. F.; Onofrio, R. On the Measurement of a Weak Classical Force Coupled to a Harmonic Oscillator: Experimental Progress. *Rev. Mod. Phys.* **1996**, *68* (3), 755–799. https://doi.org/10.1103/RevModPhys.68.755.
(183) Rugar, D.; Budakian, R.; Mamin, H. J.; Chui, B. W. Single Spin Detection by Magnetic Resonance Force Microscopy. *Nature* **2004**, *430* (6997), 329–332. https://doi.org/10.1038/nature02658.
(184) Blencowe, M. Quantum Electromechanical Systems. *Phys. Rep.-Rev. Sec. Phys. Lett.* **2004**, *395* (3), 159–222. https://doi.org/10.1016/j.physrep.2003.12.005.
(185) Brown, K. R.; Ospelkaus, C.; Colombe, Y.; Wilson, A. C.; Leibfried, D.; Wineland, D. J. Coupled Quantized Mechanical Oscillators. *Nature* **2011**, *471* (7337), 196–199. https://doi.org/10.1038/nature09721.
(186) Chan, J.; Alegre, T. P. M.; Safavi-Naeini, A. H.; Hill, J. T.; Krause, A.; Gröblacher, S.; Aspelmeyer, M.; Painter, O. Laser Cooling of a Nanomechanical Oscillator into Its Quantum Ground State. *Nature* **2011**, *478* (7367), 89–92. https://doi.org/10.1038/nature10461.
(187) Müllegger, S.; Rashidi, M.; Fattinger, M.; Koch, R. Interactions and Self-Assembly of Stable Hydrocarbon Radicals on a Metal Support. *J. Phys. Chem. C* **2012**, *116* (42), 22587–22594. https://doi.org/10.1021/jp3068409.
(188) Neier, E.; Arias Ugarte, R.; Rady, N.; Venkatesan, S.; Hudnall, T. W.; Zakhidov, A. Solution-Processed Organic Light-Emitting Diodes with Emission from a Doublet Exciton; Using (2,4,6-Trichlorophenyl)Methyl as Emitter. *Organic Electronics* **2017**, *44*, 126–131. https://doi.org/10.1016/j.orgel.2017.02.010.
(189) Obolda, A.; Ai, X.; Zhang, M.; Li, F. Up to 100% Formation Ratio of Doublet Exciton in Deep-Red Organic Light-Emitting Diodes Based on Neutral π-Radical. *ACS Appl. Mater. Interfaces* **2016**, *8* (51), 35472–35478. https://doi.org/10.1021/acsami.6b12338.
(190) Hicks, R. G. What's New in Stable Radical Chemistry? *Org. Biomol. Chem.* **2006**, *5* (9), 1321–1338. https://doi.org/10.1039/B617142G.
(191) Müllegger, S.; Das, A. K.; Mayr, K.; Koch, R. Radio-Frequency Excitation of Single Molecules by Scanning Tunnelling Microscopy. *Nanotechnology* **2014**, *25* (13), 135705. https://doi.org/10.1088/0957-4484/25/13/135705.
(192) Müllegger, S.; Tebi, S.; Das, A. K.; Schöfberger, W.; Faschinger, F.; Koch, R. Radio Frequency Scanning Tunneling Spectroscopy for Single-Molecule Spin Resonance. *Phys. Rev. Lett.* **2014**, *113* (13), 133001. https://doi.org/10.1103/PhysRevLett.113.133001.
(193) Ghasemi, S.; Moth-Poulsen, K. Single Molecule Electronic Devices with Carbon-Based Materials: Status and Opportunity. *Nanoscale* **2021**, *13* (2), 659–671. https://doi.org/10.1039/D0NR07844A.
(194) Koelsch, C. F. *SYNTHESES WITH TRIARYLVINYLMAGNESIUM BROMIDES. PENTAARYLALLYL ALCOHOLS*. ACS Publications. https://doi.org/10.1021/ja01347a057.
(195) Koelsch, C. F. *Syntheses with Triarylvinylmagnesium Bromides. α,γ-Bisdiphenylene-β-phenylallyl, a Stable Free Radical*. ACS Publications. https://doi.org/10.1021/ja01573a053.
(196) Tian, Y.; Uchida, K.; Kurata, H.; Hirao, Y.; Nishiuchi, T.; Kubo, T. Design and Synthesis of New Stable Fluorenyl-Based Radicals. *J. Am. Chem. Soc.* **2014**, *136* (36), 12784–12793. https://doi.org/10.1021/ja507005c.
(197) Dane, E. L.; Maly, T.; Debelouchina, G. T.; Griffin, R. G.; Swager, T. M. Synthesis of a BDPA-TEMPO Biradical. *Org. Lett.* **2009**, *11* (9), 1871–1874. https://doi.org/10.1021/ol9001575.
(198) Steurer, W.; Repp, J.; Gross, L.; Scivetti, I.; Persson, M.; Meyer, G. Manipulation of the Charge State of Single Au Atoms on Insulating Multilayer Films. *Phys. Rev. Lett.* **2015**, *114* (3), 036801. https://doi.org/10.1103/PhysRevLett.114.036801.
(199) Ardhuin, T.; Guillermet, O.; Gourdon, A.; Gauthier, S. Measurement and Control of the Charge Occupation of Single Adsorbed Molecules Levels by STM and Nc-AFM. *The Journal of Physical Chemistry C* **2019**. https://doi.org/10.1021/acs.jpcc.9b05687.
(200) Weymouth, A. J.; Wutscher, T.; Welker, J.; Hofmann, T.; Giessibl, F. J. Phantom Force Induced by Tunneling Current: A Characterization on Si(111). *Phys. Rev. Lett.* **2011**, *106* (22), 226801. https://doi.org/10.1103/PhysRevLett.106.226801.

(201) Wutscher, T.; Weymouth, A. J.; Giessibl, F. J. Localization of the Phantom Force Induced by the Tunneling Current. *Phys. Rev. B* **2012**, *85* (19), 195426. https://doi.org/10.1103/PhysRevB.85.195426.
(202) Berner, S.; de Wild, M.; Ramoino, L.; Ivan, S.; Baratoff, A.; Güntherodt, H.-J.; Suzuki, H.; Schlettwein, D.; Jung, T. A. Adsorption and Two-Dimensional Phases of a Large Polar Molecule: Sub-Phthalocyanine on Ag(111). *Phys. Rev. B* **2003**, *68* (11), 115410. https://doi.org/10.1103/PhysRevB.68.115410.
(203) Theobald, J. A.; Oxtoby, N. S.; Phillips, M. A.; Champness, N. R.; Beton, P. H. Controlling Molecular Deposition and Layer Structure with Supramolecular Surface Assemblies. *Nature* **2003**, *424* (6952), 1029–1031. https://doi.org/10.1038/nature01915.
(204) Böhringer, M.; Morgenstern, K.; Schneider, W.-D.; Berndt, R.; Mauri, F.; De Vita, A.; Car, R. Two-Dimensional Self-Assembly of Supramolecular Clusters and Chains. *Phys. Rev. Lett.* **1999**, *83* (2), 324–327. https://doi.org/10.1103/PhysRevLett.83.324.
(205) McNellis, E. R.; Bronner, C.; Meyer, J.; Weinelt, M.; Tegeder, P.; Reuter, K. Azobenzene versus 3,3′,5,5′-Tetra-Tert-Butyl-Azobenzene (TBA) at Au(111): Characterizing the Role of Spacer Groups. *Phys. Chem. Chem. Phys.* **2010**, *12* (24), 6404. https://doi.org/10.1039/c001978j.
(206) Jung, T. A.; Schlittler, R. R.; Gimzewski, J. K. Conformational Identification of Individual Adsorbed Molecules with the STM. *Nature* **1997**, *386* (6626), 696–698. https://doi.org/10.1038/386696a0.
(207) Schunack, M.; Rosei, F.; Naitoh, Y.; Jiang, P.; Gourdon, A.; Lægsgaard, E.; Stensgaard, I.; Joachim, C.; Besenbacher, F. Adsorption Behavior of Lander Molecules on Cu(110) Studied by Scanning Tunneling Microscopy. *The Journal of Chemical Physics* **2002**, *117* (13), 6259–6265. https://doi.org/10.1063/1.1498475.
(208) Kawai, S. H.; Gilat, S. L.; Ponsinet, R.; Lehn, J.-M. A Dual-Mode Molecular Switching Device: Bisphenolic Diarylethenes with Integrated Photochromic and Electrochromic Properties. *Chemistry – A European Journal* **1995**, *1* (5), 285–293. https://doi.org/10.1002/chem.19950010505.
(209) Shimizu, T. K.; Jung, J.; Imada, H.; Kim, Y. Adsorption-Induced Stability Reversal of Photochromic Diarylethene on Metal Surfaces. *Chemical Communications* **2013**, *49* (77), 8710. https://doi.org/10.1039/c3cc44002h.
(210) Li, J.; Speyer, G.; Sankey, O. F. Conduction Switching of Photochromic Molecules. *Physical Review Letters* **2004**, *93* (24). https://doi.org/10.1103/PhysRevLett.93.248302.
(211) Comstock, M. J.; Strubbe, D. A.; Berbil-Bautista, L.; Levy, N.; Cho, J.; Poulsen, D.; Fréchet, J. M. J.; Louie, S. G.; Crommie, M. F. Determination of Photoswitching Dynamics through Chiral Mapping of Single Molecules Using a Scanning Tunneling Microscope. *Physical Review Letters* **2010**, *104* (17), 178301. https://doi.org/10.1103/PhysRevLett.104.178301.
(212) Nie, S.; Emory, S. R. Probing Single Molecules and Single Nanoparticles by Surface-Enhanced Raman Scattering. *Science* **1997**, *275* (5303), 1102–1106. https://doi.org/10.1126/science.275.5303.1102.
(213) Klajn, R. Immobilized Azobenzenes for the Construction of Photoresponsive Materials. *Pure and Applied Chemistry* **2010**, *82* (12), 2247–2279. https://doi.org/10.1351/PAC-CON-10-09-04.
(214) Zeng, J.; Chen, K. Q.; Deng, X.; Long, M. Light-Driven Strong Spin Valve Effects in an Azobenzene-Based Spin Optoelectronic Device. *Journal of Physics D: Applied Physics* **2016**, *49* (41), 415104. https://doi.org/10.1088/0022-3727/49/41/415104.
(215) Yu, Y.; Nakano, M.; Ikeda, T. Directed Bending of a Polymer Film by Light. *Nature* **2003**, *425* (6954), 145–145. https://doi.org/10.1038/425145a.
(216) Liu, Z. F.; Hashimoto, K.; Fujishima, A. Photoelectrochemical Information Storage Using an Azobenzene Derivative. *Nature* **1990**, *347* (6294), 658–660. https://doi.org/10.1038/347658a0.
(217) Ikeda, T.; Tsutsumi, O. Optical Switching and Image Storage by Means of Azobenzene Liquid-Crystal Films. *Science* **1995**, *268* (5219), 1873–1875. https://doi.org/10.1126/science.268.5219.1873.
(218) Dri, C.; Peters, M. V.; Schwarz, J.; Hecht, S.; Grill, L. Spatial Periodicity in Molecular Switching. *Nature Nanotech* **2008**, *3* (11), 649–653. https://doi.org/10.1038/nnano.2008.269.

(219) Alemani, M.; Peters, M. V.; Hecht, S.; Rieder, K.-H.; Moresco, F.; Grill, L. Electric Field-Induced Isomerization of Azobenzene by STM. *Journal of the American Chemical Society* **2006**, *128* (45), 14446–14447. https://doi.org/10.1021/ja065449s.
(220) Yasuda, S.; Nakamura, T.; Matsumoto, M.; Shigekawa, H. Phase Switching of a Single Isomeric Molecule and Associated Characteristic Rectification. *Journal of the American Chemical Society* **2003**, *125* (52), 16430–16433. https://doi.org/10.1021/ja038233o.
(221) Alemani, M.; Selvanathan, S.; Ample, F.; Peters, M. V.; Rieder, K.-H.; Moresco, F.; Joachim, C.; Hecht, S.; Grill, L. Adsorption and Switching Properties of Azobenzene Derivatives on Different Noble Metal Surfaces: Au(111), Cu(111), and Au(100). *The Journal of Physical Chemistry C* **2008**, *112* (28), 10509–10514. https://doi.org/10.1021/jp711134p.
(222) Wolf, M.; Tegeder, P. Reversible Molecular Switching at a Metal Surface: A Case Study of Tetra-Tert-Butyl-Azobenzene on Au(111). *Surface Science* **2009**, *603* (10–12), 1506–1517. https://doi.org/10.1016/j.susc.2008.11.049.
(223) Biswas, N.; Umapathy, S. Density Functional Calculations of Structures, Vibrational Frequencies, and Normal Modes of Trans- and Cis-Azobenzene. *J. Phys. Chem. A* **1997**, *101* (30), 5555–5566. https://doi.org/10.1021/jp970312x.
(224) Kurita, N.; Ikegami, T.; Ishikawa, Y. Ab Initio Study of the Minimum-Energy Structure of Trans-Azobenzene. *Chemical Physics Letters* **2002**, *360* (3), 349–354. https://doi.org/10.1016/S0009-2614(02)00854-0.
(225) Tylkowski, B.; Jastrząb, R.; Skrobańska, M. Photo-Sensitive Complexes Based on Azobenzene. *Physical Sciences Reviews* **2016**, *1* (4). https://doi.org/10.1515/psr-2016-0002.
(226) Talaty, E. R.; Fargo, J. C. Thermal Cis–Trans-Isomerization of Substituted Azobenzenes: A Correction of the Literature. *Chem. Commun. (London)* **1967**, No. 2, 65–66. https://doi.org/10.1039/C19670000065.
(227) Maurer, R. J.; Reuter, K. Bistability Loss as a Key Feature in Azobenzene (Non-)Switching on Metal Surfaces. *Angewandte Chemie International Edition* **2012**, *51* (48), 12009–12011. https://doi.org/10.1002/anie.201205718.
(228) Cattaneo, P.; Persico, M. An Abinitio Study of the Photochemistry of Azobenzene. *Phys. Chem. Chem. Phys.* **1999**, *1* (20), 4739–4743. https://doi.org/10.1039/A905055H.
(229) Nägele, T.; Hoche, R.; Zinth, W.; Wachtveitl, J. Femtosecond Photoisomerization of Cis-Azobenzene. *Chemical Physics Letters* **1997**, *272* (5), 489–495. https://doi.org/10.1016/S0009-2614(97)00531-9.
(230) Cembran, A.; Bernardi, F.; Garavelli, M.; Gagliardi, L.; Orlandi, G. On the Mechanism of the Cis−trans Isomerization in the Lowest Electronic States of Azobenzene: S0, S1, and T1. *J. Am. Chem. Soc.* **2004**, *126* (10), 3234–3243. https://doi.org/10.1021/ja038327y.
(231) Tiago, M. L.; Ismail-Beigi, S.; Louie, S. G. Photoisomerization of Azobenzene from First-Principles Constrained Density-Functional Calculations. *J. Chem. Phys.* **2005**, *122* (9), 094311. https://doi.org/10.1063/1.1861873.
(232) Bortolus, Pietro.; Monti, Sandra. Cis-Trans Photoisomerization of Azobenzene. Solvent and Triplet Donors Effects. *J. Phys. Chem.* **1979**, *83* (6), 648–652. https://doi.org/10.1021/j100469a002.
(233) Tan, E. M. M.; Amirjalayer, S.; Smolarek, S.; Vdovin, A.; Zerbetto, F.; Buma, W. J. Fast Photodynamics of Azobenzene Probed by Scanning Excited-State Potential Energy Surfaces Using Slow Spectroscopy. *Nat Commun* **2015**, *6* (1), 5860. https://doi.org/10.1038/ncomms6860.
(234) Crecca, C. R.; Roitberg, A. E. Theoretical Study of the Isomerization Mechanism of Azobenzene and Disubstituted Azobenzene Derivatives. *J. Phys. Chem. A* **2006**, *110* (26), 8188–8203. https://doi.org/10.1021/jp057413c.
(235) Zhang, C.; Du, M. H.; Cheng, H. P.; Zhang, X. G.; Roitberg, A. E.; Krause, J. L. Coherent Electron Transport through an Azobenzene Molecule: A Light-Driven Molecular Switch. *Physical Review Letters* **2004**, *92* (15), 158301. https://doi.org/10.1103/PhysRevLett.92.158301.

(236) Kim, Y.; Garcia-Lekue, A.; Sysoiev, D.; Frederiksen, T.; Groth, U.; Scheer, E. Charge Transport in Azobenzene-Based Single-Molecule Junctions. *Physical Review Letters* **2012**, *109* (22), 226801. https://doi.org/10.1103/PhysRevLett.109.226801.
(237) Thomas, L.; Arbouch, I.; Guérin, D.; Wallart, X.; van Dyck, C.; Mélin, T.; Cornil, J.; Vuillaume, D.; Lenfant, S. Conductance Switching of Azobenzene-Based Self-Assembled Monolayers on Cobalt Probed by UHV Conductive-AFM. *Nanoscale* **2021**, *13* (14), 6977–6990. https://doi.org/10.1039/D1NR00106J.
(238) Dürr, H.; Bouas-Laurent, H. *Photochromism: Molecules and Systems*; Studies in organic chemistry (Elsevier Science Publishers); Elsevier ; Distributors for the U.S. and Canada, Elsevier Science Pub. Co.: Amsterdam, New York, 1990.
(239) Zhou, X.-L.; Zhu, X.-Y.; White, J. M. Photochemistry at Adsorbate/Metal Interfaces. *Surface Science Reports* **1991**, *13* (3–6), 73–220. https://doi.org/10.1016/0167-5729(91)90009-M.
(240) Kirakosian, A.; Comstock, M. J.; Cho, J.; Crommie, M. F. Molecular Commensurability with a Surface Reconstruction: STM Study of Azobenzene on Au(111). *Phys. Rev. B* **2005**, *71* (11), 113409. https://doi.org/10.1103/PhysRevB.71.113409.
(241) Dri, C.; Peters, M. V.; Schwarz, J.; Hecht, S.; Grill, L. Spatial Periodicity in Molecular Switching. *Nature Nanotech* **2008**, *3* (11), 649–653. https://doi.org/10.1038/nnano.2008.269.
(242) Levy, N.; Comstock, M. J.; Cho, J.; Berbil-Bautista, L.; Kirakosian, A.; Lauterwasser, F.; Poulsen, D. A.; Fréchet, J. M. J.; Crommie, M. F. Self-Patterned Molecular Photoswitching in Nanoscale Surface Assemblies. *Nano Letters* **2009**, *9* (3), 935–939. https://doi.org/10.1021/nl802632g.
(243) Jaekel, S.; Richter, A.; Lindner, R.; Bechstein, R.; Nacci, C.; Hecht, S.; Kühnle, A.; Grill, L. Reversible and Efficient Light-Induced Molecular Switching on an Insulator Surface. *ACS Nano* **2018**, *12* (2), 1821–1828. https://doi.org/10.1021/acsnano.7b08624.
(244) Cho, D.; Yang, M.; Shin, N.; Hong, S. Mapping Reversible Photoswitching of Molecular Resistance Fluctuations during the Conformational Transformation of Azobenzene-Terminated Molecular Switches. *Nanotechnology* **2018**, *29* (36), 365704. https://doi.org/10.1088/1361-6528/aacb17.
(245) Füchsel, G.; Klamroth, T.; Dokić, J.; Saalfrank, P. On the Electronic Structure of Neutral and Ionic Azobenzenes and Their Possible Role as Surface Mounted Molecular Switches. *J. Phys. Chem. B* **2006**, *110* (33), 16337–16345. https://doi.org/10.1021/jp060969v.
(246) Alemani, M. Low Temperature STM Investigation of Molecular Manipulation, Decoupling and Switching. **2007**. https://doi.org/10.17169/refubium-9785.
(247) Comstock, M. J.; Levy, N.; Kirakosian, A.; Cho, J.; Lauterwasser, F.; Harvey, J. H.; Strubbe, D. A.; Fréchet, J. M. J.; Trauner, D.; Louie, S. G.; Crommie, M. F. Reversible Photomechanical Switching of Individual Engineered Molecules at a Metallic Surface. *Physical Review Letters* **2007**, *99* (3), 038301. https://doi.org/10.1103/PhysRevLett.99.038301.
(248) Stipe, B. C.; Rezaei, M. A.; Ho, W. Inducing and Viewing the Rotational Motion of a Single Molecule. *Science* **1998**, *279* (5358), 1907–1909. https://doi.org/10.1126/science.279.5358.1907.
(249) Haberfield, P.; Block, P. M.; Lux, M. S. Enthalpies of Solvent Transfer of the Transition States in the Cis-Trans Isomerization of Azo Compounds. Rotation vs. the Nitrogen Inversion Mechanism. *J. Am. Chem. Soc.* **1975**, *97* (20), 5804–5806. https://doi.org/10.1021/ja00853a025.
(250) Hagen, S.; Kate, P.; Leyssner, F.; Nandi, D.; Wolf, M.; Tegeder, P. Excitation Mechanism in the Photoisomerization of a Surface-Bound Azobenzene Derivative: Role of the Metallic Substrate. *The Journal of Chemical Physics* **2008**, *129* (16), 164102. https://doi.org/10.1063/1.2997343.
(251) Óvári, L.; Luo, Y.; Leyssner, F.; Haag, R.; Wolf, M.; Tegeder, P. Adsorption and Switching Properties of a N-Benzylideneaniline Based Molecular Switch on a Au(111) Surface. *The Journal of Chemical Physics* **2010**, *133* (4), 044707. https://doi.org/10.1063/1.3460647.
(252) Hallett-Tapley, G. L.; D'Alfonso, C.; Pacioni, N. L.; McTiernan, C. D.; González-Béjar, M.; Lanzalunga, O.; Alarcon, E. I.; Scaiano, J. C. Gold Nanoparticle Catalysis of the Cis–Trans Isomerization of Azobenzene. *Chem. Commun.* **2013**, *49* (86), 10073. https://doi.org/10.1039/c3cc41669k.

(253) Titov, E.; Lysyakova, L.; Lomadze, N.; Kabashin, A. V.; Saalfrank, P.; Santer, S. Thermal Cis-to-Trans Isomerization of Azobenzene-Containing Molecules Enhanced by Gold Nanoparticles: An Experimental and Theoretical Study. *J. Phys. Chem. C* **2015**, *119* (30), 17369–17377. https://doi.org/10.1021/acs.jpcc.5b02473.
(254) Goulet-Hanssens, A.; Utecht, M.; Mutruc, D.; Titov, E.; Schwarz, J.; Grubert, L.; Bléger, D.; Saalfrank, P.; Hecht, S. Electrocatalytic *Z* → *E* Isomerization of Azobenzenes. *J. Am. Chem. Soc.* **2017**, *139* (1), 335–341. https://doi.org/10.1021/jacs.6b10822.
(255) Bond Energies. In *Encyclopedia of Inorganic Chemistry*; John Wiley & Sons, Ltd, 2006. https://doi.org/10.1002/0470862106.id098.